Combining In Situ Measurements and Advanced Catalyst Layer Modeling in PEM Fuel Cells

Keith Thomas Regner

Thesis submitted to the faculty of Virginia Polytechnic Institute and State University in partial fulfillment of the requirements for the degree of

Master of Science
In
Mechanical Engineering

Michael Ellis – Chair
Partha P. Mukherjee
Michael von Spakovsky

August 26, 2011
Blacksburg, Virginia

Keywords: PEM Fuel Cell, Catalyst Layer, Through-Plane Transport, DNS, Measurement

Combining In Situ Measurements and Advanced Catalyst Layer Modeling in PEM Fuel Cells

Keith Thomas Regner

Abstract

Catalyst layer modeling can be a useful tool for fuel cell design. By comparing numerical results to experimental results, numerical models can provide a better understanding of the physical processes occurring within the fuel cell catalyst layer. This can lead to design optimization and cost reduction.

The purpose of this research was to compare, for the first time, a direct numerical simulation (DNS) model for the cathode catalyst layer of a PEM fuel cell to a newly developed experimental technique that measures the ionic potential through the length of the catalyst layer. A new design for a microstructured electrode scaffold (MES) is proposed and implemented. It was found that there is a 25%-27% difference between the model and the experimental measurements.

Case studies were also performed with the DNS to compare the effects of different operating conditions, specifically temperature and relative humidity, and different reconstructed microstructures. Suggested operating parameters are proposed for the best comparison between numerical and experimental results. Recommendations for microstructure reconstruction, MES construction and design, and potential measurement techniques are also given.

Dedicated to Willie and Charlie

Acknowledgements

I would like to thank the many people who have helped me in the completion of this research. Dr. Junbo Hou helped me extensively in the lab with experimental setup and sample preparation. With his help and time I gained extensive knowledge of laboratory procedures and equipment. Jay Tuggle, Steve McCartney, and Jim Schiffbauer at the nanoscale characterization and fabrication laboratory at Virginia Tech, both trained and assisted me with focused ion beam and scanning electron microscopy technology. Dr. Scott Renneckar and Jeff Dolan assisted and provided me with laser milling capabilities.

I would also like to thank my lab mates Jessica Wright, Chase Siuta, Ashley Gordon, Katherine Finlay, and Nathan May who never hesitated when asked for their time, and often unselfishly offered it. Not only were these people helpful in the lab, but they became great friends outside of the lab as well. I would like to thank my friends and family, especially my parents, for their moral support.

Most importantly I'd like to thank Dr. Partha Mukherjee and my advisor Dr. Mike Ellis. Dr. Mukherjee not only provided me with the direct numerical simulation program for the modeling portion of this research, but also spent numerous hours on the phone troubleshooting and interpreting data. Dr. Ellis introduced me to fuel cell research and gave me the opportunity to work on this project. He was very accommodating and always willing to help. Without his help and support throughout this period of personal transition, this research would not have been possible.

Table of Contents

List of Figures

List of Tables

1. Introduction

1.1 Fuel Cell Operation Overview. Figure 1 shows a schematic of a hydrogen-fueled proton exchange membrane fuel cell (PEMFC). Humidified hydrogen is supplied through the anode flow/gas channel and diffuses through the anode diffusion layer. When the hydrogen comes into contact with the catalyst later, it is reduced easily to hydrogen ions and electrons through the hydrogen oxidation reaction shown in Eq. (1).

$$2H_2 \rightarrow 4e^- + 4H^+ \quad (1)$$

The key to a PEM fuel cell's operation is that the membrane of the fuel cell is ionically conductive only. This means that the hydrogen ions can proceed directly to the cathode through the membrane but the electrons have to take an alternate path through an electrical load.

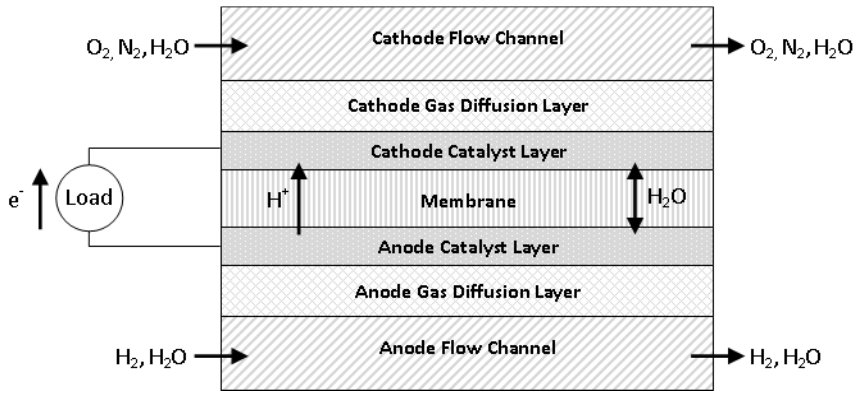

Figure 1. Schematic of a hydrogen PEM fuel cell.

The cathode gas channels and diffusion layer serve similar purposes as the anode side. Humidified air or oxygen is supplied through the cathode gas channel and diffuses towards the cathode catalyst layer through the diffusion layer. The electrons, hydrogen ions, and oxygen molecules meet in the cathode catalyst layer and combine to form water through the oxygen reduction reaction shown in Eq. (2); leading to an overall reaction for the fuel cell shown in Eq. (3).

$$O_2 + 4e^- + 4H^+ \rightarrow 2H_2O \quad (2)$$

$$2H_2 + O_2 \rightarrow 2H_2O \quad (3)$$

In both anode and cathode catalyst layers, a three phase boundary must exist in order for the reaction to occur. Pore space, electrically conductive material, and ionically conductive material must form a three phase boundary to allow transport of reactants, products, and electrons.

In the ideal (reversible) case, the fuel cell exhibits an open circuit voltage of 1.2 V. While producing current, losses reduce the cell voltage to a much lower value. These losses arise from processes that include electrochemical reactions at each electrode, mass transport through the flow channels and porous

electrodes (the diffusion layer and the catalyst layer), and transport of electrons and ions through the electrodes. These losses are affected by processes such as water production due to the electrochemical reaction and water diffusion through the membrane into the catalyst layer due to electro-osmotic drag. It is important to become familiar with these processes and the laws governing them in order to create an accurate description of fuel cell performance.

Fuel cell modeling allows us to predict and analyze the performance of a fuel cell before it is built. Models can demonstrate effects of different operating conditions and catalyst loadings, among other things. Some models can even predict effects of catalyst layer morphology, including graded catalyst and Nafion loading through the catalyst layer and variable catalyst layer porosity. These models can be used to design improved fuel cell components and fuel cell systems. The following section explains the processes occurring within the cathode of a fuel cell. These mathematical descriptions can be used to develop fuel cell models of different types.

1.2 Cathode Processes. Hydrogen PEM fuel cells use either humidified air or humidified oxygen as the oxidizing agent at the cathode. The oxidant is supplied through the cathode gas channels and its behavior within the gas channel can be described with the continuity and conservation of momentum equations shown in Eq. (4) and Eq. (5)

$$\frac{\partial(\rho)}{\partial t} + \boldsymbol{\nabla} \cdot (\rho \boldsymbol{U}) = 0 \tag{4}$$

$$\rho \frac{D(\boldsymbol{U})}{Dt} = -\boldsymbol{\nabla} p + \rho \boldsymbol{g} + \boldsymbol{\nabla} \cdot (\tau'_{ij}) \tag{5}$$

where ρ, $\boldsymbol{U}$, $\boldsymbol{g}$, and p are the mixture density, velocity vector, gravity vector, and the thermodynamic pressure, respectively. The τ'_{ij} are the viscous stresses on the fluid. The temperature distribution within the channel can be modeled with the thermal energy equation shown in Eq. (6)

$$\rho c_p \frac{DT}{Dt} = \beta T \frac{Dp}{Dt} + \boldsymbol{\nabla} \cdot (k \boldsymbol{\nabla} T) + \Gamma \tag{6}$$

where T, c_p, k, β, and Γ represent the temperature, specific heat of the mixture, thermal conductivity of the mixture, the coefficient of thermal expansion for the mixture, and the dissipation function involving the viscous stresses.

The equations governing the mass transport through the porous electrodes (the diffusion layer and the catalyst layer) are similar to Eq. (4)-(6) with the addition of a porosity term and a thermal energy source term, and are shown in Eq. (7)-(9)

$$\frac{\partial(\varepsilon\rho)}{\partial t} + \boldsymbol{\nabla} \cdot (\varepsilon \rho \boldsymbol{U}) = 0 \tag{7}$$

$$\rho \frac{D(\varepsilon \boldsymbol{U})}{Dt} = -\varepsilon \boldsymbol{\nabla} p + \varepsilon \rho \boldsymbol{g} + \boldsymbol{\nabla} \cdot (\varepsilon \tau'_{ij}) \tag{8}$$

$$\rho c_p \frac{DT}{Dt} = \beta T \frac{Dp}{Dt} + \boldsymbol{\nabla} \cdot (k \boldsymbol{\nabla} T) + \Gamma + \Psi \tag{9}$$

where ε and Ψ are the porosity and the thermal energy source term. Thermal energy sources include heat generation from irreversibilities (diffusive, Ohmic, and activation overpotentials) and from the reversible thermal energy of the electrochemical reaction.

The conservation of mass equation in the porous electrode must include each individual species because water is being produced and oxygen and hydrogen are being consumed. This is especially important for water. Water can be produced in either the liquid phase or vapor phase depending on the temperature and local relative humidity at the reaction site. Water can also be added or removed from the cathode through electro-osmotic drag. When hydrogen ions move across the proton exchange membrane and the membrane is sufficiently hydrated, the ions "drag" water molecules across with them towards the cathode. The rate of electro-osmotic drag depends on the current and the membrane hydration. In addition, water can diffuse across the membrane due to a difference in concentration between the anode and cathode sides of the membrane.

The electronic and ionic charge produced by the electrochemical reaction must also be conserved and can be modeled with Eq. (10.1) and Eq. (10.2)

$$\frac{\partial q_e}{\partial t} = -\boldsymbol{\nabla} \cdot \mathbf{i}_e = \nabla \kappa_e \nabla \phi_e + \Psi_e \tag{10.1}$$

$$\frac{\partial q_i}{\partial t} = -\boldsymbol{\nabla} \cdot \mathbf{i}_i = \nabla \kappa_i \nabla \phi_i + \Psi_i \tag{10.2}$$

where subscripts e and i denote electronic and ionic phases, q is the charge density, $\boldsymbol{i}$ is the current density vector, κ is the conductivity, ϕ is the potential, and Ψ is the charge production. Since charge must be conserved, $\Psi_e = \Psi_i$. The electronic and ionic potentials can be related to the current production per unit area of catalyst surface, j, using the Butler-Volmer equation shown in Eq. (11).

$$j = j_o\left(e^{\alpha_c n F \eta_{act}/RT} - e^{-(1-\alpha_c) n F \eta_{act}/RT}\right) \tag{11}$$

where j_o, η_{act}, α_c, and n are the exchange current density, activation overpotential, cathodic transfer coefficient, and the number of electrons transferred in the electrochemical reaction (2), respectively. In order to have a multi-dimensional catalyst layer model, current density values can be converted to current production per unit volume of catalyst layer.

The preceding equations provide a general mathematical description of the processes within the cathode and involve only a few restrictive assumptions: (1) the fluid forms a mathematical continuum; (2) the particles are essentially in thermodynamic equilibrium (the "local equilibrium" assumption); (3) the only effective body forces are due to gravity; (4) heat conduction follows Fourier's law [1]; (5) assumptions of the Butler-Volmer equation are satisfied. The most difficult terms to define in these equations are the viscous stress terms and the thermal energy source terms which can be functions of position, time, and temperature.

Although the preceding equations describe the processes occurring on the cathode side of a fuel cell quite thoroughly, this system of coupled, transient, partial differential equations with time and position

varying coefficients must be solved in order to obtain solutions for current density, ionic potential, water/oxygen concentrations, temperature, and other unknown variables. This becomes nearly impossible without making simplifying assumptions. Fortunately, assumptions such as isothermal and steady state operation, the specific phase of the product water, and others can be made to simplify the governing equations and allow for computational modeling.

1.3 Purpose of Research. This research can be divided into three areas: catalyst layer reconstruction, modeling catalyst layer processes, and experimental measurement of ionic potential. The purpose of this research is to study the underlying transport phenomena using a direct numerical simulation (DNS) of the cathode catalyst layer developed by Mukherjee and Wang [2], and validate and verify the findings to the experimental through-plane ionic potential measurements. The DNS model provides cross-sectional area averaged ionic potential results through the thickness of a stochastically reconstructed catalyst layer. The experimental data is gathered by a newly developed technique (Hess et al. [3]) and yields ionic potential measurement data at different locations through the catalyst layer. By comparing the numerical results to the experimental results, the computational model can be evaluated and validated. The experimental data can also provide further insight into the catalyst layer structure, processes occurring within the catalyst layer of a PEM fuel cell, and numerical catalyst layer reconstruction methods. Finally, the model can help to guide improvements to the existing ionic potential measurement technique.

2. Literature Survey

2.1 Porous Media Characterization. One method of modeling cathode catalyst layer processes in a PEM fuel cell involves discretizing the governing equations and solving them in a numerical domain with features equivalent to those of the actual catalyst layer. Before the governing equations can be solved, however, it is first necessary to characterize the microstructure of the porous catalyst layer, as this is an essential input into predictive modeling. The following sections summarize different methods for doing so.

2.1.1 Mercury Intrusion Porosimetry. Porosimetry is a technique used to measure pore size distribution, volume, density, and other porosity-related properties of a material. A non-wetting fluid like mercury is forced into the pores of the material by an external pressure. The equilibrium pressure is inversely proportional to the pore size; higher pressure is required to intrude mercury into micropores while less pressure is required to intrude mercury into macropores. The relationship between equilibrium pressure and the amount of mercury intruded into the material can be used to find pore size data.

Mercury intrusion porosimetry (MIP) is widely used to characterize porous materials. Kong et al. [4] used MIP to investigate the influence of pore-size distributions in the diffusion layer on mass transport in PEM fuel cells. It was found that pore-size distribution has a more important effect on cell performance than the total porosity of the gas diffusion layer. Androutsopoulos et al. [5] developed a model to interpret mercury penetration and retraction behavior when using MIP to determine pore structure and distribution in porous materials. The model can predict the movement of mercury under increasing or decreasing pressure which can give insight into the interconnectedness of pore segments.

While MIP is a useful technique for characterizing porous media, it does have disadvantages. Firstly, it is a destructive technique. Once MIP is conducted on a sample, the sample cannot be used again. This disadvantage is not significant if the porous homogeneity of the bulk material can be ensured so that tests can be made on a representative sample. More significantly, intrusion pressure may crush the structures being evaluated. MIP is not a useful tool when examining a porous material consisting of more than one material (carbon and ionomer), as it cannot distinguish between the two different materials. For this reason, MIP does not provide an adequate description of fuel cell catalyst layers for direct numerical simulation.

2.1.2 X-Ray Computed Tomography. Another method to characterize the catalyst layer is through 3-D experimental images using nondestructive X-ray computed tomography (CT). Penetrating radiation is used to take high resolution X-ray pictures. By rotating the sample, X-ray pictures can be taken at multiple angles; the pictures can then be computationally analyzed and assembled to obtain 3-D volume information. The grayscale pictures produced by the CT represent X-ray absorption coefficients of the materials within the medium and can be used to distinguish between different materials. CT has been used in the medical field for many years but more recently has other applications including the evaluation of crack distribution and propagation in porous

materials under loading [6], characterization of biological materials like wood [7], and evaluation of porous electrodes in fuel cells.

Griesser et al. [8] used CT to characterize the porous electrodes in solid oxide fuel cells (SOFC). They were able to determine the location and distribution of cracks, channels, and medium sized pores in the catalyst layer. This information helps determine the ionic conductivity of the ceramic and the mechanical stability of the catalyst layer leading to geometrical optimization and methods for improving materials and processes.

Izzo et al. [9] used CT to reconstruct SOFC anodes at sub-50 nm resolution. Using this method they were able to find the porosity and tortuosity of the porous electrode as well as the percentage of transport pores, or the percentage of pores forming a continuous pathway from one end of the sample to the other. Structural parameters found using CT showed good agreement with prior results using MIP. The reconstructed porous medium was then used to computationally predict pore-scale mass transport and electrochemical reactions within the SOFC anode to optimize electrode structure for achieving higher power density and durability.

Recently, Pfrang et al. [10] used X-ray computed tomography to image membrane electrode assemblies (MEA) of PEM fuel cells. 3-D images of the MEA and attached gas diffusion layers reached sub-μm resolution. The carbon fibers of the gas diffusion layer could be resolved and the catalyst layers could be visualized.

2.1.3 Stochastic Reconstruction Methods. Stochastic reconstruction methods use two dimensional images of a porous medium to statistically reconstruct the pore network. Quiblier [11] was first to extend this method in three dimensions using a probability distribution function and a two-point autocorrelation function found from the 2-D image. Bentz et al. [12] simplified the approach outlined by Quiblier by exploring the effectiveness of a modification to the reconstructed microstructures based on analysis of the hydraulic radius of the porous media. Liang et al. [13] improved the method introduced by Quiblier by introducing a truncated Gaussian method using the Fourier transform. This improvement reduces both computer time and memory required by eliminating the need to solve a system of nonlinear equations.

Okabe et al. [14] used multiple-point statistical information, which describes the statistical relation between multiple spatial locations, from thin 2-D sections to generate 3-D pore-space representations. The model was tested on Fontainebleau sandstone and it was found that the use of multiple-point statistics predicts long range connectivity of pore structures better than two-point statistical methods.

Yeong et al. [15] reconstructed random porous media from limited morphological information using a variation of the simulated annealing method. The procedure involves finding a state of minimum “energy” among a set of many local minima by interchanging the phase of pixels in the digitized system. The energy is defined in terms of the sum of a squared difference between a reference and simulated correlation function. The capabilities of the model were demonstrated by

reconstructing 1-D and 2-D porous structures, and later extended to three dimensions [16]. Kim et al. [17] used a method based on simulated annealing to reconstruct the catalyst layer in a PEM fuel cell. Three phases are reconstructed; platinum/carbon, electrolyte, and gas pores. The pore size distribution of the reconstructed catalyst layer is validated against experimental results.

Another method to reconstructing porous media is to take multiple images through the material. While CT is one method for doing this, another is with the help of a focused ion beam (FIB) and a scanning electron microscope (SEM). A picture of the sample can be taken with the SEM then the FIB can remove a layer of material and another picture can be taken. This process can be repeated until the desired number of pictures is acquired. The porous structure between each SEM picture can then be assembled stochastically. Bansal et al. [18] successfully reconstructed sub-20 nm features in silicone using this technique. Wilson et al. [19] used this technique to make a complete 3-D reconstruction of a SOFC anode. The data was used to calculate critical microstructural features such as volume fractions and surface areas of specific phases, three phase boundary length, and the connectivity and tortuosity of specific sub-phases. While this technique is useful for many different materials, FIB sectioning tends to be difficult for polymer based materials, such as a PEM catalyst layer, because the beam damages the polymer in the vicinity of the cut, leading to inaccurate images.

The problem of reconstructing random heterogeneous microstructures is applicable when trying to reconstruct fuel cell catalyst layers. The simulated annealing technique is one approach to doing so. More recently, however, Patelli et al. [20] suggest a hybrid approach utilizing both the simulated annealing technique and a genetic algorithm. The simulated annealing technique is used to refine the solutions identified by means of the genetic algorithm, increasing both accuracy and efficiency. Kasula et al. [21] successfully reconstructed solid oxide and PEM fuel cell electrodes using 2-D transmission electron microscope (TEM) images. Stochastic reconstructions yielded three phase representations. It was found that two-point statistics yielded a more realistic representation of the porous media than one-point statistics. SOFC reconstructions were implemented into a numerical model using the Lattice Boltzmann Method (LBM).

Wang et al. [22] reconstructed a regular microstructure to be implemented into a direct numerical simulation PEMFC catalyst layer model to study morphological effects of the catalyst layer on fuel cell performance. Wang et al. [23] followed with the reconstruction and implementation of a random microstructure. The reconstructed microstructures are simplified to contain two phases, the gas/void phase and a mixed electrolyte/electronic phase. Ultimately, Mukherjee and Wang [2] generated the microstructure of a PEM catalyst layer using the Gaussian random field method extended to three dimensions developed by Quiblier [11] with a simplifying modification developed by Bentz et al. [12]. This stochastic simulation technique is capable of generating 3-D replicas of the random microstructure based on specified low-order statistical information (as opposed to using multiple-point statistics for simplification) such as the porosity and a two-point autocorrelation function. This information can be obtained from processing micrographs of the porous sample into binary-image format. This numerical representation of the catalyst layer can then be implemented in the

aforementioned DNS model. Because of low cost and high microstructure reconstruction speed, this reconstruction method is used throughout this research and a more detailed description follows.

The stochastic reconstruction method assumes that an arbitrarily complex pore structure can be described using a phase function, $Z(\boldsymbol{r})$. The value of the phase function at each point, $\boldsymbol{r}$, equals a value of zero if the point belongs to the pore/void phase, and a value of one if the point belongs to the solid phase. Mathematically, the phase function can be described with Eq. (12) [24]

$$Z(\boldsymbol{r}) = \begin{cases} 0, & \text{if } \mathbf{r} \text{ is in pore space} \\ 1, & \text{otherwise} \end{cases} \tag{12}$$

If the pore structure is statistically *homogeneous*, then it can be described using two statistical properties; the porosity, ε, and the two-point autocorrelation function, $A_Z(\boldsymbol{u})$. The porosity is the probability that a point within the domain is in the pore/void phase ($Z(\boldsymbol{r}) = 0$). The two-point autocorrelation function is the probability that two points at a distance $\boldsymbol{r}$ are both in the pore/void phase. The porosity and two-point autocorrelation function are defined mathematically in Eq. (13) and Eq. (14) [24]

$$\varepsilon = \overline{Z(\boldsymbol{r})}, \qquad \measuredangle \boldsymbol{r} \tag{13}$$

$$A_Z(\boldsymbol{u}) = \frac{\overline{[Z(\boldsymbol{r})-\varepsilon][Z(\boldsymbol{r}+\boldsymbol{u})-\varepsilon]}}{\varepsilon-\varepsilon^2}, \qquad \measuredangle \boldsymbol{r} \tag{14}$$

where overbar denotes a statistical average and $\boldsymbol{u}$ is the lag vector. If the porous medium is statistically homogeneous, the porosity is uniform.

In general, the stochastic reconstruction method rebuilds the porous medium using an image of the actual medium (TEM or SEM). The two-point autocorrelation function can be calculated from the image by converting the image to binary. If the *M x N* pixel 2-D image is defined as a discrete valued function *I(x, y)* with periodic boundaries, where *I(x, y)* equals one for solid phase and zero for pore/void phase, the two-point autocorrelation function, *S(x, y)*, found from the binary image is given by Eq. (15) [25]

$$S(x,y) = \sum_{i=1}^{M}\sum_{j=1}^{N}\frac{I(i,j)\times I(i+x,j+y)}{M\times N} \tag{15}$$

The two-point autocorrelation function can be converted to its polar form, *S(r)*, for distances *r* in pixels with Eq. (16) [25] and imposed onto a three dimensional domain, *F(x,y,z)*, with Eq. (17) [26]

$$S(r) = \frac{1}{2r+1}\sum_{l=0}^{2r}\bar{S}\left(r,\frac{\pi l}{4r}\right) \tag{16}$$

$$F(r) = F(x,y,z) = \frac{[S\left(r=\sqrt{x^2+y^2+z^2}\right)-S(0)\times S(0)]}{[S(0)-S(0)\times S(0)]} \tag{17}$$

where $\bar{S}(r,\theta) = S(r\cos\theta\,, r\sin\theta)$ is obtained by bilinear interpolation from the values *S(x, y)*.

Following the approach by Quiblier [11], an initial 3-D image is generated that consists of Gaussian distributed noise generated using a uniform random number generator and the Box-Muller method to convert the uniform random deviates to normal deviates. This 3-D noise image, *N(x, y, z)*, is directly filtered with the 3-D autocorrelation function, *F(x, y, z)*. The resulting image can be described with Eq. (18)

$$R(x,y,z) = \sum_{i=0}^{m}\sum_{j=0}^{n}\sum_{k=0}^{p} N(i+x, j+y, k+z) \times F(i,j,k) \quad (18)$$

Values obtained from Eq. (18) are then rounded to 0 or 1 to create a binary image. This is a simplification to the method used by Quiblier [11] where a matrix of filtering coefficients must be found by solving a large system of nonlinear equations. This simplification was developed by Bentz et al. [12] and is desired numerically to avoid inversion.

The porosity of the resulting 3-D reconstruction can then be calculated. Earlier, a threshold was chosen for the gray scale for the 2-D binary image, above which points are set to solid phase and below which points are set to the pore/void phase. This gray scale threshold is iterated until the porosity of the reconstructed porous medium matches that of the actual sample (measured separately using standard techniques). A specialized structural designation routine is then used in order to establish structural connectivity [23]. The resulting 3-D microstructure contains two phases; void phase for oxygen and water transport and a mixed electrolyte phase containing ionomer, platinum, and carbon for electron and proton transport. The properties of the electrolyte phase are found from the volume fractions of ionomer, platinum, and carbon used in the catalyst layer fabrication process. Consequently, the specific interfacial area where the reaction occurs can be determined as a location where a transport void phase meets a transport electrolyte phase (see Section 3.1) [2].

2.2 Modeling Cathode Catalyst Layer Processes in PEM Fuel Cells. Modeling cathode catalyst layer processes can be very difficult because of the physics and governing equations that must be obeyed (see section 1.2). In order to properly model a catalyst layer it is very important to know the governing equations of the processes, the boundary conditions, and the initial conditions if the system is not at steady state. Different assumptions can be made to simplify the model. Selection of input parameters is also important for an accurate and efficient model. The following sections review ways of modeling the cathode catalyst layer.

2.2.1 Interface Models. Interface models treat the catalyst layer as a thin interface where the electrochemical reaction occurs. These models are based on the flux balance concept, which keeps track of all the species that flow in, out, and through the fuel cell. Mass, species, and charge must all be conserved in these models, which is captured by Eq. (19) [27]

$$\frac{j}{2F} = \frac{J_{H^+}^{M}}{2} = J_{H_2}^{A} = 2J_{O_2}^{C} = \frac{J_{H_2O}^{A}}{\alpha} = \frac{J_{H_2O}^{M}}{\alpha} = \frac{J_{H_2O}^{C}}{1+\alpha} \quad (19)$$

where *j, F, α,* $J_{H^+}^{M}, J_{H_2}^{A}, J_{O_2}^{C}, J_{H_2O}^{A}, J_{H_2O}^{M}$, and $J_{H_2O}^{C}$ represent the current density, Faraday's constant, the ratio between the water flux across the membrane and the charge flux across the membrane, net flux

of hydrogen ions across the membrane, net flux of hydrogen into the anode, net flux of oxygen into the cathode, net flux of water into the anode, net flux of water across the membrane, and net flux of water into the cathode, respectively.

Springer et al. [28] presented a 1-D, isothermal, steady state PEM fuel cell model that accounted for water diffusion coefficients, electro-osmotic drag coefficients, water sorption isotherms, and membrane conductivities. Polarization curves were generated at typical operating conditions. Bernardi et al. [29] developed a similar model to examine limitations of cell performance. With modern CFD, more complicated models can be developed. Among them, Khajeh-Hosseini-Dalasm et al. [30] developed a 3-D, transient, two phase, isothermal model for the cathode side of a PEM fuel cell and Hu et al. [31] developed a 3-D CFD model that accounts for two phase flow of water in both the cathode and the anode as well as the effects of flow channel rib resistance on species transport.

While interface and flux balance models can provide good predictions of overall fuel cell performance, they do not account for the intricacies of processes occurring within the catalyst layer during fuel cell operation, specifically, these models do not acknowledge the necessity for the existence of a three phase boundary for a functioning catalyst layer. To better understand the detailed interactions between geometry, fluid dynamics, multiphase flow, electrochemical reaction, and overall catalyst layer processes, the catalyst layer phases (carbon, ionomer, and void) must be modeled individually.

2.2.2 Agglomerate Models. Agglomerate models assume that the structure of the catalyst layer is composed of groups of platinum particles supported on carbon black particles and bounded by polymer electrolyte. Micropores exist inside the agglomerate between carbon grains while macropores constitute the void spaces between agglomerates. Because of the intricate porous structure, different modes of gas transport are responsible for the supply of oxygen to the reaction sites. Generally, oxygen reaches the reaction site through Knudsen diffusion or by Fickian diffusion in the micropores (pores within the agglomerates) and through Fickian diffusion in the macropores (pores around agglomerates). The relative importance of these distinct modes of diffusion is determined by the pore volumes of the micro and macropores, which is determined by the ionomer content in the catalyst layer, among other things.

Boundary conditions are implemented on the membrane/catalyst layer interface and the catalyst layer/gas diffusion layer interface. Based on different assumptions, current density, oxygen concentration, etc., can be found through the thickness of the catalyst layer. By varying agglomerate properties/geometry and the volume fractions of the components of the catalyst layer, the geometry and properties of the catalyst layer vary. Hence, the effects of catalyst layer geometry on cell performance can be investigated.

Broka et al. [32] compared an interface model and an agglomerate model (1-D and isothermal). It was found that the agglomerate model matched experimental results better. An SEM analysis was

also done on a catalyst layer. It was found that the agglomerate is a fairly geometrically accurate representation of an actual catalyst layer. Berg et al. [33] developed a non-isothermal, macroscopic model of the cathode catalyst layer in a PEM fuel cell. The model describes the reaction-diffusion kinetics of the three phase catalyst layer. It was found that an interface model may not hold over the whole range of realistic oxygen concentrations or when liquid pore water is present due to variations in the effective exchange current density with operating conditions. Genevey et al. [34] used a finite element method to model a transient cathode catalyst layer assuming an agglomerated structure. Equations for the conservation of reactants and products, electronic and ionic currents, and energy were considered.

Eikerling et al. [35] used the agglomerate model to investigate the performance of cathode catalyst layers in PEM fuel cells due to effects of oxygen diffusion, proton conductivity, and reaction kinetics. Ranges of optimum catalyst layer thicknesses are revealed depending on the current density range. Song et al. [36] used an agglomerate model to perform numerical optimizations with respect to one or two parameters of four design parameters of the cathode catalyst layer: Nafion content, porosity, thickness, and platinum loading. Similarly, Kamarajugadda et al. [37] explored the effects of ionomer loading, platinum loading, platinum/carbon ratio, agglomerate size, and catalyst layer thickness, while Wang et al. [38] examined different structures of agglomerates and their effect on performance. An approximate analytical solution for planar geometry of agglomerates was found as well as the effects of agglomerate radius and boundary conditions.

As CFD advanced, more complicated models emerged, including one developed by Schwarz et al. [39], who used CFD to calculate 3-D, multiphase, multicomponent transport phenomenon in a PEM fuel cell while taking account for the detailed composition and structure of the catalyst layers using a multiple thin-film agglomerate model. Furthermore, Liu et al. [40] presented a model that accounts for the full coupling of random porous morphology, transport properties, and electrochemical conversion in cathode catalyst layers with agglomerated structure. The model is capable of determining spatial distributions of water, oxygen, electrostatic potential, and reaction rate. A critical current density is observed under which the liquid water saturation is well below the critical value for pore blocking. At current densities larger than the critical current density, pore blocking occurs at different locations within the catalyst layer and reactant and reaction rate distributions are highly non-uniform. Schwarz et al. [41] examined the effect of 3-D spatially distributed catalyst loading on PEM fuel cell performance while Srinivasarao et al. [42] explored the use of multiple catalyst layers. The effects of ionomer content and porosity through the thickness of the catalyst layer were observed.

Siegel et al. [43] used electron microscopy to characterize the geometry of agglomerates within a catalyst layer. A CFD model was used to determine the effects of agglomerate geometry on fuel cell performance. It was found that control of catalyst layer structure at the microscopic level, particularly void fraction and characteristic agglomerate length, could lead to better fuel cell performance in the high current density region where concentration overpotential is most significant.

This work was later extended by Coppo et al. [44] to account for the temperature dependence of all model properties involved in the model formulation.

While agglomerate models represent the geometry of a catalyst layer, they may leave out many important features/non-uniformities of an actual catalyst layer. There are also some assumptions that are made, such as uniform ionic conductivity in the catalyst layer ionomer, that contribute to discrepancies with experimental results.

2.2.3 Direct Numerical Simulation. Direct numerical simulation (DNS) is a numerical technique to solve conservation equations in a mathematical domain. A two-stage numerical integration using the finite volume method approximates the temporal and spatial components of the governing equations. In catalyst layer modeling, DNS can be used to solve point-wise accurate species and charge transport equations directly on the digital representation of the catalyst layer. Doing so gives insight into the effects of morphological parameters on the performance of the cathode catalyst layer through a systematic pore-scale description of the underlying transport processes. The catalyst layer can be discretized by numerically reconstructing the porous microstructure (see Section 2.1).

Wang et al. [22] first introduced DNS in PEM fuel cells on regular catalyst layer microstructures and later to random catalyst layer microstructures [23]. Mukherjee and Wang [2] extended this work by using Fluent to implement direct numerical simulation on a stochastically reconstructed catalyst layer and later investigated the effects of bilayer cathode catalysts layers using DNS [45]. Although DNS requires numerical reconstruction of the catalyst layer and can be computationally expensive, it is a powerful method for modeling catalyst layer processes. Mukherjee and Wang's [2] choice of stochastic microstructure reconstruction coupled with their DNS model is used throughout this research and a more detailed description follows.

Mukherjee and Wang's [2] DNS code aims to model catalyst layer processes and examine species and charge gradients through-plane using a stochastically reconstructed catalyst layer. Due to the complex, coupled processes occurring within the catalyst layer of a PEM fuel cell (see Section 1.2), assumptions must still be made to simplify the governing equations and facilitate modeling. The key processes included in the model are: (1) the oxygen reduction reaction at an electrochemically active surface in the reconstructed pore structure as given by Eq. (2); (2) diffusion of oxygen and water vapor through the pore phase in the reconstructed pore structure; and (3) charge transport through the solid phase in the reconstructed pore structure.

The specific assumptions in the DNS model are as follows:

1. Isothermal and steady state operation.
2. The oxygen concentration in the void phase equals that in the thin polymer electrolyte film covering platinum reaction sites. The oxygen concentration gradient through the polymer electrolyte film to the reaction site is zero due to the small thickness of the film (~5 nm).
3. The solid phase in a real catalyst layer consists of electronically conducting material and ionically conducting material. Since the reconstructed microstructure only accounts for two

phases (void and solid), a Bruggeman correction is used to take into account the effect of the electronic phase volume fraction when calculating the ionic conductivity. Because the catalyst layer is very thin and its electronic conductivity is very high, the electronic phase potential is assumed to be uniform and electron transport is not considered.

4. Only water in the vapor phase is considered even if the water vapor concentration slightly exceeds the saturation value corresponding to the cell operation temperature (slight oversaturation is allowed).
5. Water in the electrolyte phase is in equilibrium with the water vapor; thus, only water transport through the void phase is considered.

Because of the assumptions made, the time terms and temperature terms in Eq. (7)-(10) can be neglected. Also, body forces due to gravity can be neglected since there is no liquid phase and gas phase body forces are small. The governing equations can therefore be reduced to three conservation equations for the transport of charge, oxygen, and water vapor shown in Eq. (20)-(22)

$$\nabla \cdot (\kappa_i \nabla \Phi_i) + S_\Phi = 0 \tag{20}$$

$$\nabla \cdot \left(D_{O_2}^g \nabla c_{O_2}\right) + S_{O_2} = 0 \tag{21}$$

$$\nabla \cdot \left(D_{H_2O}^g \nabla c_{H_2O}\right) + S_{H_2O} = 0 \tag{22}$$

where κ_i, $D_{O_2}^g$, $D_{H_2O}^g$, Φ_i, c_{O_2}, and c_{H_2O} are the ionic conductivity, diffusion coefficient of oxygen gas, diffusion coefficient of water vapor in gas, ionic phase potential, local concentration of oxygen, and local concentration of water vapor, respectively.

The ionic conductivity of the electrolyte phase is adjusted using a Bruggeman correction, shown in Eq. (23), to take into account the effect of the electronic phase volume fraction and the porosity of the catalyst layer.

$$\kappa_i = \kappa_o \left(\frac{\varepsilon_i}{\varepsilon_i + \varepsilon_e}\right)^n = \kappa_o \left(\frac{\varepsilon_i}{1 - \varepsilon_g}\right)^n \tag{23}$$

κ_o is the intrinsic conductivity of the ionomer, ε_i, ε_e, and ε_g are the ionic, electronic, and gas pore volume fractions, and n is a variable that accounts for the tortuosity of the ionomer within the catalyst layer, respectively.

The second terms in the conservation equations represent a volumetric source/sink term for charge, oxygen, and water vapor. The source term is only valid at the catalyzed interface where the electrochemical reaction takes place and is a function of the interfacial surface area per unit volume of catalyst layer, current density, and location. The specific interfacial area can be found through the microstructure reconstruction.

The overpotential, η, is defined in Eq. (24)

$$\eta = \Phi_e - \Phi_i - U_o \tag{24}$$

where Φ_e and U_o are the electronic phase potential and reference open circuit potential of the cathode at the cell operation temperature. Both of these values are constant. The conservation and source terms can be discretized to find parameters and overpotential at each active site within the 3-D reconstructed microstructure. Transfer current between two neighboring locations forming an active reaction interface is described by the Tafel equation. Details about the discretization can be found in Mukherjee and Wang [2].

Boundary conditions at each face of the 3-D reconstructed microstructure are needed for oxygen and water vapor concentration and ionic phase potential. For ease of implementation of the boundary conditions, one layer of electrolyte element is added at the boundary between the catalyst layer and the membrane, and a uniform operating current is applied to this layer. Similarly, at the boundary between the catalyst layer and the gas diffusion layer, one layer of pore elements is added and uniform oxygen and water vapor concentration is supplied to this layer. The boundary conditions at $y = 0$, $y = y_L$, $z = 0$, and $z = z_L$ (see Figure 5) are symmetrical and can be defined using Eq. (25)

$$\frac{\partial c_{O_2}}{\partial n} = 0, \qquad \frac{\partial c_{H_2O}}{\partial n} = 0, \qquad \frac{\partial \Phi_i}{\partial n} = 0 \tag{25}$$

where n is the direction normal to the respective boundary. These boundary conditions indicate that the concentrations of oxygen and water vapor and the ionic phase potential do not change at the boundary in the respective direction. Using a comparison to heat transfer, the boundary conditions in Eq. (25) represent insulated sides.

The boundary conditions in the x direction (see Figure 5) become more complicated. At $x = 0$ the boundary conditions are defined in Eq. (26)

$$\frac{\partial c_{O_2}}{\partial x} = 0, \qquad \frac{\partial c_{H_2O}}{\partial x} = -\frac{N_{w,net}}{D_{H_2O}}, \qquad -\kappa_i \frac{\partial \Phi_i}{\partial x} = I \tag{26}$$

where D_{H_2O} and I are the diffusion coefficient for water and the current density. $N_{w,net}$ represents the net water flux through the membrane. This term takes into account water diffusion through the membrane to the cathode side due to electro-osmotic drag as well as water flux through the membrane due to back diffusion from the cathode to the anode side and is defined in Eq. (27)

$$N_{w,net} = N_{w,drag} - N_{w,diff} = n_d \frac{I}{F} - N_{w,diff} = \alpha \frac{I}{F} \tag{27}$$

where $N_{w,drag}$ and $N_{w,diff}$ are water flux due to electro-osmotic drag and back diffusion, respectively. n_d is the electro-osmotic drag coefficient and refers to the number of water molecules migrated across the membrane per proton as current is passed. The net water transport can be simplified by defining a net water transport coefficient, α. α is assumed to be constant ($\alpha = 0.2$) although it depends on reaction rate and inlet humidity conditions. The boundary conditions at $x = x_L$ are defined in Eq. (28)

$$c_{O_2} = c_{O_2,x_L}, \qquad c_{H_2O} = c_{H_2O,x_L}, \qquad \frac{\partial \Phi_i}{\partial x} = 0 \tag{28}$$

where c_{O_2,x_L} and c_{H_2O,x_L} represent the oxygen and water vapor concentrations at the catalyst layer and gas diffusion layer interface. Both are adjusted to take into account the diffusion resistance through the gas diffusion layer with constant concentration in the flow channel, representing a high stoichiometric flow rate. Diffusion coefficients are adjusted with respect to gas diffusion layer porosity and tortuosity to take into account the diffusion resistance. Further details about the precise definitions of these concentrations can be found in Appendix A.

Input parameters into the model include operating conditions, geometry, and transport parameters. In the DNS model, most of these parameters are constant. However, ionic conductivity changes with location in the catalyst layer and species diffusivity is a function of operating parameters.

The ionic conductivity of the ionomer changes with location because it is a function of water content and the water content is a function of the relative humidity. Since water vapor production varies spatially within the catalyst layer, the concentration of water vapor, and consequently the relative humidity, varies throughout the catalyst layer. Therefore, the conductivity of the ionomer within the catalyst layer varies and must be calculated at every point where ionomer exists within the catalyst layer. For pore-level modeling, Knudsen diffusion due to molecule-to-wall collisions must be considered. The total diffusivity is therefore a combination of binary diffusivity and Knudsen diffusivity. The binary diffusion coefficients for oxygen and water vapor depend on the operating parameters of temperature and pressure while the Knudsen diffusion coefficients depend on temperature and mean pore size. Further details about calculating ionic conductivity, binary diffusivity, Knudsen diffusivity, and combined diffusivity can be found in Appendix B.

2.3 Techniques for Experimental Validation of Models. There are many characterization techniques that are used for validating fuel cell models and these techniques can generally be divided into two types: ex situ and in situ. Ex situ techniques characterize the detailed structure or properties of the individual components of the fuel cell. Generally, the components are completely separated from the fuel cell and are characterized in an unassembled, nonfunctional form. In situ techniques use the electrochemical variables of voltage, current, and time to characterize the performance of fuel cells under operating conditions [27]. The following sections review various ex situ and in situ characterization techniques for fuel cells.

2.3.1 Ex Situ Characterization Techniques. Most ex situ characterization techniques focus on identifying which individual elements most significantly impact fuel cell performance. Among the most important characteristics to evaluate are pore structure, catalyst surface area, electrode/electrolyte microstructure, and electrode/electrolyte chemistry.

Porosity of both the gas diffusion layer and the catalyst layer plays a large role in fuel cell performance. To be effective, the porosity must be large and exhibit interconnected pore space

through the entire material (effective porosity). Effective porosity can be determined using volume infiltration techniques like mercury intrusion porosimetry (see Section 2.1.1).

The effective porosity of a material is related to the permeability of the material. Permeability measures the ease with which gases move through the material. Gas diffusion layers and catalyst layers should have high permeabilities, while the membrane of the fuel cell should be impermeable to gases. Permeability can be measured by measuring the volume of a gas that passes through a material in a certain amount of time with a certain pressure drop.

Effective catalyst layers have high surface area in order to increase the possible area where the electrochemical reaction can occur. The most accurate technique for determining the surface area is known as the Brunauer-Emmett-Teller (BET) method. The BET method uses very low temperatures to create a thin layer of inert gas on the sample surface. Typically, a dry sample is evacuated of all gas and cooled to 77 K, the temperature of liquid nitrogen. A layer of inert gas will physically adhere to the sample surface, lowering the pressure in the analysis chamber. The surface area of the sample can then be calculated from the measured absorption isotherm [27].

A porous medium like the catalyst layer can also be characterized through examination of the microstructure, pore size distribution, and chemical determination. Section 2.1 summarizes many of the popular techniques. Others include X-ray diffraction (XRD) which provide crystal structure, orientation, and chemical compound information, Auger electron spectroscopy (AES), X-ray photoelectron spectroscopy (XPS), and secondary-ion mass spectroscopy (SIMS) [27].

2.3.2 In Situ Characterization Techniques. While ex situ techniques can provide information about individual components of the fuel cell, in situ electrochemical characterization techniques are more popular, and are used to study fuel cell performance and the effects of certain variables on the current and voltage of the fuel cell. The most popular in situ techniques include current-voltage measurement, current interrupt measurement, electrochemical impedance spectroscopy (EIS), and cyclic voltammetry (CV).

Current-voltage measurements (polarization curves) are the most popular technique to characterizing fuel cells, as they give insight into the overall performance of the fuel cell. Current-voltage measurements are usually obtained by allowing the fuel cell to draw a fixed current and measuring the corresponding operating voltage. By slowly stepping down the current demand, the entire current-voltage response for the fuel cell can be determined. With this information, polarization and power density curves can be obtained. It is important that the fuel cell is allowed to reach steady state and operating conditions are recorded (cell temperature, gas flow rates, etc.) before the current-voltage measurements are taken. By comparing experimental current-voltage measurements to model generated current-voltage points, overall performance can be compared, however, it is difficult to determine what exactly is causing any differences [27].

Current interrupt separates the contributions to fuel cell performance into Ohmic and non-Ohmic processes. Typically, a fuel cell is held at a fixed current until a current is abruptly imposed (or

withdrawn) at $t = 0$. The resulting voltage response is then recorded as a function of time. The interruption of the current causes an immediate voltage change followed by a transient change in voltage. The immediate voltage change is associated with the Ohmic resistance of the cell while the transient change in voltage is associated with the much slower reaction and mass transport processes. Usually, the Ohmic losses are determined at each measurement point on the current-voltage curve. An iR-corrected curve can then be obtained by removing the Ohmic losses from the current-voltage curve and can be used to separate the activation and concentration losses from the cell. Current interrupt is beneficial because it is a fast measurement method that usually doesn't require complicated hardware. By quantifying the Ohmic, activation, and concentration losses associated with the fuel cell, areas for improvements in the model can be exposed [27].

Electrochemical impedance spectroscopy (EIS) is a more sophisticated technique for distinguishing between Ohmic, activation, and concentration losses. This dynamic technique applies a sinusoidal voltage perturbation to the fuel cell and measures the corresponding amplitude and phase shift of the resulting current response. Measurements are conducted over a wide range of frequencies, resulting in the construction of an impedance spectrum, known as a Nyquist plot. Using the Nyquist plot, an equivalent circuit model can be constructed. Although EIS is time consuming, it can help distinguish, more specifically than current interrupt, between the effects of activation, Ohmic, and concentration losses [27].

Cyclic voltammetry (CV) is a technique that can provide insight into the reaction kinetics within a fuel cell. A voltage is swept linearly with time and the resulting cyclic current response is measured as a function of time but plotted as a function of the cyclic voltage sweep. CV can be used to determine the electrochemically active surface area in the cathode catalyst layer by quantifying the total charge provided by hydrogen adsorption or desorption on the catalyst surface. Most models require active surface area as an input parameter; CV can be used to determine this parameter [27].

The preceding techniques for fuel cell characterization are very popular and useful; at least one of these techniques is used in all the references. They don't, however, give any insight into gradients across the cathode catalyst layer which can be used to help validate the model developed by Mukherjee and Wang [2] used throughout this research. Recently, however, Hess et al. [3] developed the first method for taking in situ measurements of ionic potential within a PEM fuel cell cathode catalyst layer. Using this new technique, ionic potential can be measured at various points through the catalyst layer. This method is ideal for validating Mukherjee and Wang's [2] DNS model, as their model predicts the ionic potential through the cathode catalyst layer. This experimental potential measurement technique developed by Hess et al. [3] is used throughout this research to compare to potential gradient profiles obtained from the DNS model developed by Mukherjee and Wang [2]; a more detailed description of the experimental technique follows.

To obtain in situ measurements, a microstructured electrode scaffold (MES), originally proposed by Hess et al. [3] and shown in Figure 2, is fabricated. The MES consists of alternating layers of ion conducting material and insulating material which surround a hole filled with catalyst ink. The ion

conducting material intersects with the catalyst ink allowing for measurements of potential at discrete intervals through the thickness of the catalyst layer.

A tab protrudes from each layer of the MES and contacts a reference electrode used to measure ionic potential at that location within the catalyst layer. The hole filled with catalyst ink is micro-milled with a diameter between 100-200 μm so that transport effects within the catalyst layer can remain one-dimensional and edge effects can be neglected.

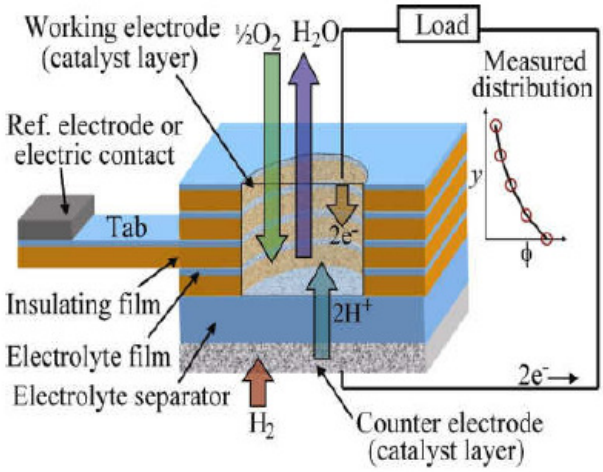

Figure 2. A microstructured electrode scaffold (MES) design used to measure potential at discrete intervals along the thickness of the cathode catalyst layer [3].

The MES takes the place of the cathode catalyst layer. Specially designed cathode hardware is used to accommodate the MES. With the MES in place, ionic potential can be measured at different depths in the cathode catalyst layer at different operating conditions.

2.4 Contributions of this Work to Catalyst Layer Modeling. Being able to model a process with a computer is very convenient. Before the physical product is constructed, it can be refined and optimized through the computer model. This reduces cost and time significantly. If an accurate model of a PEM fuel cell catalyst layer can be developed, parameters such as operating conditions, Platinum/Nafion loading, macro-geometry, and possibly even pore-structure geometry can be chosen to maximize overall fuel cell performance. The purpose of this research is to compare ionic potential distributions through the catalyst layer from the direct numerical simulation model developed by Mukherjee and Wang [2] to the in situ measurement technique developed by Hess et al. [3] with the purpose of validating the model.

Along with model evaluation, methods for improving the stochastic microstructure reconstruction method will be investigated as well methods for improving in situ measurement techniques of ionic potential in the catalyst layer. Since the in situ measurement technique is fairly new, there can be room for improvement, for example, in MES architecture and thickness.

3. Experimental Procedures

3.1 Porous Microstructure Reconstruction. Before the direct numerical simulation modeling can be performed, a numerical representation of the cathode catalyst layer must be constructed. This is done stochastically using 2-D binary micrographs. If a pore structure is statistically homogeneous, it can be described by the porosity of the medium and a two-point autocorrelation function. The porosity of the medium is the probability that a point within the porous medium is a void and is a constant for a statistically homogeneous porous medium. The two-point autocorrelation function is the probability that two different points within the medium are both in a void and is determined from a binary 2-D SEM image of the porous medium. The stochastic reconstruction method extended to 3-D developed by Quiblier [11] and modified by Bentz et al. [12] applied throughout this research, uses a 3-D white noise image filtered with the autocorrelation function to decide whether a point within a porous medium is a solid or a void. An iterative process is used to match the porosity of the reconstructed 3-D microstructure to the actual porosity of the sample which is determined through alternate means. Specific details about the process can be found in the preceding sections. The following steps summarize the process.

1. A grayscale SEM picture is taken of the porous sample of finite length and width as seen in Figure 3.

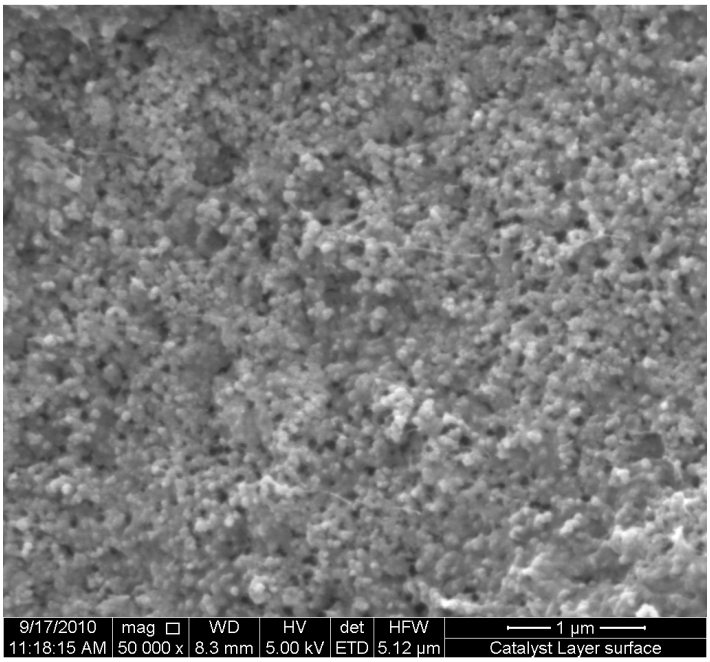

Figure 3. Grayscale image of a typical PEM catalyst layer.

2. The SEM picture is reduced to a binary black and white image by choosing a threshold grayscale value such that all pixels darker than that shade are in the solid phase and all pixels lighter than that shade are in the void phase. This binary image is obtained using standard image processing techniques and an example is shown in Figure 4.

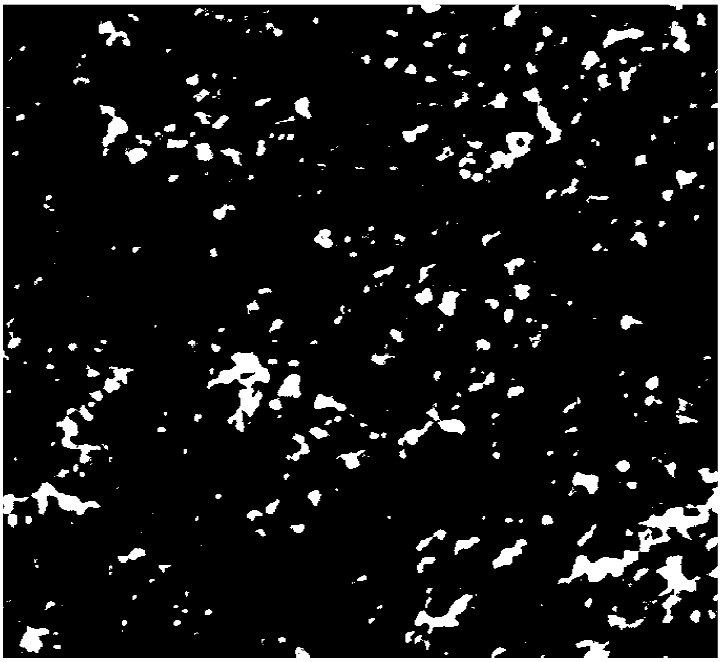

Figure 4. Grayscale threshold is chosen to convert the grayscale image to a binary image.

3. The two-point autocorrelation function is found from the binary SEM image using Eq. (15) and Eq. (16). The two-point autocorrelation function contains information about the probability of a point, $\boldsymbol{r} + \boldsymbol{u}$ belonging to the pore space when point $\boldsymbol{r}$ belongs to the pore space. $\boldsymbol{u}$ is a vector and $\boldsymbol{r}$ is the position vector of a variable point [11]. The autocorrelation function is then imposed on a 3-D domain using Eq. (17).
4. An initial 3-D image is constructed using a random number generator. These numbers are completely uncorrelated to one another; however, they must represent a Gaussian population [11].
5. The Box-Muller transformation is used to convert the uniform random deviates to normal deviates. This becomes a 3-D white noise image. This is a simplification by Bentz et al. [12] of the approach utilized by Quiblier [11], where a matrix of filtering coefficients is computed by solving a huge system of nonlinear equations.
6. This white noise image is then directly filtered with the two-point autocorrelation function, using Eq. (18). The resulting values are rounded to 0 or 1 and the 3-D microstructure representation is generated.

Figure 5 shows an example of a 3-D reconstructed microstructure of the cathode catalyst layer. As seen from the figure, there are two phases in the microstructure; electrolyte phase and pore phase. The electrolyte phase consists of a mix of the electronically and ionically conductive materials and the platinum catalyst sites. The pore phase allows for the flow of oxygen and water vapor to and from the catalyst sites. For each phase, there are two states; “transport” and “dead”. An element belonging to the “transport” state means that it is connected to the continuous network of its respective phase. An

element belonging to the "dead" state means that it is in an electrochemically inactive region because either ions/electrons or oxygen cannot physically get to the reaction site.

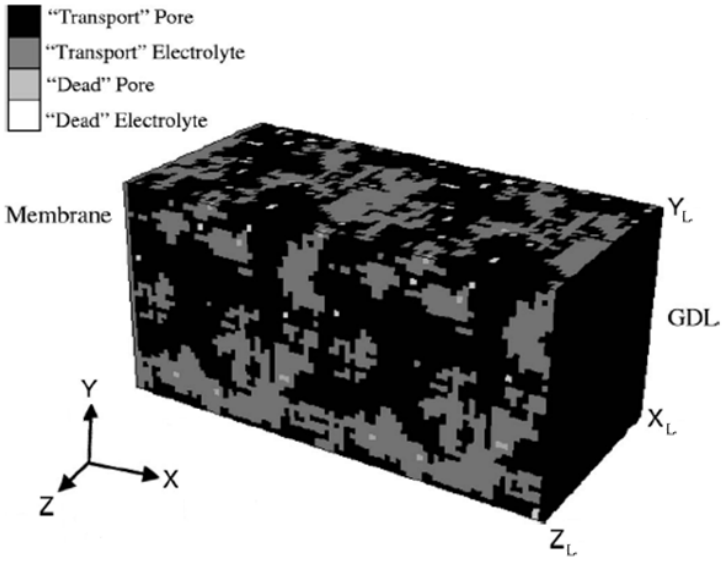

Figure 5. An example of a 3-D reconstructed microstructure using stochastic reconstruction to be implemented in a DNS computer model [2].

The resulting 3-D microstructure representation was found by choosing a certain grayscale threshold to determine the 2-D binary image. Since the choice of this threshold affects the overall porosity of the final reconstruction, the threshold has to be adjusted and chosen so that the porosity of the final reconstruction matches the actual porosity of the sample (an iterative process).

The porosity of the catalyst layer, ε_{CL}, can also be calculated with the properties of the materials used to prepare the catalyst ink using Eq. (29)

$$\varepsilon_{CL} = 1 - \left[\frac{1}{\rho_{Pt}} + \frac{1}{\rho_C R_{Pt/C}} + \frac{R_{I/C}}{\rho_{Nafion} R_{Pt/C}}\right]\frac{L_{Pt}}{X_{CL}} \qquad (29)$$

where ρ_{Pt}, ρ_C, ρ_{Nafion}, $R_{I/C}$, $R_{Pt/C}$, L_{Pt}, and X_{CL} are the are the densities of platinum (21.5 g/cm^3), carbon (1.8 g/cm^3), Nafion (~2 g/cm^3), weight ratio of Nafion to carbon, weight ratio of platinum to carbon, catalyst layer platinum loading, and catalyst layer thickness. All catalyst inks were prepared with 39.1% platinum supported on carbon, an ionomer to carbon ratio of 0.8, and a loading of 0.4 mg-Pt/cm^2. The thickness of the catalyst layer is dictated by the thickness of the MES, which varied between 20-25 µm depending on the MES (see Section 3.3.4). Using Eq. (29), the calculated porosity of the MES catalyst layer will be slightly high compared to the porosity of a typical catalyst layer due to the thickness of MES. Typical catalyst layers yield a porosity of around 60% and the grayscale threshold chosen to produce the binary SEM image is iterated so that the final porosity of the reconstructed catalyst layer is 60%. Consequently, DNS simulations are performed on reconstructed catalyst layers with porosities closer to that of a typical catalyst layer, but with a greater thickness.

Two different catalyst layer reconstructions were used throughout the modeling portion of this research, both with 60% porosity. The difference between the microstructures is in the generation of the initial, 3-D random matrix; each generated with different stochastic realizations. Both catalyst layers were reconstructed with 100 cells in the x direction and 50 cells in the y and z directions (see Figure 5) with a total thickness of 20 μm in the x direction and 10 μm in the y and z directions ($dx = dy = dz = 0.2$ μm). In addition, one layer of electrolyte-only cells is added to the membrane/catalyst layer interface and one layer of pore-only cells is added at the catalyst layer/gas diffusion layer interface for the implementation of boundary conditions.

The resulting 3-D microstructures are a discretized representation of a porous medium including a solid phase and a pore phase. A location at which a "transport" solid phase contacts a "transport" pore space represents an electrochemically active area. Direct numerical simulation can be used to solve the equations governing the processes within the cathode catalyst layer and variables such as current density, overpotential, oxygen concentration, and water concentrations can be found at each location within the reconstructed microstructure. These values can also be area averaged to find though-plane profiles.

3.2 Modeling Catalyst Layer Processes. The flexibility of the DNS model allows for the user to define cell operating temperature, exchange current density, oxygen and water boundary concentrations, the cathodic transfer coefficient for the oxygen reduction reaction, the net water transport coefficient (through the membrane), diffusion coefficients, and catalyst layer thickness. The DNS model solves the conservation equations within the domain of the reconstructed catalyst layer which is the output of the stochastic microstructure reconstruction program.

Desired model input parameters and boundary conditions can be modified as desired; more details about the input parameters can be found in Appendix C. The 3-D binary reconstructed microstructure information is obtained through an interpolation file. This interpolation file is basically the output of the 3-D microstructure generation code and imposes the binary microstructure information onto the generated mesh. This establishes the pore/solid distribution within the computational domain. Pore and electrolyte connectivity is established and thus makes the computational domain of the porous catalyst layer ready for subsequent flow calculations.

Once the model parameters, boundary conditions, and computational domain have been established the DNS is ready to be run. Approximately 5000 iterations must be performed in order to reach a level of sufficient convergence (approximately 8 hours on a single PC). The program returns useful information including data files of cross-sectional area averaged cathode overpotential, reaction current density, and water and oxygen concentrations vs. distance through the catalyst layer. These files can be used to obtain plots and examine trends. In order to obtain polarization curves, the DNS model must be run at each desired current density. The cell voltage, V_{cell}, can then be obtained with Eq. (30)

$$V_{cell} = U_o - \eta_c - HFR \times I \tag{30}$$

where U_o is the reversible voltage (1.2 V), η_c is the average value of potential in the catalyst layer, *HFR* is the high frequency resistance for the catalyst layer, and *I* is the current density. η_c is found from the area averaged cathode overpotential across the cathode catalyst layer; η_c is the average value of potential in the catalyst layer. After finding the cell voltage, polarizations curves can be plotted.

3.3 Through-Plane Ionic Potential Measurements. In order to evaluate the model developed by Mukherjee and Wang [2] discussed above and to gather further insight into catalyst layer processes, a technique for measuring ionic potential through the thickness of the catalyst layer is used. This technique developed by Hess et al. [3] uses a microstructured electrode scaffold (MES) (see Figure 2) and yields ionic potential measurements at different locations through the thickness of the catalyst layer.

The MES constructed and presented by Hess et al. [3] was approximately 50 μm thick. A typical catalyst layer thickness is between 15-20 μm and therefore, our main goal was to reduce the thickness of our MES to between 15-20 μm yet still retain the ability to easily take potential measurements. Hess et al. [3] created their sublayers (ionomer/insulating combination) by spin coating Nafion solution onto a Kapton sheet. The individual sublayers were then hot pressed together to create alternating insulating/ionically conductive layers as seen in Figure 2. While the spin coating process allowed for very thin layers of Nafion (~1 μm), the Kapton sheets were relatively thick (7.5 μm). This produced a Kapton/Nafion sublayer of ~9 μm and a total thickness of ~50 μm with five sublayers hot pressed together. By aiming to reduce the thickness of the insulating layer, the entire thickness of the MES could be reduced drastically.

A product search revealed that insulating materials are not sold in sheets that are thinner than 7.5 μm in thickness. This led to experimentation with solution casting of the insulating material, similar to the Nafion. The following sections summarize the design process, construction procedures of the final MES design, implementation of the MES into the fuel cell, and data collection methods.

3.3.1 Geometrical Considerations. The overall geometry of the MES is important to consider, ensuring the ability to easily take ionic potential measurements. As seen from Figure 2, a portion of each sublayer protrudes from the MES, separate from the other sublayers (there is no sublayer attached above or below during this portion). The ionic potential measurement can then be taken at the end of each protrusion on the ionomer layer, each corresponding to a certain distance through the catalyst layer. If each sublayer is to be hot pressed together to create the MES, the overall geometry of the MES is dependent on the geometry of each individual sublayer. When designing our MES, it was desired to keep a similar geometry for ease of measurement while reducing overall thickness.

As stated before, in order to reduce the overall thickness of the MES, solution casting the insulating layer was investigated, as opposed to using a pre-manufactured insulating sheet whose minimum thickness is only 7.5 μm. One method of solution casting is spin coating. In this process, excess solution is deposited on a high speed, rotating substrate in order to spread the fluid by centrifugal force; this method was chosen by Hess et al. [3] in order to create a thin Nafion layer, using a sheet of Kapton as the substrate.

Due to thickness, an insulating sheet was ruled out in our design. Alternately, insulating solution was spun coat on a glass substrate, and an ionically conducting solution was then spun coat on top of the resulting, thin insulating film. Because of its insulating properties and ability to solution cast, polyvinylidene fluoride (PVDF) was chosen as the insulating material, specifically Kynar 720. A 10 wt% PVDF solution was prepared in *N,N*-Dimethylacetamide (DMAc) and stirred for 8 hours at 80 °C. The ionically conducting solution chosen was 5 wt% Nafion solution from Ion Power.

While this method produced both thin PVDF and Nafion films, the spin coating process left poor sublayer geometry for taking potential measurements. Figure 6 shows a sublayer on a glass substrate created using the spin coating method.

Figure 6. A thin Nafion film cast on a thin PVDF film cast on a glass substrate using spin coating.

As seen from Figure 6, when using the spin coating process the shape of the thin film is difficult to control and tends to leave free form shapes. If multiple sublayers were hot pressed together, ionic potential measurement points would be difficult to establish due to the overall geometry of the MES. Additionally, the PVDF/Nafion sublayer is difficult to remove from the glass substrate without damaging the sublayer itself. Due to these reasons, the spin coating method was avoided.

An alternate solution casting method uses the effect of gravity to force a droplet of solution down a substrate. As the droplet slides down the substrate it leaves a trail; as the solvent evaporates, a thin film is left. Two to three drops of PVDF solution were deposited at the top of a vertical glass slide. After the solution slides down the slide and the solvent evaporates, a thin film of PVDF is left on the glass slide. The process is then repeated with the Nafion solution. Two to three drops of Nafion solution are deposited at the top of the vertical glass slide on top of the PVDF film. The solution is then guided down the slide, ensuring that it stays on top of the PVDF film. The result is a PVDF/Nafion sublayer approximately 1 cm x 7.5 cm x 3-6 µm.

The geometry of this sublayer is much more useful when taking potential measurements. Several sublayers can be oriented similarly to Figure 7 such that ionic potential can be measured at one end of the sublayer, and overlap at the other end (the location of the catalyst layer). Due to optimal

geometry and reduction in thickness of individual sublayers, this solution casting method was chosen as the best method to construct sublayers.

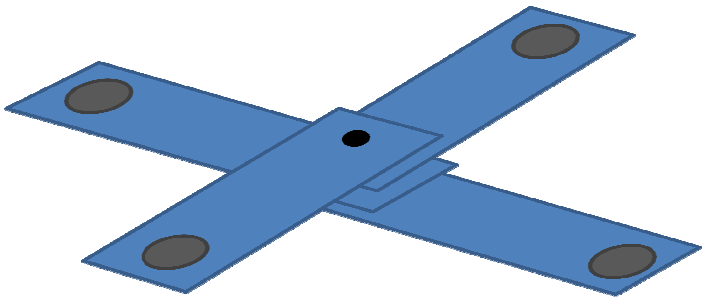

Figure 7. Orientation of sublayers to create MES. The blue rectangles represent PVDF/Nafion sublayers, the black hole represents the catalyst ink, and the gray ovals are where ionic potential measurements are taken.

3.3.2 Solvent Considerations. There are two possible ways to making sublayers using the aforementioned casting method: casting a Nafion film on a PVDF film or vice versa. The properties of the solvents of each solution play an important role in determining the best process for doing so. Because the solvent in the Nafion solution (isopropyl alcohol) does not dissolve Kynar 720, the integrity of the Kynar film is not compromised if a Nafion film is cast on top. If, however, the procedure were reversed (cast the Nafion film first then cast the PVDF film), the DMAc in the PVDF would dissolve the Nafion film when it is cast. Therefore, the PVDF film must first be cast on the glass slide; the Nafion can then be cast onto the thin PVDF film. A cross-sectional schematic of the sublayers is shown in Figure 8.

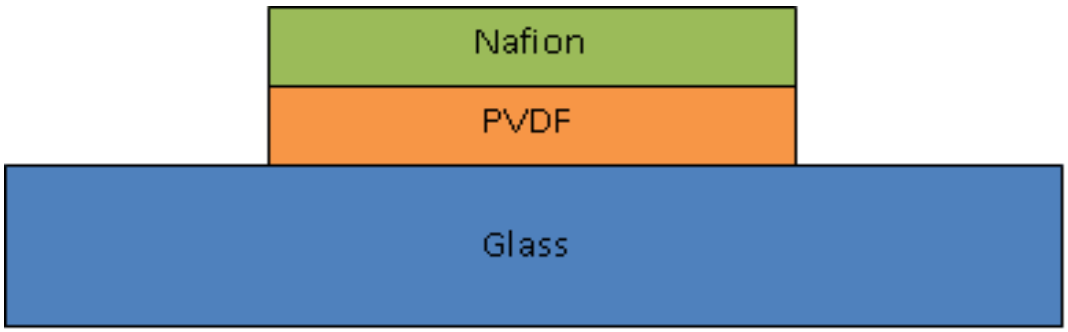

Figure 8. The Nafion film must be cast on top of the PVDF film to avoid problems with solvents.

For this same reason, sublayers cannot be continuously cast on top of one another. In other words, another PVDF film cannot be cast on an existing sublayer, as it will dissolve the adjacent Nafion film. Consequently, five individual sublayers are created on different glass slides with the Nafion film exposed (on top of the PVDF film). This orientation of the sublayers is an important

consideration in the overall construction and geometry of the MES. Removal of the sublayers from the glass substrate can be difficult as well and is described in the upcoming section.

3.3.3 MES Construction. The overall MES needs to be geometrically similar to Figure 7 where the blue rectangles represent the PVDF/Nafion sublayers. Each sublayer must overlap in the middle so a hole can be drilled and filled with catalyst ink to make up the cathode catalyst layer. The dark gray circles represent the measurement locations. At this point, the ionic potential through each Nafion film is measured to some reference, representing the ionic potential at different locations through the catalyst layer. Solution cast sublayers can achieve this geometry using an adhesive coated substrate.

Solution casting of PVDF is done on glass slides heated to between 85 and 90 °C to ensure uniform films without bubbles/holes. The glass is first cleaned using isopropyl alcohol to remove contaminants and dust. In a fume hood, a hotplate is turned on its side so that the heated surface is nearly vertical and the glass slide is then secured to the heated surface of the hot plate as seen in Figure 9.

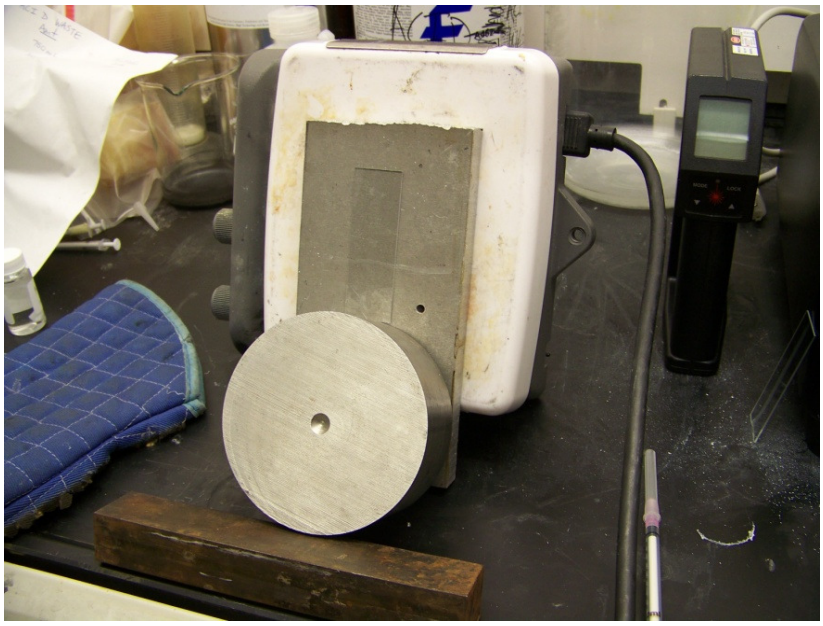

Figure 9. The experimental setup for casting thin PVDF films. The glass slide is heated to 85-90 °C.

The temperature of the glass is measured to ensure that it is within the desired temperature range. Using a syringe, 1-2 drops of preheated (55-65 °C) PVDF solution (10 wt% Kynar 720 in DMAc) are dispensed near the top of the glass slide. As gravity forces the drop to slide down the glass, it leaves a trail of solution in its path. As the DMAc evaporates, a long, thin PVDF film ~2-4 μm thick is left on the glass slide. The slide is kept at the elevated temperature for five minutes, then removed and cooled naturally.

After the PVDF films have fully cooled, a nitrogen source is used to remove any dust. The ionically conducting film is then cast directly onto the PVDF film using a similar method. One to two drops of 5 wt% Nafion solution (Ion Power) is dispensed near the top of the PVDF film at room temperature. Using gravity the drop can be guided along the PVDF film, leaving a Nafion film ~1-2 µm thick on top of the PVDF film after the solvent evaporates. The result, as mentioned earlier, is a PVDF/Nafion sublayer approximately 1 cm x 7.5 cm x 3-6 µm on a glass slide. The slides are set aside to dry before further construction.

In order to create the geometry in Figure 7, the sublayers must be transferred from the glass slide on which they were cast, to some other substrate that can create this geometry and be implemented into a fuel cell for data collection. This is done with Scotch tape and adhesive coated polytetrafluoroethylene (Teflon or PTFE) sheet.

First, a piece of adhesive coated PTFE (McMaster-Carr, 2208T11) is taped to the table with the adhesive coating side down. An outline of a 3” x 3” fuel cell is drawn on to the PTFE sheet and six 1/8” holes are punched as seen in Figure 10. Note that the backing is not peeled from the PTFE yet.

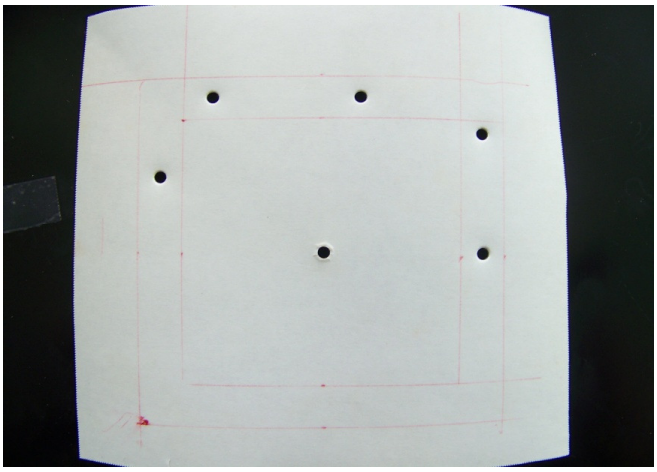

Figure 10. The outline of a 3" x 3" fuel cell is drawn onto the adhesive coated PTFE and six holes are punched.

Five holes are punched outside of the outline of the 3” x 3” fuel cell and one hole is punched in the center. The five outer holes will be where the ionic potential will be measured and the center hole is where all of the PVDF/Nafion sublayers will overlap.

Sublayers can be removed from the glass substrate using an adhesive coated material. The rigidity of the PTFE provides sufficient support for the sublayers but the adhesive is too aggressive to remove the sublayers from the glass without damaging them. Through experimentation, it was found that Scotch tape (3M) can effectively remove the sublayers from the glass without damage. For this reason, the two materials are used together. First, the backing is removed from the PTFE and the PTFE is applied to the outside of a roll of Scotch tape. The Scotch tape is then peeled off its roll and placed on the table with the adhesive side facing up. Six holes are then punched into the Scotch

tape at the appropriate locations. Figure 11 depicts this procedure. This configuration provides support from the PTFE, but allows for easy removal of sublayers from the glass with the Scotch tape adhesive.

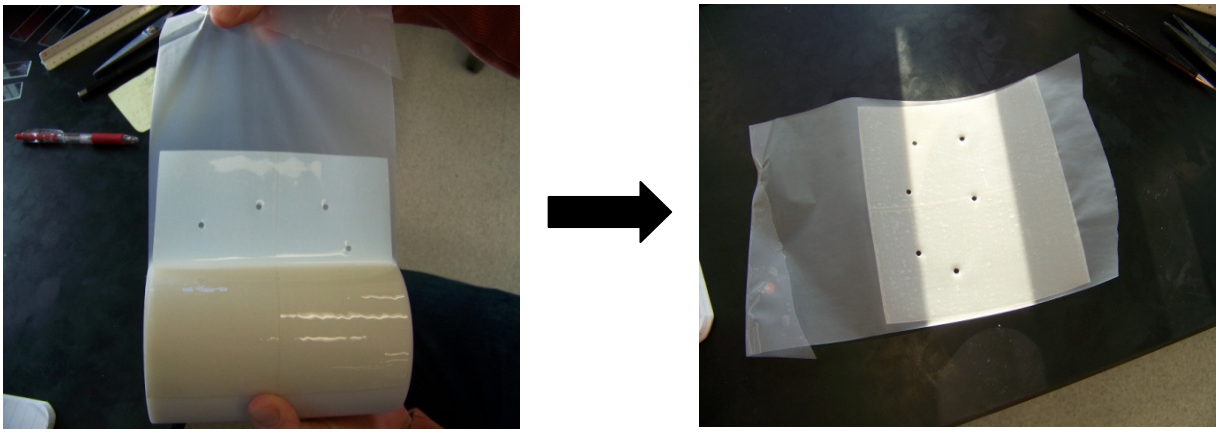

Figure 11. The PTFE is applied to the outside of a roll of Scotch tape. The PTFE is used for support and the Scotch tape is used for its effectiveness to remove sublayers from the glass substrate.

One at a time, the glass slides are placed face down onto the adhesive side of the Scotch tape in such a way that one end of the sublayer crosses the hole in the middle and the other end crosses a hole at the outer edge of the PTFE assembly, as shown in Figure 12. The PTFE assembly is then peeled from the glass slide so that the sublayer remains on the Scotch tape. This process is repeated until the desired number of sublayers have been applied, in this case, five, to form the sublayer assembly.

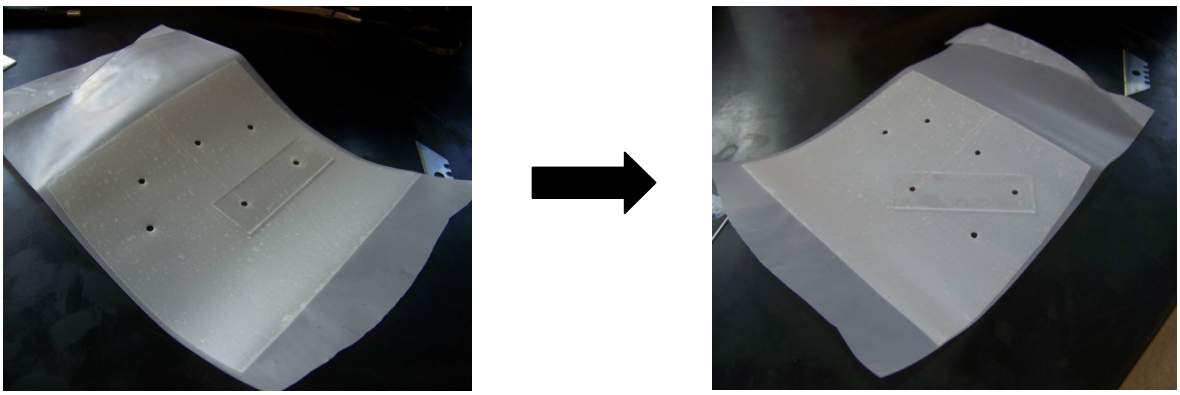

Figure 12. The glass slides are placed downward onto the Scotch tape. When they are peeled up, the sublayer crosses both the measurement hole and the center hole.

After all of the sublayers have been applied to the tape, it is necessary to cover the remaining Scotch tape adhesive to make the assembly easier to handle and implement into the fuel cell. For this, a thin Kynar film is used. 10 wt% Kynar 720 in DMAc is knife cast onto a glass substrate at 80 °C. The resulting dimensions of this film are approximately 7.5 cm x 10 cm x 6 µm. This is enough

area to fully cover the center hole and facilitate handling by reducing the exposed adhesive surface area. This film also prevents shorting between sublayers and the membrane after the Nafion membrane is added to the MES. The film is applied in a similar manner to the sublayers. Since there is enough exposed adhesive area, the sublayer assembly can be adhered to the Kynar film which is supported on a large glass substrate. The sublayer assembly with the attached Kynar film is then removed from the glass substrate. After excess material is trimmed, the entire MES is hot pressed at 115 °C, ~250 psi for 5-10 minutes to ensure secure bonding between each sublayer. The resulting MES resembles Figure 13.

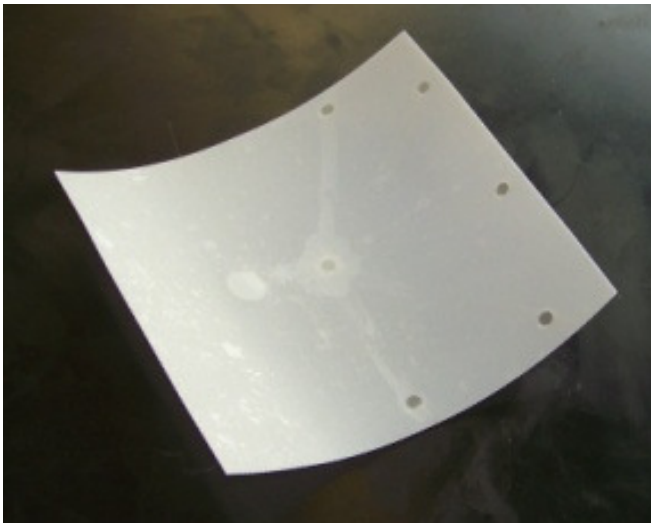

Figure 13. The resulting MES.

3.3.4 Cathode Catalyst Layer. After hot pressing, the next step is to drill a hole in the MES for the cathode catalyst layer. Three methods for making the hole were examined: focused ion beam (FIB), laser milling, and punching the hole after freezing the sample with liquid nitrogen. While using an FIB is more accurate, it is time consuming and expensive to use. Alternately, laser milling is extremely fast and inexpensive; however, there is some concern with smearing of the sublayers because of the heat generated by the laser. Similarly, freezing the sample and punching the hole is fast and inexpensive, however layer separation and debris removal may pose issues. The applicability of each method was explored.

With the help of the Nanoscale Characterization and Fabrication Laboratory (NCFL) at Virginia Tech a 100 µm diameter hole was milled using an FIB. The diameter of the hole is chosen such that the transport in the catalyst layer remains one dimensional and edge effects from the interface between the MES and the catalyst ink should be negligible. Figure 14 shows the result of the FIB drilling procedure.

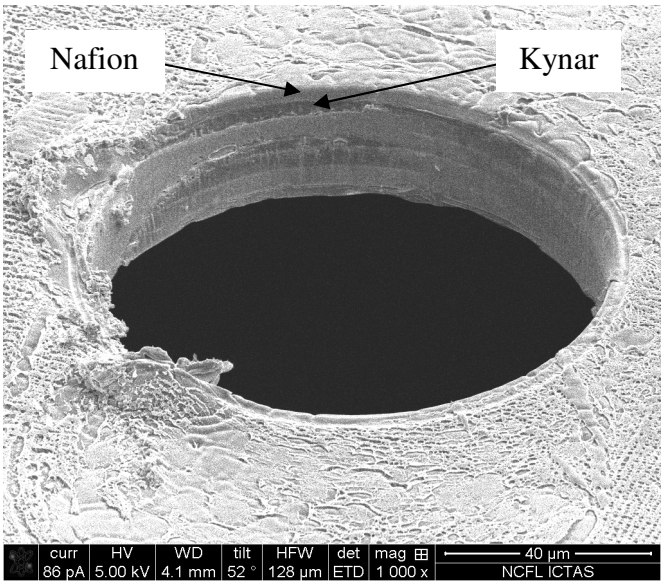

Figure 14. A 100 µm diameter hole is drilled through the sublayer assembly using a focused ion beam.

Figure 14 also gives a good perspective of the thickness of the sublayer assembly. Noting the scale in the figure, the thickness can be approximated at about 20 µm, which is less than half the thickness of the MES constructed by Hess et al. [3] and much closer to the thickness of an actual catalyst layer. Individual sublayers can also be seen and are indicated in Figure 14.

Alternately, the hole can be drilled using a laser mill (V-460, Universal Laser Systems, Inc.) provided by the Wood Science and Forest Products department at Virginia Tech. Figure 15 shows holes drilled in a practice sample.

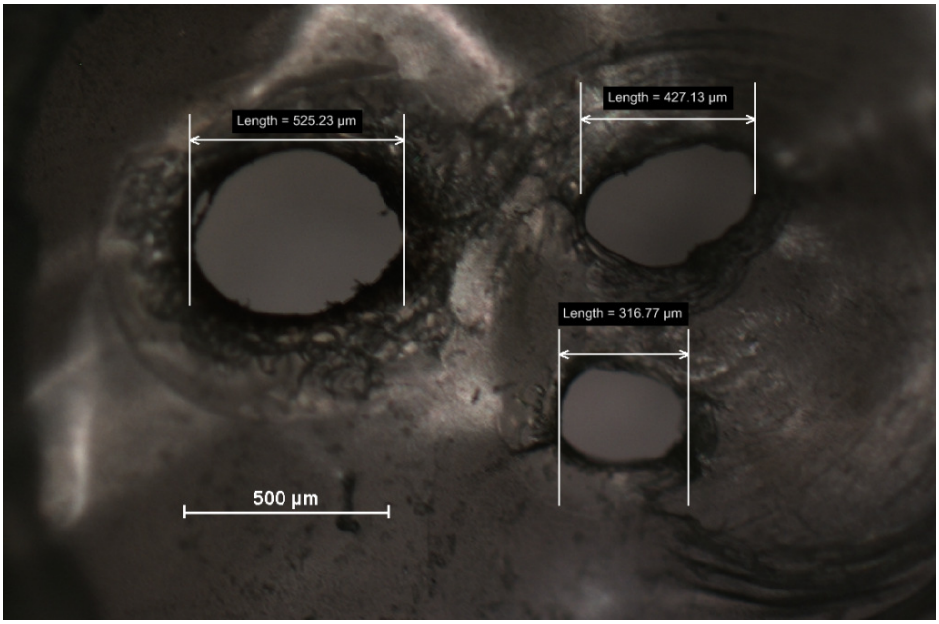

Figure 15. Holes drilled in a practice sample using a laser mill.

Each hole in Figure 15 is the result of an attempt to drill a 100 µm diameter hole. Each hole was drilled using different power settings on the laser. As seen from the figure, each hole is much larger than the desired 100 µm. Due to the power of the laser and the delicacy of the sublayers, it is very difficult to drill a hole of that size accurately because the laser tends to burn the material. This can be seen by the singeing type damage around the edges of each hole. This singeing is also undesired because it could short the layers. If one of the Nafion layers melts together with another, the ionic potential at discrete locations will no longer be measured. This singeing behavior could be due to the intended use of the laser. The laser is normally used to cut wood products, not delicate polymers, and singeing could be fixed with a further study into laser settings.

Note that Hess et al. [3] drilled their catalyst layer hole with this laser method and didn't see any shorting behavior between different sublayers. This could be attributed to the thickness of the insulating layer they used (7.5 µm). The larger insulating layer could prevent two Nafion layers from shorting together because there is a greater distance between them.

Another method for creating a hole in the MES is to freeze the sample and then punch the hole. In this approach, a sample MES was first immersed in liquid nitrogen until it was frozen. In order to demonstrate the capabilities of this method, the hole was punched with a syringe with a diameter of 400 µm. The result of the procedure can be seen in Figure 16.

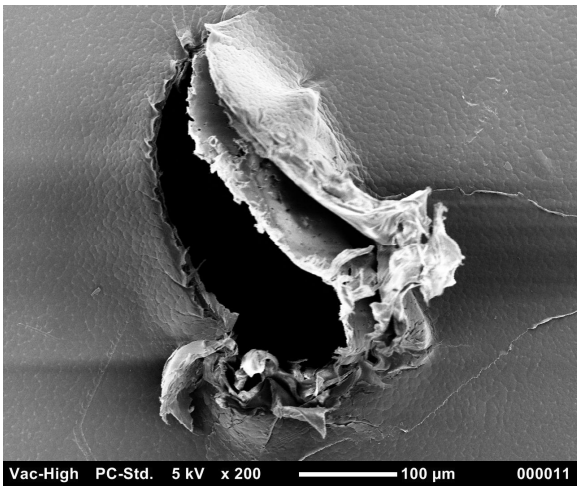

Figure 16. Results of a hole punched in a frozen MES.

From Figure 16, it can be seen that the syringe did successfully penetrate the MES, however, it performed this with more of a tearing than a punching action. The syringe left a flap of material still attached. The figure also suggests that the layers delaminated as seen from the separation of sublayers in the flap. While this method is easy and inexpensive, it is difficult to remove a whole piece of material without tearing, it is difficult to find an instrument that is capable of punching a hole 100 µm in diameter, and this method seems to separate sublayers. Because FIB can drill a hole of this size accurately without tearing or singeing the MES, it was chosen as the appropriate method for drilling the hole for the cathode catalyst layer.

After the hole is drilled, the membrane and catalyst layers can be added. Catalyst ink was prepared by first combining 17 mg of 39.1% platinum on Vulcan XC-72 (De Nora) and 0.2 mL of deionized water. 1 mL of isopropyl alcohol was then added and the mixture was sonicated for 30 minutes. The addition of the water prevents the platinum from reacting when the isopropyl alcohol is added. After mixing, 160 mg of 5 wt% Nafion in isopropyl alcohol (Ion Power, Inc.) was added and the mixture was sonicated for another 30 minutes. The resulting catalyst ink provides 0.4 mg-Pt/cm^2 loading with a Nafion/carbon ratio of 0.8 for a catalyst layer area of 12 cm^2.

A Nafion 211 membrane was hot pressed to the knife-cast Kynar side of the MES (opposite side of the PTFE sheet) at 115 °C for approximately 25 minutes. The anode catalyst layer was then applied to the membrane with an airbrush at approximately 80 °C. A mask was used when spraying the catalyst layer. The ink was sprayed within a 12 cm^2 area (since enough ink was prepared for a 12 cm^2 catalyst layer) with a 1 cm^2 cutout which exposes the anode side of the membrane. This creates an anode catalyst layer that is 1 cm^2. The mask is used because it is difficult to prepare catalyst ink for only 1 cm^2 with the properties mentioned above.

The cathode catalyst layer was then applied with an airbrush at approximately 80 °C. A similar masking method was used for the cathode catalyst layer. A 12 cm^2 catalyst layer was sprayed onto a mask with a 1 cm^2 cutout that exposes the 100 μm diameter hole in the MES. Assuming that the catalyst layer fully and uniformly fills the hole drilled in the MES (with a thickness of 20 μm from Figure 14), the theoretical porosity of the cathode catalyst layer can be calculated using Eq. (29) to be 67%. Before the MES was installed into the fuel cell, sufficient time was given to let the solvent evaporate out of the catalyst layers.

3.3.5 Ionic Potential Measurements. In order for the MES to be beneficial to this research, the ionic potential within each Nafion film must be measured. Hess et al. [3] achieved these measurements with the help of specially machined fuel cell hardware and hydrogen reference electrodes at each measurement point. Using the hydrogen reference electrodes, they were able to measure absolute values of potential through the catalyst layer.

In order to avoid machining custom endplates for reference electrodes, methods for measuring ionic potential differences between individual layers were investigated. One way of doing so is by attaching a highly conductive wire to the potential measurement locations on the MES (the outer holes in Figure 13). The MES is designed such that the outer holes in the PTFE expose the Nafion side of each sublayer. Gold wire (99.99%, 0.1 mm diameter) is attached to each measurement point with Nafion solution; as the solvent evaporates out of the solution, the gold wire is left attached to the Nafion film. Figure 17 shows an MES with the attached gold wires and sprayed catalyst layer.

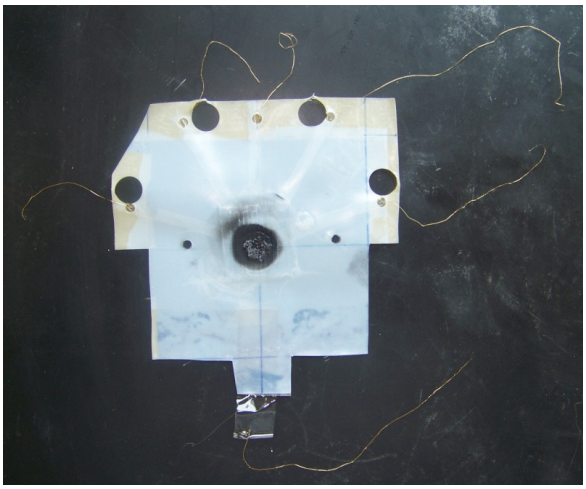

Figure 17. MES with gold wires attached to measurement points. The catalyst layer is sprayed and the GDL is installed.

In theory, this allows measurement of potential differences between layers within the catalyst layer by measuring the potential difference between different gold wires. As seen from the figure, one gold wire is also attached to the membrane so that potential differences can be measured between layers and the membrane.

One possible problem with this measurement technique is that the gold/Nafion union is exposed to oxygen in the atmosphere due to the design of the MES. This presents the possibility of a reduction reaction occurring with an unknown reduction potential. Although this reduction potential should not be reflected in the measurements since potential differences are being measured (as long as this reduction potential is the same at each gold/Nafion union), an alternate measurement technique was established to eliminate this possibility.

One method to eliminate the gold/Nafion union and any reduction reaction is to submerse the Nafion measurement point on the MES in a liquid electrolyte. A reference electrode can then be immersed in the liquid electrolyte and the potential can be measured from the reference electrode. The orientation of the MES/fuel cell assembly makes it difficult to immerse the measurement points in liquid electrolyte, so a reference electrode fixture was designed to fit around the MES and fuel cell fixture.

The design, which can be seen in Appendix D, immerses only the potential measurement points of the MES in an electrolyte solution (in this case, 1 mol/L sulfuric acid). The two part reference electrode fixture uses FEP encapsulated o-rings to prevent electrolyte leakage and allows for potential measurements to be taken with miniature Ag/AgCl reference electrodes (eDAQ, ET072). The reference electrode fixture was designed specifically for this MES design and the fuel cell fixture being used. Figure 18 shows the fixture installed on an MES.

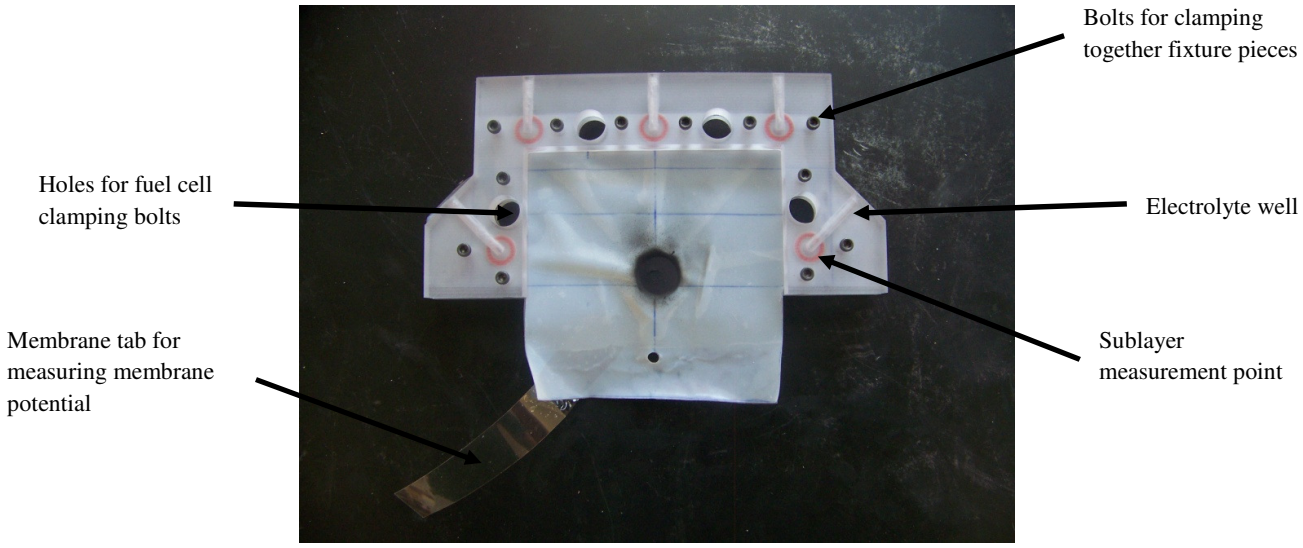

Figure 18. The reference electrode fixture installed on an MES eliminates the occurrence of a reduction reaction.

As seen from Figure 18, there are wells at each potential measurement point that are filled with sulfuric acid. The potential difference between two layers is measured by placing an Ag/AgCl reference electrode in the well associated with each sublayer and measuring the resulting potential difference. There is also a tab from the Nafion membrane that protrudes out of the MES. This tab can be submersed in sulfuric acid and can be used as another potential measurement point. Holes in the fixture accommodate the clamping bolts in the fuel cell fixture. While this reference electrode fixture does eliminate an unknown reduction potential, it still does not allow for the measurement of absolute potential values (it is only capable of measuring differences).

The final MES is an anode catalyst layer, PEM, and cathode catalyst layer with Nafion probes at discrete locations through the cathode catalyst layer, supported on a PTFE substrate. Either a reference electrode fixture or gold wires are used to attach a potentiostat to each measurement point to measure the ionic potential difference between discrete locations through the catalyst layer in the form of a voltage.

3.3.6 Integration/Installation into PEM Fuel Cell. Before data can be collected, the MES must be integrated with the fuel cell hardware. As mentioned before, no special hardware has to be manufactured for testing using this MES design. The cell hardware is a 5 cm^2 active area cell (Fuel Cell Technologies, Inc.). Anode and cathode end plates are held together using eight bolts and there are two guide pins to ensure alignment of end plates and flow channels; holes of the appropriate size are punched into the MES to accommodate these pins and bolts.

The gas diffusion layer for the anode is non-wet proofing carbon paper (Toray, TGPH-090) and is installed normally. The cathode gas diffusion layer is non-wet proofing carbon cloth (E-TEK, B1A). The carbon cloth is placed on top of the PTFE substrate over the center hole. When the fuel

cell is clamped, the flexible cloth is forced to contact the catalyst layer. After the gas diffusion layers are in place, the bolts and alignment pins are guided through the holes in the MES. The bolts are tightened to 9 in-lbs.

Cathode flow field/GDL/catalyst layer connectivity may be affected because of the method of GDL installation. Future research in MES design can focus on ensuring proper flow field/GDL/catalyst layer connectivity through flow field design, selection of a backing substrate that is thinner and more rigid than the PTFE used in this MES, or the shape/size of the center hole in the PTFE substrate. A cross-sectional schematic of the final MES is shown in Figure 19.

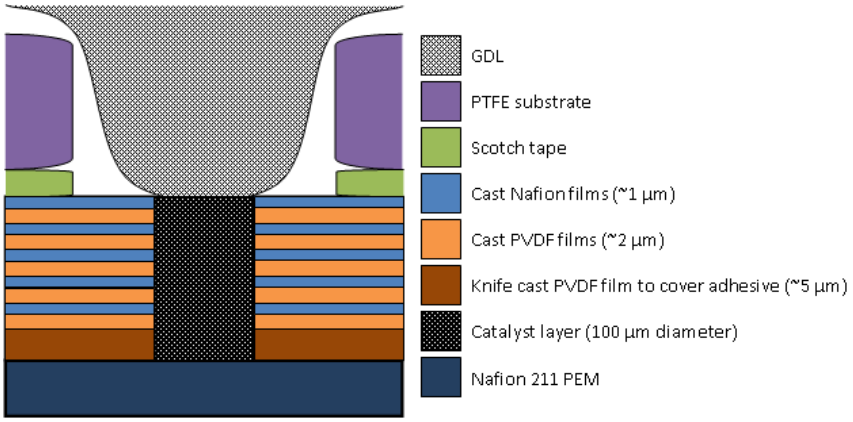

Figure 19. Cross-sectional schematic of the center hole of the constructed MES. The top is adjacent to the cathode flow channels while the bottom is adjacent to the anode catalyst layer. Note the thickness of the cathode catalyst layer is ~20 µm and there are five locations through the catalyst layer where ionic potential measurements can be taken.

3.3.7 Data Collection. Anode and cathode gas are supplied by a fuel cell testing station (Fuel Cell Technologies, Inc.). Humidified hydrogen is supplied at 100 sccm to the anode and humidified air is supplied to the cathode at 100 sccm. The cell temperature is held at 50 °C and is controlled by the fuel cell testing station. Because the area of the cathode catalyst layer is so small, the current will be too small to be measured by the fuel cell test stand. Thus, cell voltage control, current measurement, and sublayer voltage differential measurements are accomplished using a multi-channel potentiostat (1480 Multistat, Solartron Analytical).

Before testing, the fuel cell is allowed to reach steady state. Humidified nitrogen is supplied to the cathode and anode for at least 96 hours to ensure that the thin Nafion films become hydrated for ionic conductivity. Following this, humidified hydrogen and air (relative humidity of 100%) are supplied and polarization curves are taken to ensure steady state performance.

For performance information of the MES, one channel of the potentiostat both supplies the voltage and measures the corresponding current (operating in potentiostatic mode). When taking ionic potential measurements using the gold wire method, one channel drives the fuel cell by

maintaining a voltage, five other channels measure the potential between the cathode current collector and the respective gold wire, one channel measures the potential between the membrane and the cathode current collector, and one channel measures the potential between the membrane and the anode. It is important that the gold wires are not touching each other or another part of the fuel cell in order to avoid shorting/noise. When taking potential measurements with the reference electrode fixture, one channel drives the fuel cell by maintaining a voltage and another channel measures the potential between two sublayers, as seen in Figure 20.

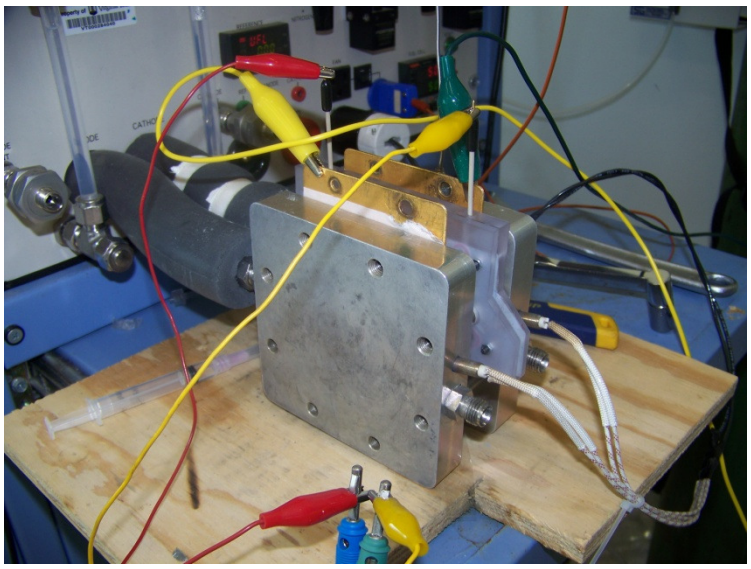

Figure 20. Experimental setup using the reference electrode fixture. The setup for the gold wire method looks similar, although there are additional channels measuring potential at each layer simultaneously.

As seen from Figure 20, only one measurement at a time can be taken using the reference electrode fixture since there are only two Ag/AgCl reference electrodes. Typically, the cell voltage is held constant for an extended period of time to achieve steady state behavior while ionic potential is measured in each sublayer. The voltage is then changed and the measurements are taken at a different set point. Post-processing is done using MatLab and Excel.

4. Results and Discussion

4.1 Microstructure Reconstruction. As stated previously, two different numerical microstructures were created using different stochastic realizations; that is that the perturbation from the nominal porosity is different in each microstructure. These two microstructures are referred to as reconstructed catalyst layer 1 (RCL1) and reconstructed catalyst layer 2 (RCL2) throughout this paper and can be seen in Figure 21 and Figure 22.

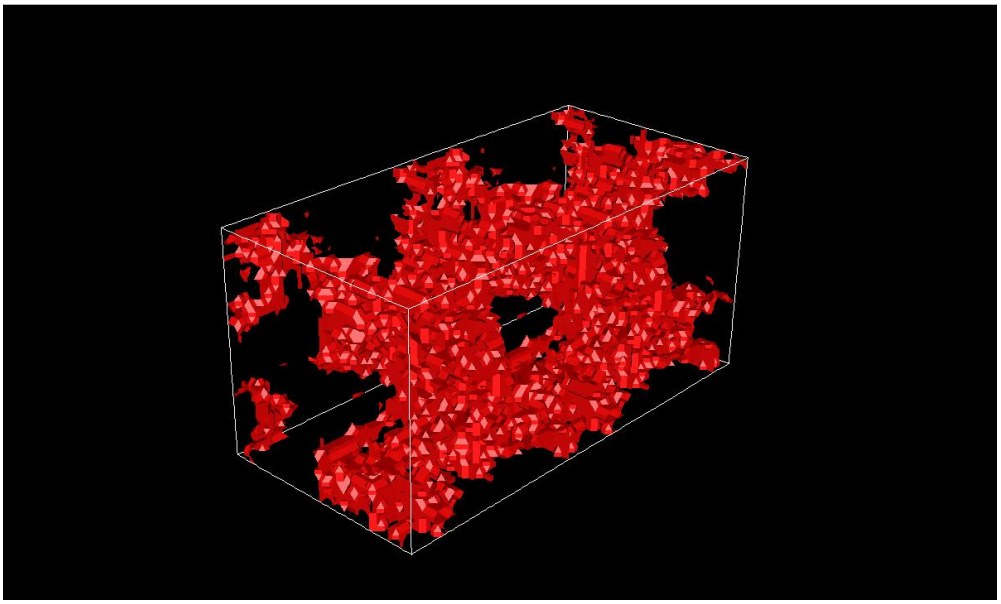

Figure 21. Reconstructed catalyst layer 1. The red phase represents the electrolyte (solid) phase.

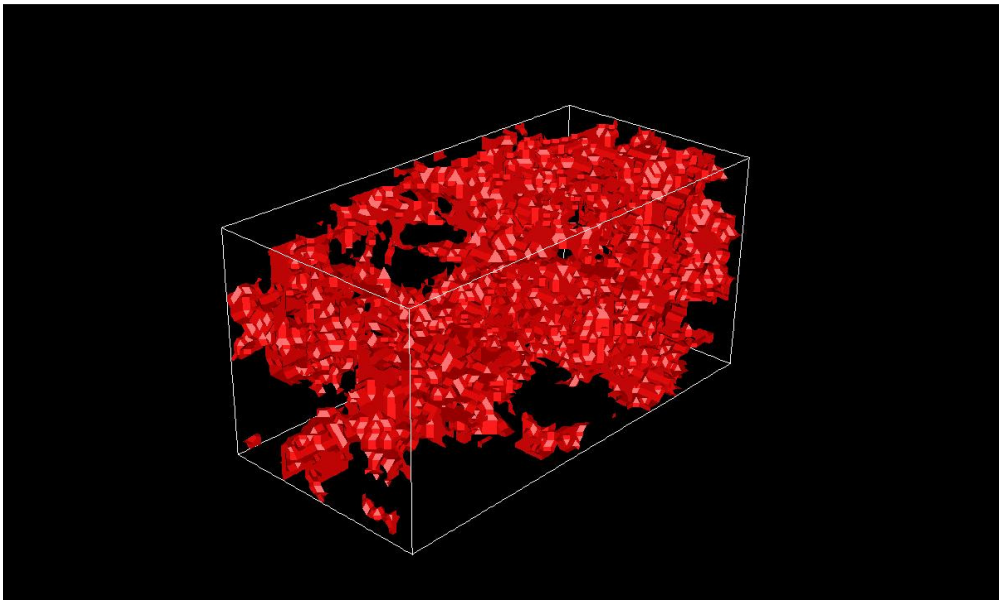

Figure 22. Reconstructed catalyst layer 2. The red phase represents the electrolyte (solid) phase.

As seen from the figures, the microstructures are binary; the red phase indicates the solid phase within the porous matrix. Both microstructures are generated such that the nominal porosity of the catalyst layer is 60% with a thickness of 20 µm. Actual porosities are 59.9% and 60.1% for RCL1 and RCL2, respectively. The overall thickness of the microstructures is 20.4 µm including the single layer of void and electrolyte phase for implementation of boundary conditions.

Figure 23 shows the local pore volume fraction distributions across the thickness of the catalyst layer. As seen, both microstructures yield an overall porosity around 60%, but they accomplish this in different ways. RCL1 has a relatively larger, but more uniform, deviation around 60% while RCL2 has a smaller deviation around 70% but has an area where there is a significant drop-off in the porosity around 15 µm from the membrane. This effect becomes visible in the simulations as the large reduction in porosity chokes oxygen diffusion to a large part of the catalyst layer.

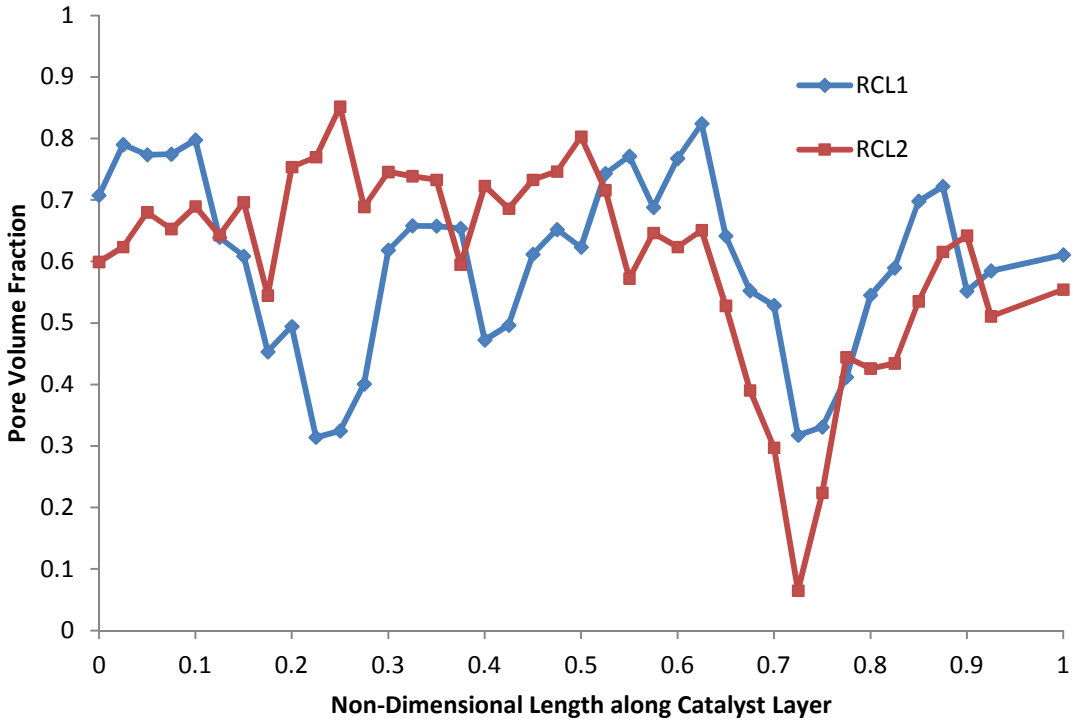

Figure 23. Pore volume fraction for RCL1 and RCL2.

4.2 Modeling MES Polarization Curves. In order to obtain polarization curves with the DNS, it must be run at individual current densities for each microstructure. Using Eq. (30), the cell voltage can be calculated and the polarization curve can be plotted. Figure 24 shows a polarization curve at 50 °C and 100% relative humidity, assuming a typical high frequency resistance value of 100 mΩ-cm^2 and minimal liquid water blockage.

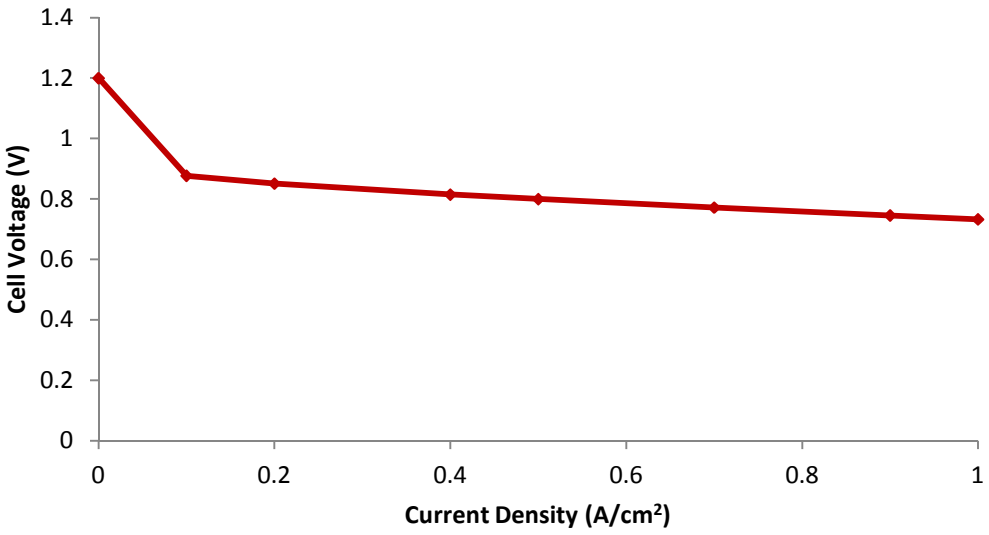

Figure 24. DNS predicted polarization curves at 50 °C, 100% RH, and HFR = 100 mΩ-cm^2.

As seen from the figure, the polarization curve shows a fast drop in voltage at smaller current densities controlled by the kinetics of the oxygen reduction reaction and at intermediate values of current density the curve exhibits a linear voltage drop. The sharp drop-off in voltage at higher current densities is not apparent due to the DNS inputs and will be discussed further in future sections.

4.3 Experimental Polarization Curves. Six different MES were constructed and tested throughout this research. Details about each MES can be seen in Table 1.

Table 1. Methods for drilling catalyst layer hole and taking ionic potential measurements for each MES tested.

MES	Details
MES 1	FIB hole, gold wire method
MES 2	FIB hole, gold wire method
MES 3	Laser drilled hole, gold wire method
MES 4	FIB hole, gold wire method
MES 5	FIB hole, reference electrode fixture method
MES 6	FIB hole, reference electrode fixture method

Polarization curves were obtained for all six MES, however, only one MES provided reasonable ionic potential measurements (MES 6 using the reference electrode fixture). The MES that was built using the laser to drill the hole for the cathode catalyst layer exhibited shorting between layers (see Section 4.4.1), and hence the rest of the MES used the FIB for drilling the hole.

Overall fuel cell performance increased with time as the MES hydrated. Because very little water is produced in the cathode catalyst layer due to its size, the fuel cell took hours to reach steady state

performance. Figure 25 and Figure 26 show polarization and power density curves for MES 1. As seen from the figures, the overall cell performance increases with time until it eventually reaches a state of steady maximum performance. All other MES showed similar behavior, although overall maximum performance varied with MES.

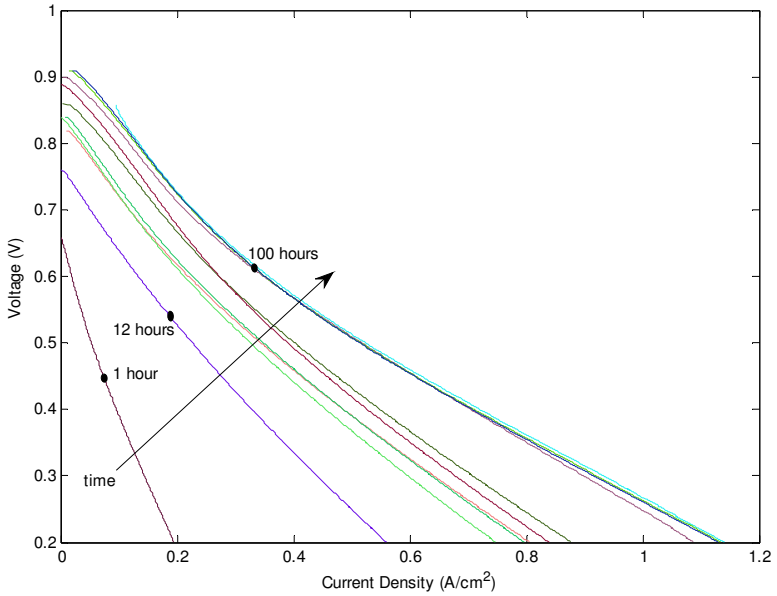

Figure 25. Polarization curve for MES 1. Performance reaches a steady state after the MES fully hydrates.

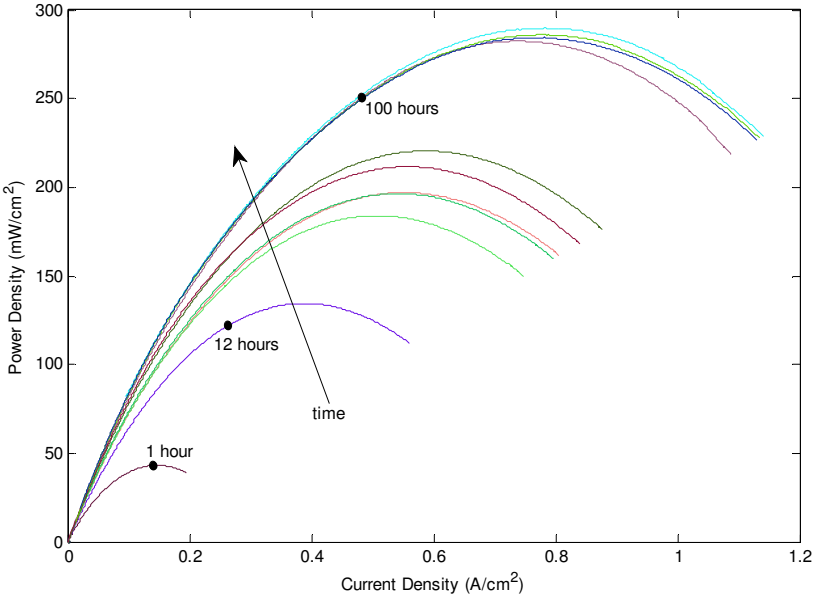

Figure 26. Power density curves at different times for MES 1.

Maximum overall fuel cell performance varied with each MES and can be seen in Figure 27. Most MES exhibited poor performance. The relatively steep slopes of the polarization curves seen in Figure 27 suggest that the MES are experiencing a large Ohmic type loss. This Ohmic loss can be attributed to either poor catalyst layer/membrane/GDL connectivity or high catalyst layer ionic resistance. Other possible causes of poor performance include poor catalyst utilization and liquid water blocking pores in the cathode catalyst layer and/or gas diffusion layer.

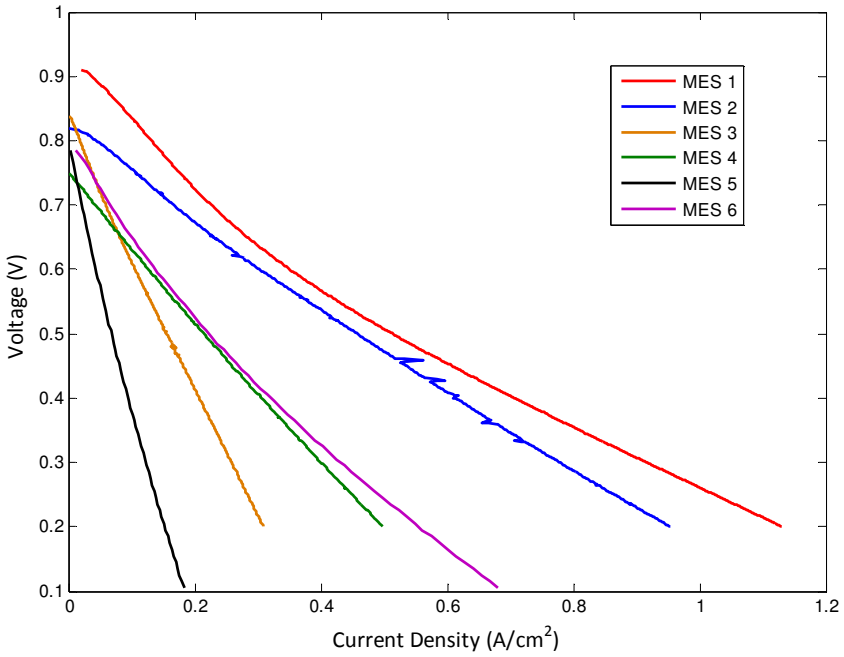

Figure 27. Steady state performance of each MES constructed.

Comparing experimental polarization curves in Figure 27 to the DNS polarization curve in Figure 24, it can be seen that experimental polarization curves exhibit much lower performance. Membrane/catalyst layer/GDL connectivity, liquid water generation, and catalyst layer conductivity were explored to find which had the greatest effect on DNS polarization curves. Variables were then adjusted in the DNS accordingly to account for these factors and predict polarization curves more accurately.

4.3.1 Membrane/Catalyst Layer/GDL Connectivity. The MES is constructed such that the cathode catalyst layer must be sprayed into a hole that is 100 µm in diameter. If the catalyst ink is agglomerated or sprayed unevenly, there may not be good connectivity between the catalyst layer and the membrane. A useful method to characterize not only connectivity between the catalyst layer and the membrane, but also the catalyst layer and the gas diffusion layer, is electrochemical impedance spectroscopy (EIS). Using EIS, the Ohmic resistance of the fuel cell can be found, also known as the high frequency resistance (HFR). Eq. (30) uses the HFR to directly calculate the numerical polarization curves; and increasing the HFR can reduce the cell performance drastically.

EIS was performed on MES 6 in order to find the appropriate HFR value to use in Eq. (30). Voltage was swept from 100,000 Hz to 100 Hz with amplitude of 10 mV. Figure 28 shows the results of the EIS. The HFR for MES 6 is taken to be the real component of impedance at 10,000 Hz, or 234 mΩ-cm^2. This HFR is not out of the ordinary, indicating sufficient connectivity throughout the fuel cell and MES. DNS polarization curves are re-plotted with the measured HFR value. The effects of changing the HFR can be seen in Figure 29. The HFR would have to be much larger to explain the disparity between DNS predictions and experimental results.

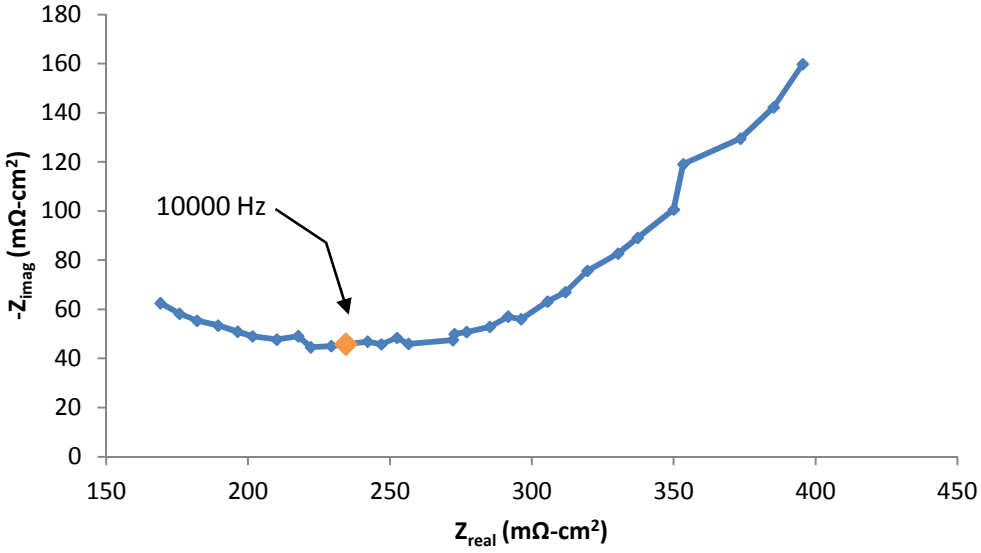

Figure 28. EIS from 100 Hz to 100,000 Hz. HFR taken at 10,000 Hz to be 234 mΩ-cm^2.

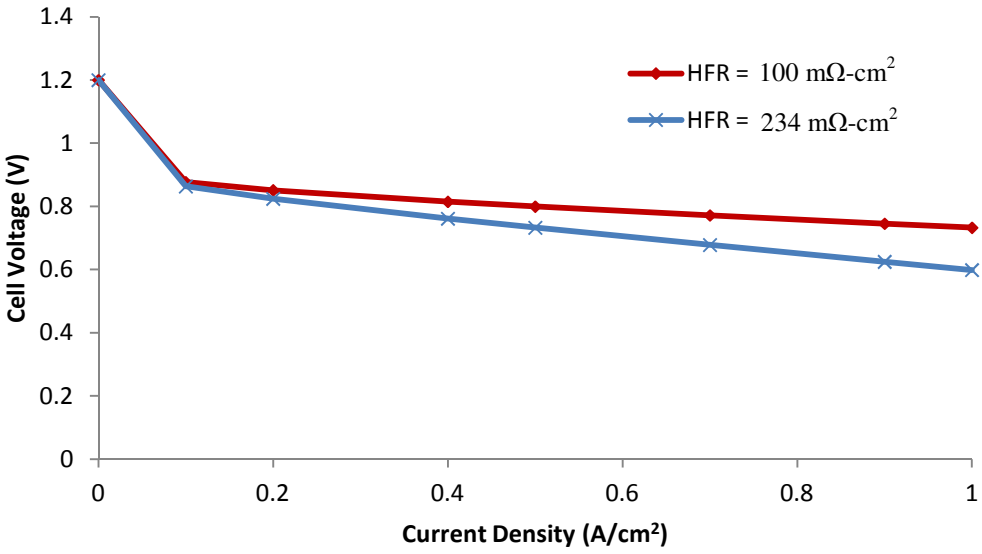

Figure 29. DNS polarization curves with the measured HFR. Increasing the HFR reduces calculated performance.

Although using the appropriate HFR value is important, it is not the factor that is causing the large discrepancies between the DNS and experimental polarization curves. The measured HFR value confirms membrane/catalyst layer/GDL connectivity and that the performance reduction is due to another phenomenon.

4.3.2 Effects of Liquid Water. In the DNS model, all the water produced is assumed to be in the vapor form; that is that the DNS does not account for liquid water. Liquid water can affect the overall performance of the fuel cell because droplets can block pores in both the gas diffusion layer and the catalyst layer, inhibiting oxygen transport.

Since MES are operated at relatively high relative humidity, there is certainly the possibility of liquid water condensation within the GDL. While the DNS does not physically account for liquid water, there are other ways to increase mass transport losses. One way to do this is to decrease the porosity and/or increase the tortuosity of the GDL and/or catalyst layer. Increasing the GDL tortuosity mimics liquid droplet formation in the GDL, requiring that the oxygen diffuse through a more tortuous gas diffusion layer and consequently reducing the oxygen concentration boundary condition into the catalyst layer. Lower catalyst layer porosity imitates the effect of liquid water blocking pores and inhibits oxygen from reaching an electrochemically active site. In order to avoid reconstructing another numerical catalyst layer, properties of the GDL, specifically the tortuosity, were adjusted to simulate the effects of liquid water. Note that all of the water generated in the catalyst layer is still assumed to be in the vapor phase but in reality, there could be liquid water blocking pores in the catalyst layer.

Figure 30 shows the DNS polarization curve with GDL tortuosity of 4 compared to the polarization curve shown in Figure 29 (tortuosity of 1.5). Both polarization curves in Figure 30 account for the experimentally measured HFR of 234 mΩ-cm^2.

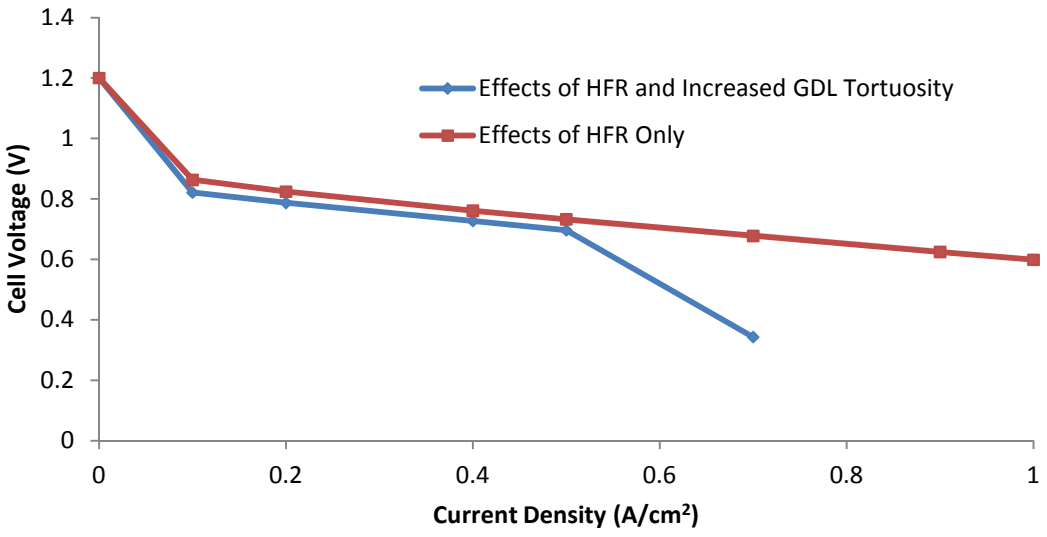

Figure 30. The effects of the GDL tortuosity on DNS polarization curves.

As seen from the figure, the increase of GDL tortuosity tends to slightly reduce the overall performance at intermediate values of current density but decreases cell performance drastically at higher current densities. The large voltage drop at higher current densities is attributed to the low oxygen concentration at the interface between the catalyst layer and the gas diffusion layer due to an increase of the oxygen diffusion resistance through the GDL to the catalyst layer as a result of the increase in the tortuosity of the GDL.

While the effects of liquid water are certainly important, the experimental polarization curves shown in Figure 27 exhibit more of an Ohmic type loss in the fuel cell as opposed to a mass transport type loss. For this reason, the ionomer conductivity within the catalyst layer was investigated.

4.3.3 Ionic Conductivity of Ionomer within the Catalyst Layer. In order to account for the Ohmic type loss in the experimental polarization curves, the effects of low ionic phase volume fraction and highly tortuous ionomeric pathways are considered. These were accounted for by decreasing the value of the Bruggeman correction in Eq. (23). Because the thickness of the ionomer within the catalyst layer is so small and because the ionic network is so tortuous, the resistance to proton transport will be higher and adjusting the value of the Bruggeman correction can account for this resistance. Figure 31 shows the DNS polarization curve at 50 °C, 100% relative humidity, and increased protonic resistivity compared to the polarization curve taken with MES 1 (50 °C, 100% relative humidity). Assuming an ionomer volume fraction of 0.13 and a porosity of 0.6, the exponent used in the Bruggeman correction was 7 to obtain the DNS polarization curve. The high frequency resistance of MES 1 is assumed to be similar to MES 6 (234 mΩ-cm^2).

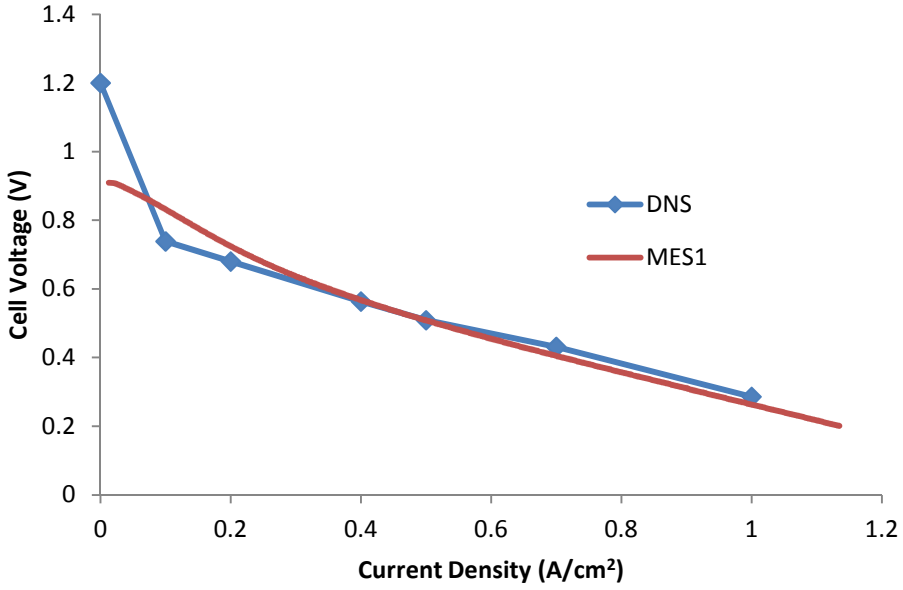

Figure 31. DNS polarization curve compared to MES1 polarization curve; both at 50 °C and 100% relative humidity.

As seen from the figure, the DNS can predict the polarization curve at the same operating conditions for MES 1 with the Bruggeman adjustment. There is, however, a large difference in the open circuit voltage. This can be attributed to hydrogen crossover, poor hydration, or even catalyst degradation in the small catalyst layer. Linear sweep voltammetry was applied to measure the hydrogen crossover current, however, results were inconclusive.

Increasing the protonic resistance of the ionomer in the DNS by adjusting for the tortuosity and thickness of the ionomer (adjusting Bruggeman correction) can produce a polarization curve similar to MES 1. MES 6, however, exhibits a much larger Ohmic type loss than MES 1 that cannot be accounted for solely by the increase in protonic resistance due to the tortuosity of the ionomer within the catalyst layer (there is a physical limit on the value of the exponent in the Bruggeman correction that should be used). In order to match the MES 6 polarization curve, the ionic conductivity had to be reduced further by decreasing the water content in the ionomer. Increasing temperature and reducing relative humidity in the DNS model reduces the water content within the Nafion ionomer and consequently reduces the intrinsic conductivity of the ionomer (κ_o in Eq. (23)). Figure 32 compares the experimental MES 6 polarization curve to a DNS polarization curve that accounts for the resistivity to proton transport due to the tortuosity of the ionomer and insufficient hydration of the ionomer.

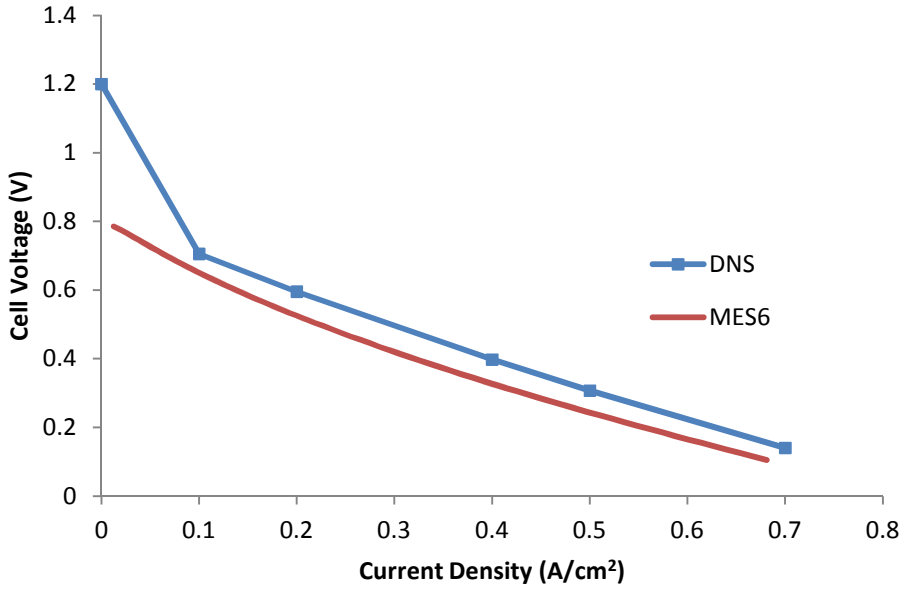

Figure 32. DNS polarization curve at 40% relative humidity and 90 °C compared to MES 6 polarization curve taken at 100% relative humidity and 50 °C.

Experimental polarization curves indicate a large Ohmic type loss in the MES. DNS simulations suggest that this Ohmic type loss can be attributed to an increase in protonic resistance of the ionomer within the catalyst layer due to the high tortuosity and small thickness. This result implies that the ionic conductivity of bulk Nafion and Nafion within a catalyst layer can be very different.

DNS results also suggest that, although operating at 100% relative humidity, the ionomer within the catalyst layer may still not be fully hydrated. This could be attributed to the small amount of water that is being produced on the cathode.

A portion of the Ohmic type losses seen in the experimental polarization curves could also be attributed to the catalyst layer manufacturing. If the volume fraction of the ionomer within the catalyst layer is not as high as expected there would be an increase in proton transfer resistance as the DNS suggests. Also, if the electrochemically active surface area within the catalyst layer is not as high as expected due to agglomeration of catalyst ink, the polarization curves would exhibit a large Ohmic type loss as seen in the experimental polarization curves. This highlights the importance of a uniform catalyst layer and some of the difficulties associated with spraying a 100 µm diameter catalyst layer.

4.4 Through-Plane Ionic Potential. Figure 33 illustrates the numbering system used and locations of each sensing layer within the MES. The PVDF portion of each sublayer is assumed to be 2 µm thick. The Nafion portion of each sublayer is assumed to be 1 µm and the knife-cast PVDF layer is assumed to be 5 µm. The total thickness of the catalyst layer is thus 20 µm. Layer 1 is designated as the layer adjacent to the cathode gas diffusion layer and layer 5 adjacent to the membrane. An example illustration of a through-plane ionic potential profile is also shown in Figure 33. This gives an idea of how the magnitude of voltage differences between each layer compare; for example, there will be a larger ionic potential difference between layer 5 and layer 4 than there will be between layer 2 and layer 1.

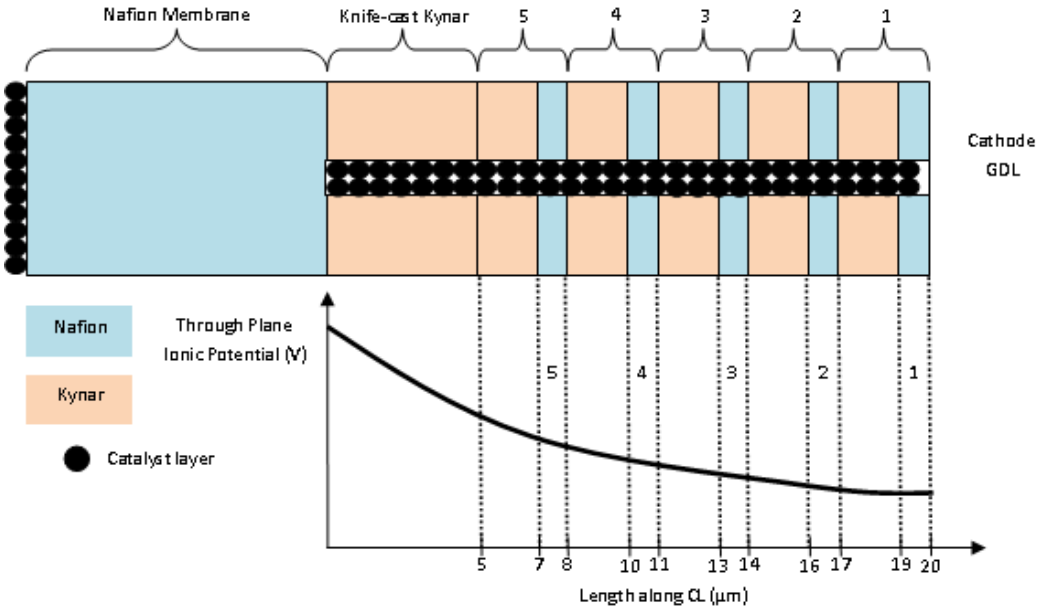

Figure 33. Location of each sublayer within the MES. An example potential profile is shown.

Through-plane ionic potential measurements proved to be difficult to take. The main problems when taking potential measurements were shorting between layers and discontinuities between the measurement point and the cathode catalyst layer. These issues are explained in Sections 4.4.1 and 4.4.2. Although some measurements showed the expected trends, there were issues with repeatability. The best results were obtained from MES 6 which used the reference electrode fixture and are shown in Section 4.4.3. The potential measurements from MES 6 are compared to the DNS results in Section 4.4.4.

4.4.1 Shorting Between Layers. In MES 3 (with the laser-drilled hole), shorting between the sublayers and/or the membrane caused each sublayer to measure the same potential as the membrane. Figure 34 shows the measured potential at each measurement point and at the membrane referenced to the cathode current collector in MES 3.

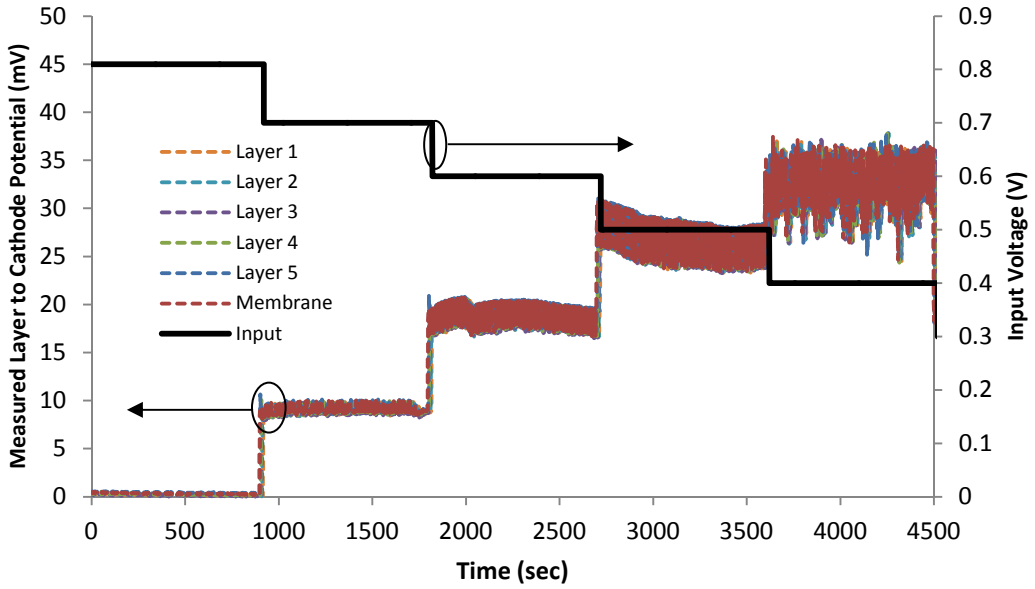

Figure 34. MES 3 (with the laser-drilled hole) exhibited signs of shorting between the Nafion sensing layers and the membrane.

Referencing Figure 34, the operating voltage was controlled potentiostatically and stepped from 0.8 V to 0.4 V (increasing current density). The potential was measured on separate channels of a potentiostat between the cathode current collector and each sensing layer's measurement point (gold wire). The potential between the membrane and the cathode current collector was also measured. As seen from the figure, the potential measurements follow the correct trend. As the voltage is decreased (increasing current density), there should be an increasing voltage difference across the catalyst layer. This is because the higher current draw requires more protons to be transported across the membrane and into the cathode catalyst layer.

As seen from the figure, the potential measured between the current collector and each layer follows the potential measured between the membrane and the current collector. This behavior

suggests that all of the layers are shorted to the membrane. Figure 35 shows this result more clearly by measuring each layer with respect to the membrane. As seen, the potential difference between each layer and the membrane is zero, indicating that there is a short. In this case, the input voltage was swept, as if taking a polarization curve and the membrane was measured with respect to the current collector.

Unfortunately, many MES showed the correct trend of potential with decreasing operating voltage like this one, however, there was shorting behavior or the magnitudes of the measured voltages were unreasonable. Some measurements were also very noisy. As seen in Figure 34, the measurement becomes more and more erratic at higher current densities.

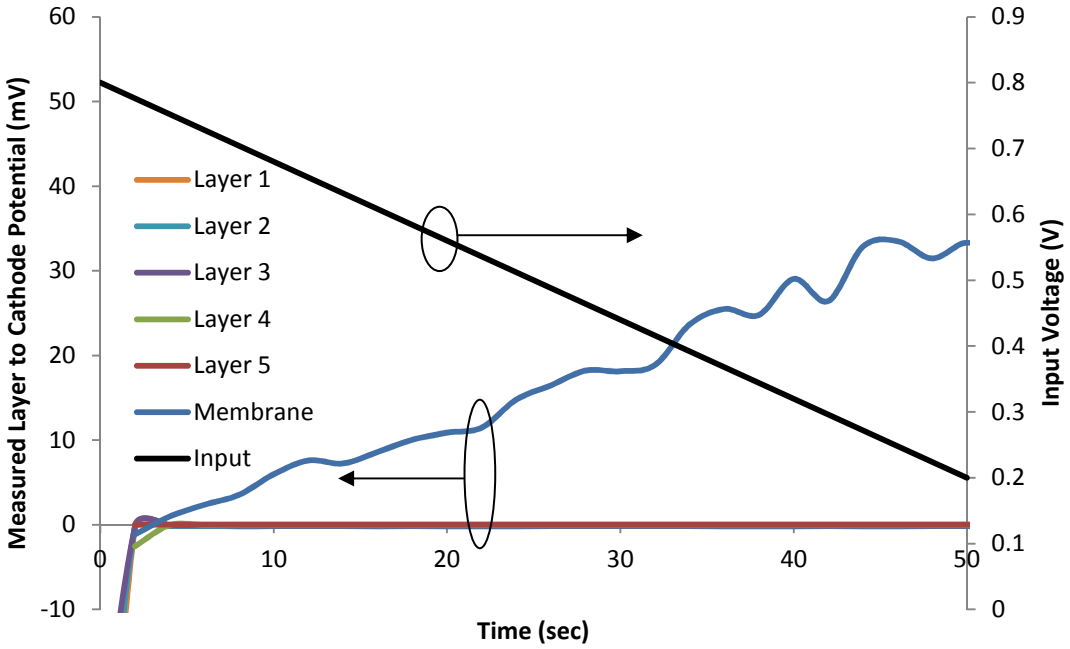

Figure 35. The potential measured between the layers and the membrane is zero, indicating a short.

This shorting behavior can be described in two ways; the Nafion portion of each sublayer physically contacts the membrane or there is a short between the layers within the hole. Although the former is possible, it is highly unlikely since there are at least two films of PVDF separating each Nafion layer from the membrane; the PVDF portion of the sublayer and the knife cast PVDF adjacent to the membrane. The Nafion layers are most likely shorted together due to the laser method used to drill the catalyst hole. Since the hole is so small and the thin sublayers so delicate, the heat from the layers probably singed the edges, melting the Nafion sensing layers together (see Figure 15). When the membrane was hot pressed onto the MES, there was then contact between this singed area and the membrane, causing a short between all of the layers and the membrane. For this reason, the remainder of the MES were drilled with FIB.

4.4.2 Open Circuit Layers. Some MES exhibited potential measurement readings that suggested that there was a discontinuity between the catalyst layer and the potential measurement point. This was confirmed by examining the voltage reading with the potentiostat attached to the MES, removing the potentiostat, and seeing no corresponding change in the voltage. The discontinuities can occur at the interface between the catalyst layer and the Nafion sensing layer, in the middle of the Nafion layer, or can be caused by insufficient hydration of the thin Nafion layer.

The catalyst ink is applied into the 100 µm diameter hole using an airbrush. If the ink has agglomerated or there is insufficient coverage of catalyst ink into the hole, there could be some points where the catalyst ink does not contact the Nafion sensing layers. This situation is shown in Figure 36 and would cause an open circuit voltage to be measured by the potentiostat at these layers.

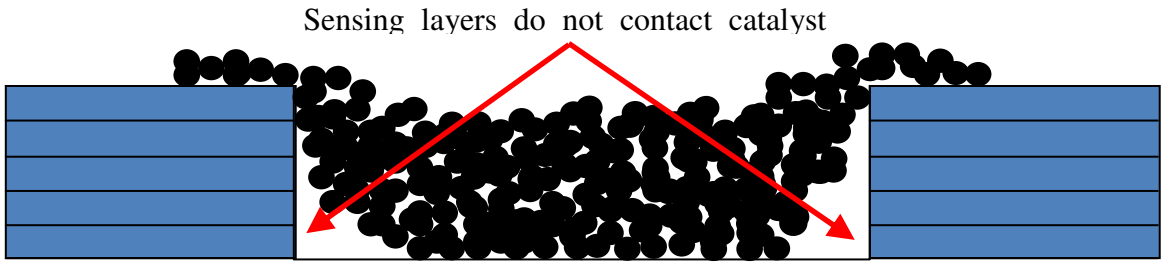

Figure 36. If catalyst ink does not contact the Nafion sensing layers then there will be an open circuit.

Another possible reason for an open circuit is if there is a discontinuity in the Nafion sensing layer. Due to the design of the MES, the lengths of the sublayers from the catalyst layer to the ionic potential measurement points are quite long (~6 cm). This large length leaves a greater possibility for discontinuities/defects in the Nafion layer which could impede the flow of the hydrogen ions.

The Nafion sensing layer within each sublayer is also very thin compared to its length (~1 µm). Since there is not a lot of water being produced on the cathode, sufficient time is needed for these thin Nafion layers to be hydrated by the humidified gas in order to become ionically conductive. An improved MES design that reduces overall sublayer length may yield more reliable ionic potential measurements.

4.4.3 Experimental MES Responses. MES 6 provided the most reliable ionic potential measurements. The fuel cell was held constant at an operating voltage of 0.5 V (which corresponds to an operating current density of ~0.2 A/cm^2 according to the polarization curve in Figure 27) and operated at 50 °C and 100% relative humidity. Ionic potentials were measured using the reference electrode fixture with Ag/AgCl reference electrodes. It was found that there was an offset of 16 mV between the reference electrodes. Measured voltages between layers are presented in Figure 37. The 16 mV offset is removed from the data in Figure 37.

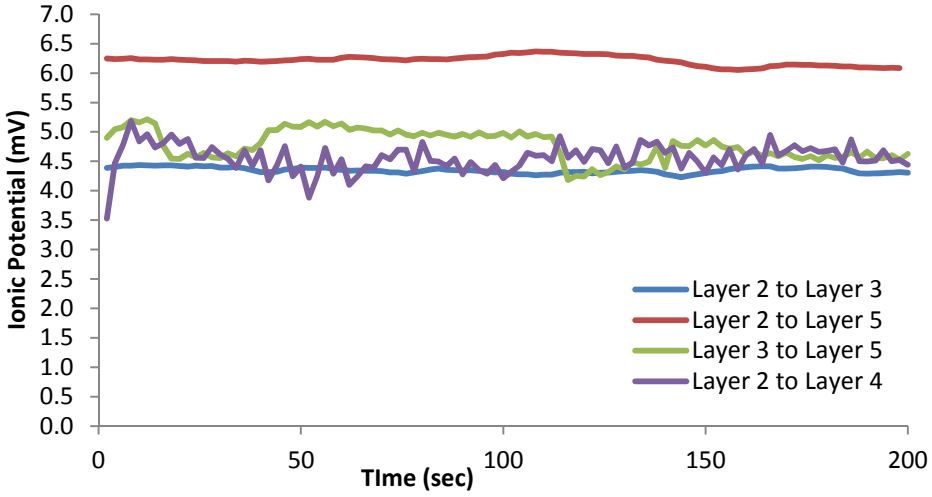

Figure 37. Measured ionic potential between different layers at an operating voltage of 0.5 V.

4.4.4 Predicting Profiles with DNS. The direct numerical simulation model was performed at 50 °C, 100% relative humidity, and 0.2 A/cm^2. The ionic potential through the cathode catalyst layer was plotted for each microstructure and can be seen in Figure 39. Note that there is a thickness associated with each Nafion sensing layer (1 µm) and there is a potential gradient across this thickness. In order to find the difference between different sublayers in the DNS, a location within each sensing layer must be chosen. For example, potential differences between layers can be found using ionic potential values located directly in the center of each sensing layer, average ionic potential across the sensing layer, etc. In this case, the edges closest to one another were chosen. For example, if measuring the difference between layer 5 and layer 3, the potential at the membrane side of layer 3 (13 µm in Figure 33) is subtracted from the potential at the GDL side of layer 5 (8 µm in Figure 33). If measuring the difference between layer 3 and layer 2, the potential at the membrane side of layer 2 (16 µm) is subtracted from the potential at the GDL side of layer 3 (14 µm). Potential values at the appropriate locations are indicated in Figure 39.

It should be noted that although MES 6 provided the most reliable results, the potential difference between all combinations of layers were not obtained due to erratic measurements. These erratic values can be attributed to poor connectivity between the sensing layer and catalyst layer, discontinuities in the layer, or poor layer hydration as explained in Section 4.4.2.

Table 2 tabulates the information obtained from Figure 37 and Figure 39. The experimental data reported in Table 2 represents an average of the data collected from $0 < t < 200$ seconds in Figure 37. As seen from the table, there is fairly significant error between the experimental and numerical results. The error is very significant between layer 2 and layer 3 for both microstructures. This suggests that the actual potential profile within the catalyst layer towards the GDL does not level off as much as the DNS predicts. As seen from Figure 39, there are much larger potential gradients towards the membrane (more so in RCL2 than RCL1), obviously because there is a higher concentration of protons that are entering the catalyst layer through the membrane. Unfortunately,

due to the design of the MES, this gradient cannot be measured. The knife-cast PVDF sheet is too thick for the MES to capture what is occurring in this region.

Table 2. Comparison of experimental and DNS ionic potential differences.

Layer 1	Layer 2	Layer 3	Layer 4	Layer 5	Experimental (mV)	DNS, RCL2 (mV)	|Difference| (mV)	% Error	DNS, RCL1 (mV)	|Difference| (mV)	% Error
	■			■	6.3	7.0	0.8	10.7	8.8	2.6	29.0
		■		■	5.0	5.9	0.9	15.3	6.7	1.7	25.4
	■		■		4.5	3.1	1.4	-45.2	6.0	1.5	25.0
	■	■			4.4	0.3	4.1	-1360	0.6	3.8	-633
						Average % error excluding outlier		23.7	**Average % error excluding outlier**		26.5

The average error excluding the outlier (layer 2 to layer 3) is 23.7% for RCL2 and 26.5% for RCL1. Errors could be due to the noise in the measurement (see Figure 37) or because the exact location of each sublayer within the microstructure is unknown. While there is significant difference between predicted and measured ionic potential differences, both results follow the same trend; that is layer 2 to 5 shows the greatest difference, followed by layer 3 to 5, layer 2 to 4, then layer 2 to 3. Figure 38 shows the information in Table 2 in graphical form.

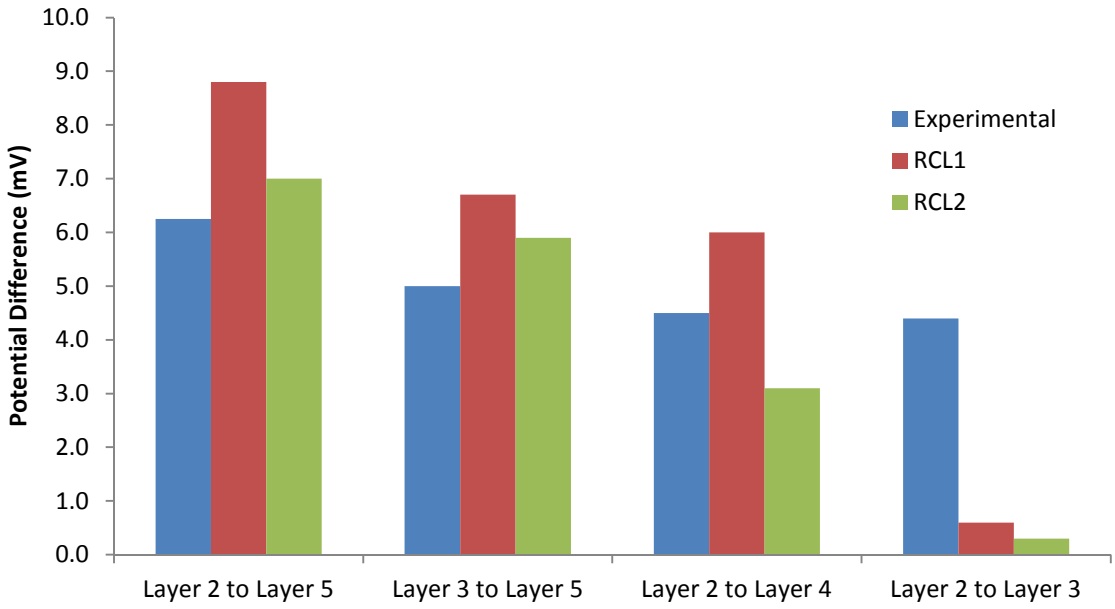

Figure 38. Visual comparison of experimental and numerical results.

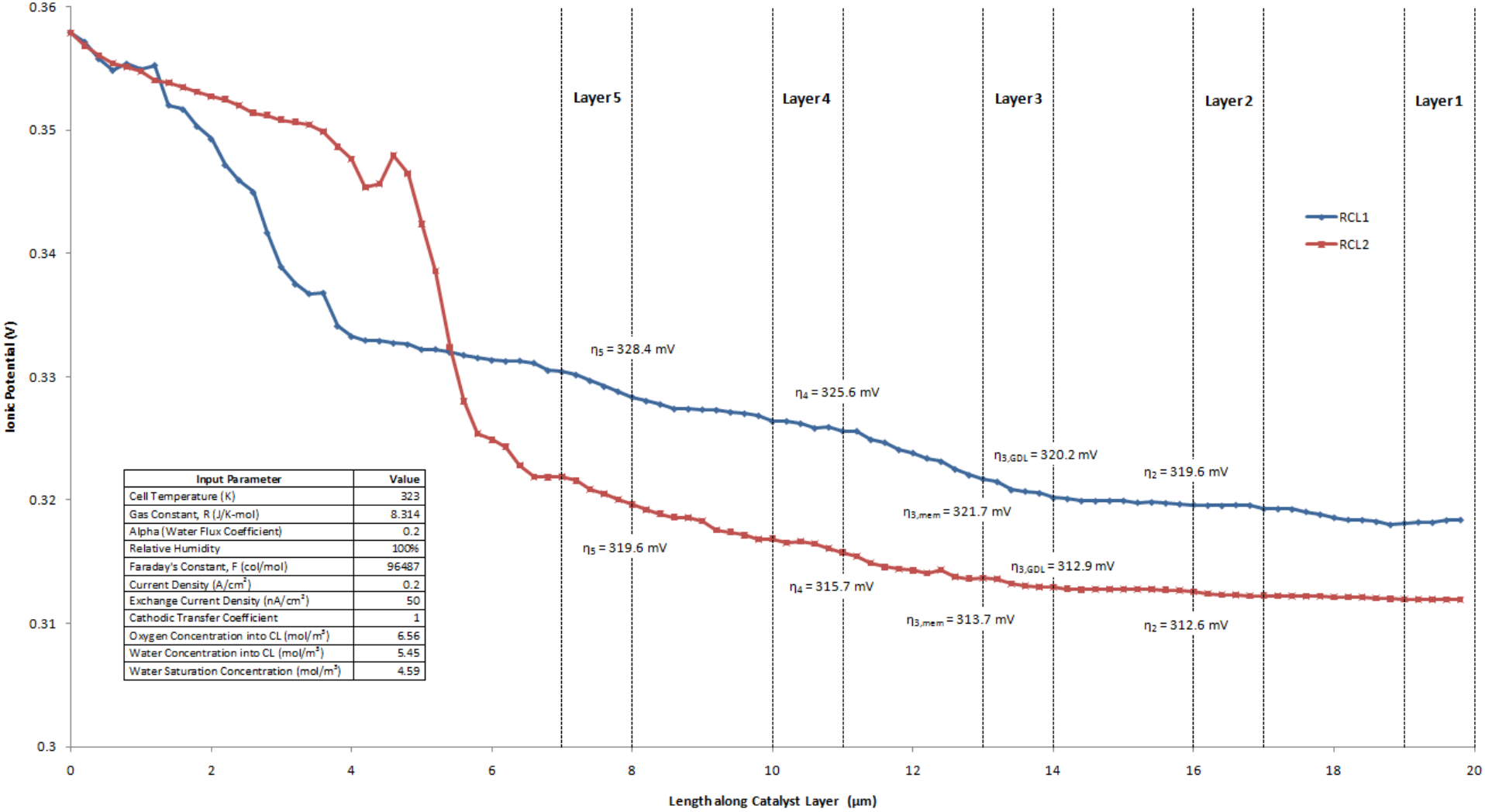

Figure 39. Ionic Potential across the catalyst layer for RCL1 and RCL2 microstructures with indicated DNS input parameters.

4.5 Effects of Operating Conditions and Microstructure on DNS. Case studies were performed in order to examine the effects of different operating input parameters on overall performance and through-plane trends. Comparisons focused on operating temperature, relative humidity, and the microstructure used (see Appendix C for calculating other appropriate input parameters). All experiments were performed with the same cell pressure, GDL properties, and other constant values which can be found in Table 3, Table 4, and Table 5 in Appendix C. Note that these are not the same values used to match the experimental polarization curves in an earlier section and are chosen just to highlight the effects of different operating conditions and microstructure. All plots in sections 4.5.1 and 4.5.2 highlighting the effects of operating temperature and gas channel relative humidity use RCL1 as the microstructure implemented in the DNS.

4.5.1 Operating Temperature. The activity at each location within the catalyst layer is defined as the water vapor concentration at that point divided by the saturation concentration (Eq. (40)), and corresponds to the local relative humidity. Since the saturation concentration at 50 °C is much smaller than that at 90 °C due to smaller saturation pressure, the relative humidity at each location in the microstructure is higher. This higher local relative humidity results in higher water content in the ionomer within the catalyst layer and better ionic conductivity, as per Eq. (38) and Eq. (39). If the model did account for liquid water, there would be more possibility of condensation at 50 °C. The liquid water would block reaction sites and the cell would show overall poorer performance than the 90 °C case, where there is less condensation due to the higher temperature.

Local relative humidity through the catalyst layer at 70% relative humidity in the gas channel and 0.4 A/cm^2 can be seen in

Figure **40**. Note that since the model does not account for liquid water, slight oversaturation is allowed and a relative humidity greater than 100% corresponds to a water vapor pressure that is greater than the saturation pressure. Higher saturation concentration of water vapor also results in lower oxygen concentration into the catalyst layer due to lower partial pressure. This specifically hinders performance at higher current density where there are more mass transport limitations.

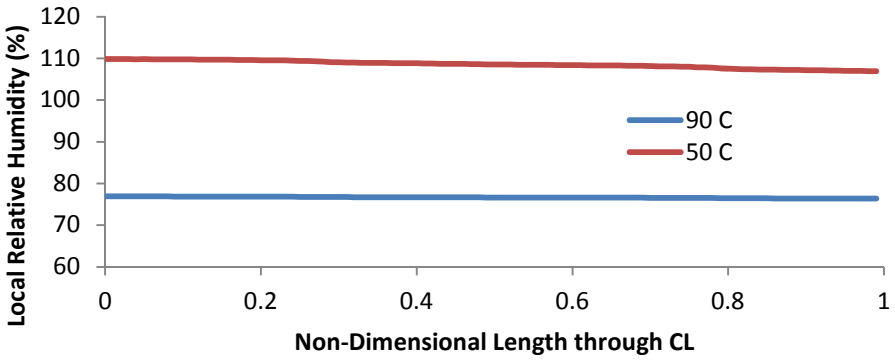

Figure 40. Area averaged local relative humidity through the catalyst layer for 90 °C and 50 °C operating temperatures at 70% relative humidity in the gas channel and a current density of 0.4 A/cm^2.

Figure 41 shows the through-plane ionic potential and Figure 42 and Figure 43 show the 3-D reaction current distributions for 70% relative humidity in the gas channel and a current density of 0.4 A/cm^2. It is important to note that higher temperature operation exhibits higher voltage loss at intermediate current densities (e.g. 0.4 A/cm^2). The combined effects of lower relative humidity (e.g. 70%) and lower temperature (e.g. 50 °C) result in competing influence on the ionic resistance, which causes a pronounced impact on the overpotential at intermediate current density operation [45]. It should, however, also be noted that at elevated temperature, the significant increase in saturation vapor pressure results in lower available oxygen concentration into the catalyst layer, which would have deleterious implications in the higher current density regime where mass transport limitation plays a major role.

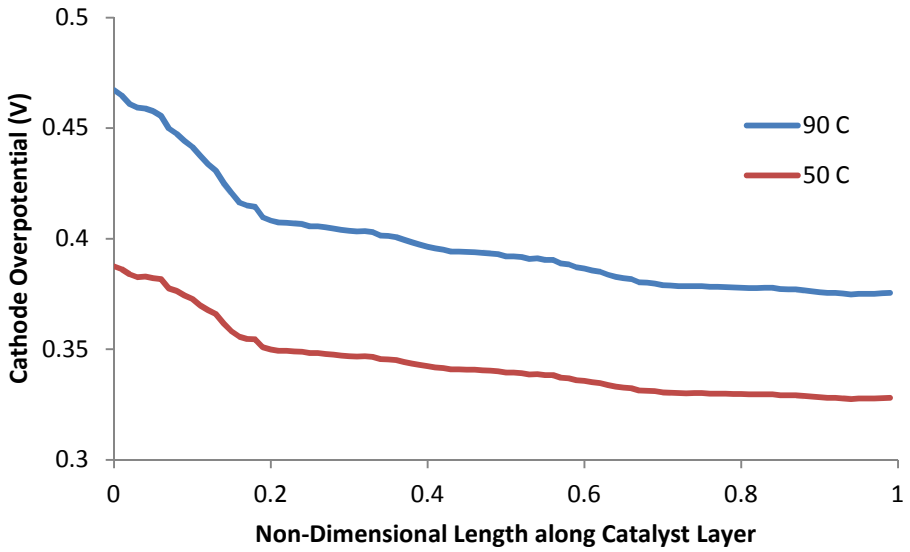

Figure 41. Cathode overpotential through the length of the catalyst layer at 70% relative humidity in the gas channel and 0.4 A/cm^2 current density.

Based on Figure 41, the DNS predicts that 50 °C performs better than 90 °C, which is counter-intuitive. In reality, fuel cell operation at 50 °C would increase the possibility of condensation and pore-clogging liquid water, effecting oxygen diffusion to the reaction site and resulting in overall lower performance, especially at higher current densities. This model, however, assumes that all water produced is in the vapor form, hence there isn't even the possibility of liquid water blocking reaction sites.

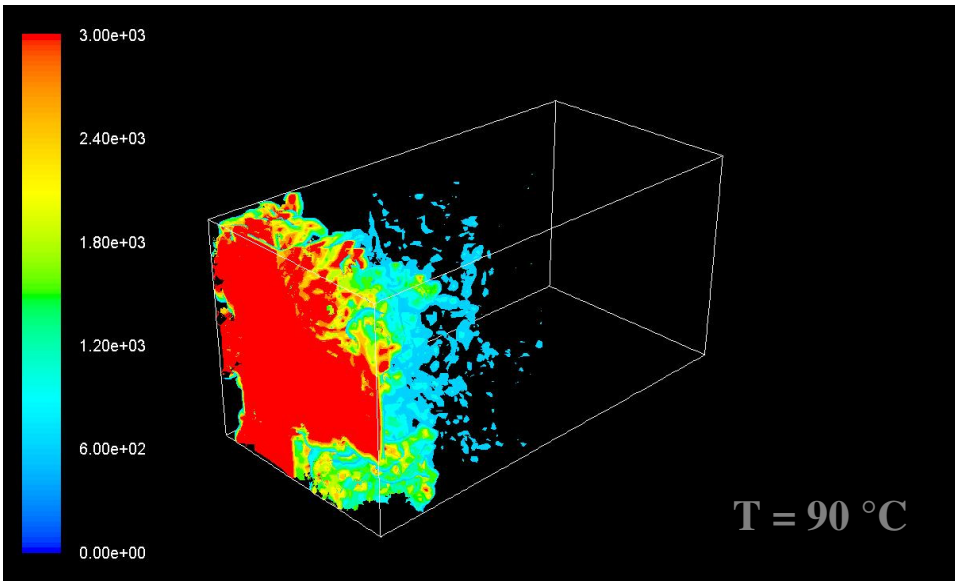

Figure 42. 3-D reaction current distribution at 70% relative humidity in the gas channel, 0.4 A/cm^2, and 90 °C.

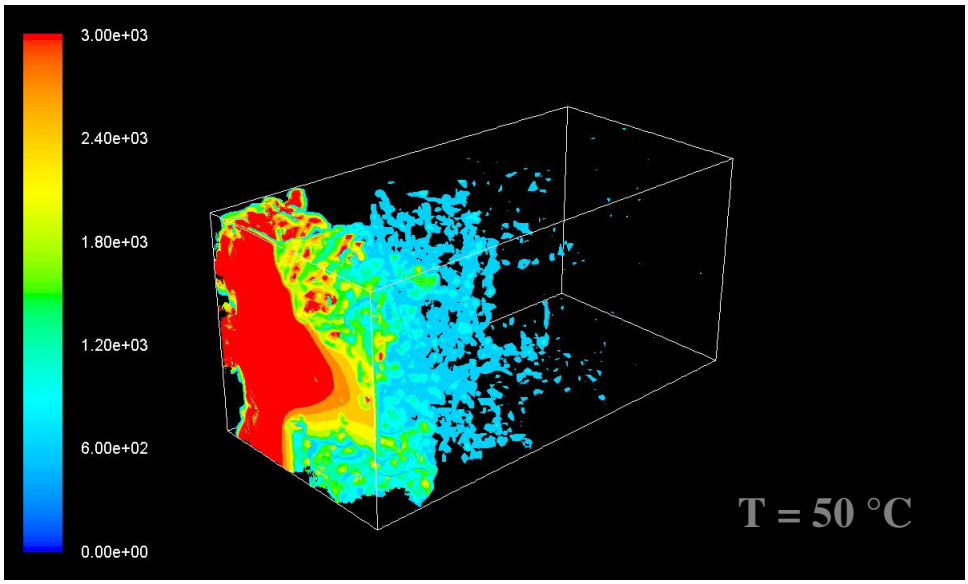

Figure 43. 3-D reaction current distribution at 70% relative humidity in the gas channel, 0.4 A/cm^2, and 50 °C.

Catalyst utilization is a term used to quantify the amount catalyst in the catalyst layer (in this case platinum) that is electrochemically active compared to the total amount of catalyst in the porous structure. Increasing current density causes the abundance of oxygen in the catalyst layer to decrease and therefore effects the catalyst utilization; in other words, catalyst utilization is a function of current density. Figure 44 shows the catalyst utilization at 70% relative humidity and different cell operating temperatures.

There are many definitions for catalyst utilization. In the DNS model, area averaged reaction current is plotted as a function of length through the catalyst layer. A reaction zone percentage can be found by integrating under this curve until the integral is equal to the operating current density. This percentage is then multiplied by the active reaction area percentage. The active reaction area percentage is defined as the interfacial area between transport phases divided by the total interfacial area (~93% for both microstructures).

For example, to find the catalyst utilization at 1 A/cm^2, the area averaged reaction current is summed from the plane adjacent to the membrane to an arbitrary plane until this sum equals 1 A/cm^2. The location of the final plane is divided by the total length of the catalyst layer and the reaction zone percentage is obtained. This value is then multiplied by the active reaction area percentage. While this method is an approximation, it is a useful way to compare catalyst utilization at different operating conditions.

As seen from Figure 44, the catalyst utilization for the 50 °C case is larger at all current densities. This again is attributed to the fact that the 50 °C case has higher relative humidity within the catalyst layer and therefore higher ionic conductivity. In both cases, the catalyst utilization is larger at lower current densities because there is an abundance of oxygen. As the current density increases, the catalyst utilization decreases due to the reduced oxygen concentration.

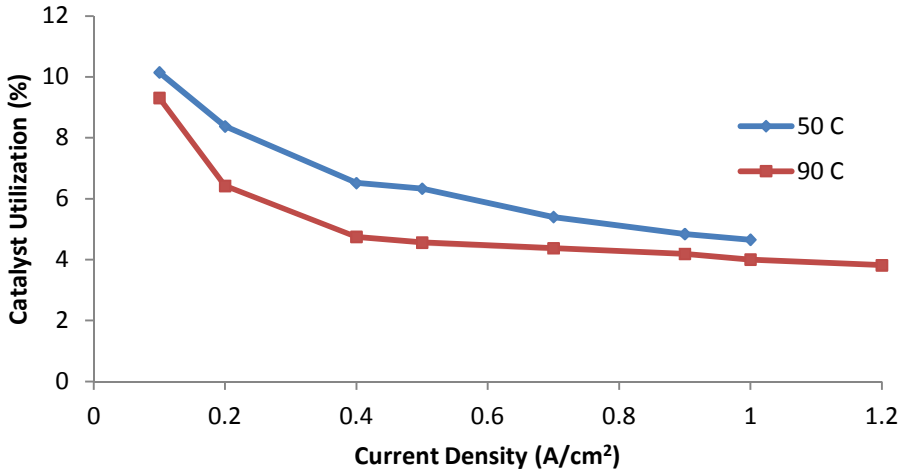

Figure 44. Catalyst utilization as a function of current density at a relative humidity of 70% in the gas channel.

Since the model does not account for liquid water generation, it predicts higher performance at lower temperatures. In reality, lower operating temperature would increase the possibility of pore-blocking liquid water and consequently increase mass transport losses. The effects of pore-blocking liquid water in the GDL can be simulated in the DNS by changing the tortuosity of the GDL, as explained in Section 4.3.2. This would reduce the oxygen concentration into the catalyst layer. The effects of pore-blocking liquid water in the catalyst layer can be simulated in the DNS by

reconstructing a catalyst layer that is less porous, reducing the number of active reaction sites in the numerical domain. This imitates liquid water blocking reaction sites within an actual catalyst layer and increases diffusive losses within the catalyst layer due to the decreased void phase volume fraction. While these adjustments can simulate the effects of liquid water, they are not the proper way to accurately model two-phase catalyst layers.

4.5.2 Gas Channel Relative Humidity. The effects of relative humidity in the gas channel are compared at a current density of 0.4 A/cm^2 and a temperature of 90 °C. Figure 45 and Figure 46 show the 3-D reaction current distributions within the catalyst layer at gas channel relative humidity values of 100% and 70%.

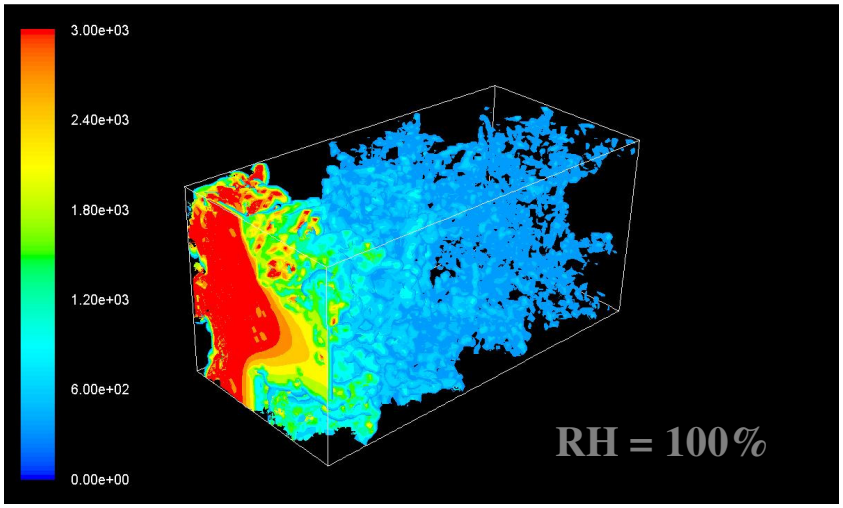

Figure 45. 3-D reaction current distribution at 100% relative humidity in the gas channel, 90 °C, and 0.4 A/cm^2.

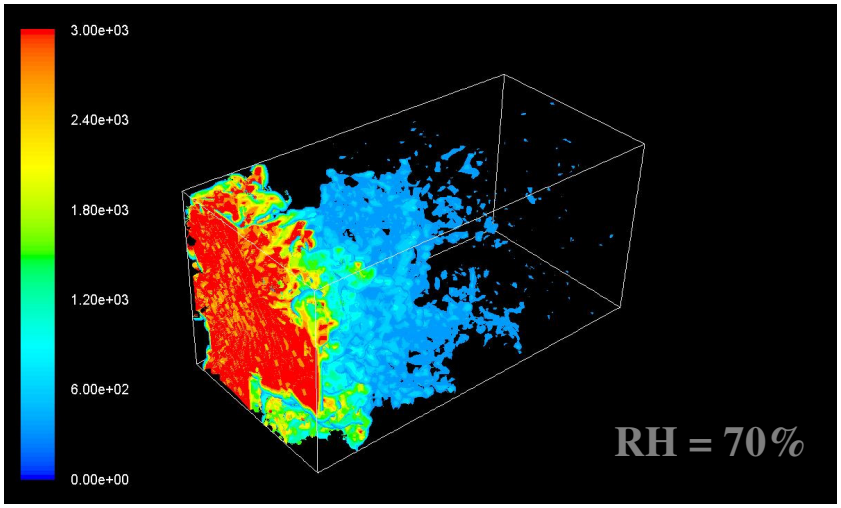

Figure 46. 3-D reaction current distribution at 70% relative humidity in the gas channel, 90 °C, and 0.4 A/cm^2.

As seen from the reaction current distributions, the majority of the electrochemical reaction occurs closer to the membrane at lower relative humidity because lower humidity decreases the ionic conductivity of the catalyst layer. At 100% relative humidity the reaction is spread more uniformly throughout the catalyst layer. This can be seen more clearly in the reaction current density distribution through the catalyst layer in Figure 47 which shows the high humidity case to have slightly but consistently higher current production throughout the catalyst layer.

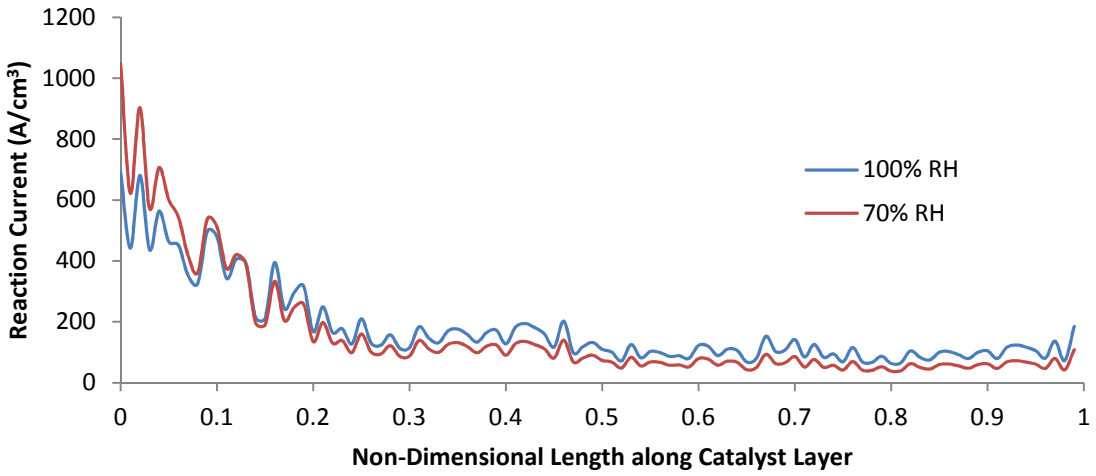

Figure 47. Reaction current through the length of the catalyst layer at 90 °C and 0.4 A/cm^2.

Figure 48 displays a comparison of the catalyst utilization at each relative humidity and a temperature of 90 °C. As expected, the catalyst utilization is higher at higher relative humidity due to increased ionic conductivity within the catalyst layer structure.

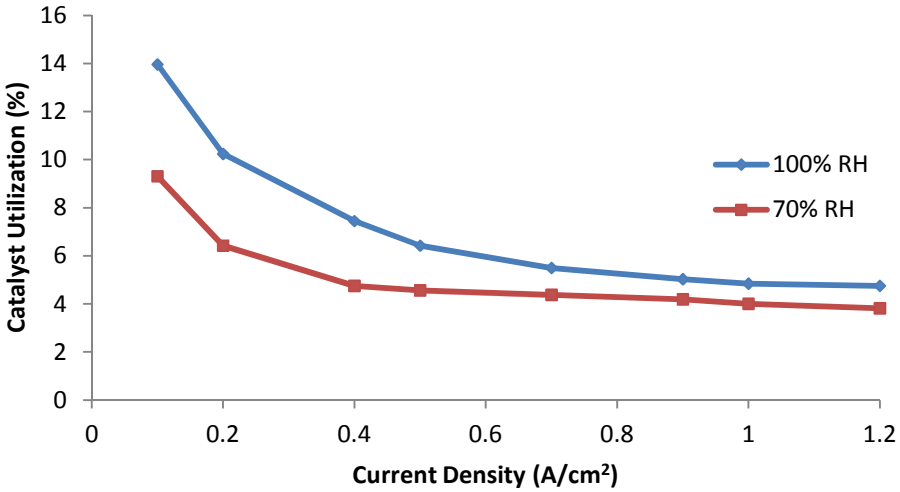

Figure 48. Catalyst utilization at 90 °C and different gas channel relative humidity.

4.5.3 Microstructure Effects. The effects attributable to the different microstructure reconstructions (RCL1 and RCL2) are not apparent in the polarization curves, however, the effects can be seen in reaction current distributions. Pore volume fractions of RCL1 and RCL2 can be seen in Figure 23. As noted earlier, RCL1 exhibits a more uniform porosity, however, it deviates from the average value more than RCL2. While RCL2 has a reduced deviation, it exhibits a region of very low porosity about 5 µm from the gas diffusion layer. The microstructures were created using different stochastic realizations of the initial 3-D random matrix.

Figure 49 and Figure 50 show the 3-D reaction current distributions and Figure 51 shows the area averaged reaction current through the catalyst layer for each microstructure at 90 °C, 0.4 A/cm^2, and 70% relative humidity in the gas channel.

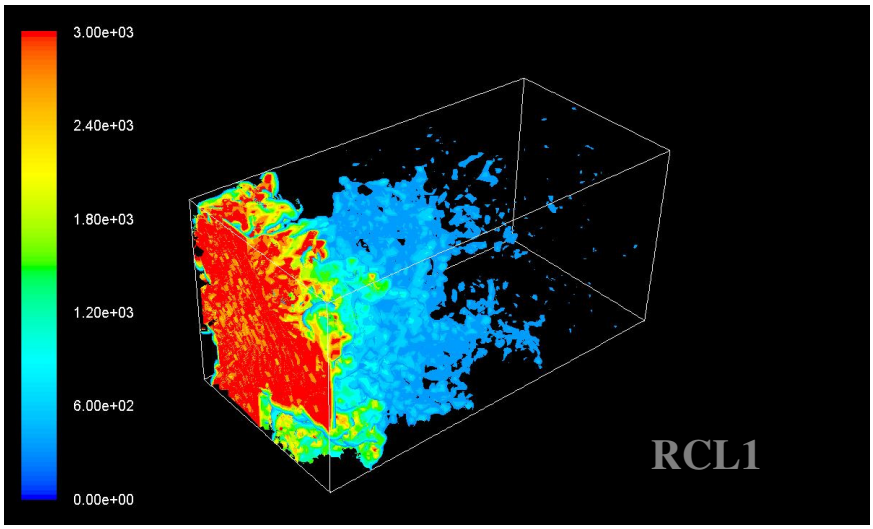

Figure 49. 3-D reaction current distribution for RCL1 at 70% RH, 0.4 A/cm^2, and 90 °C.

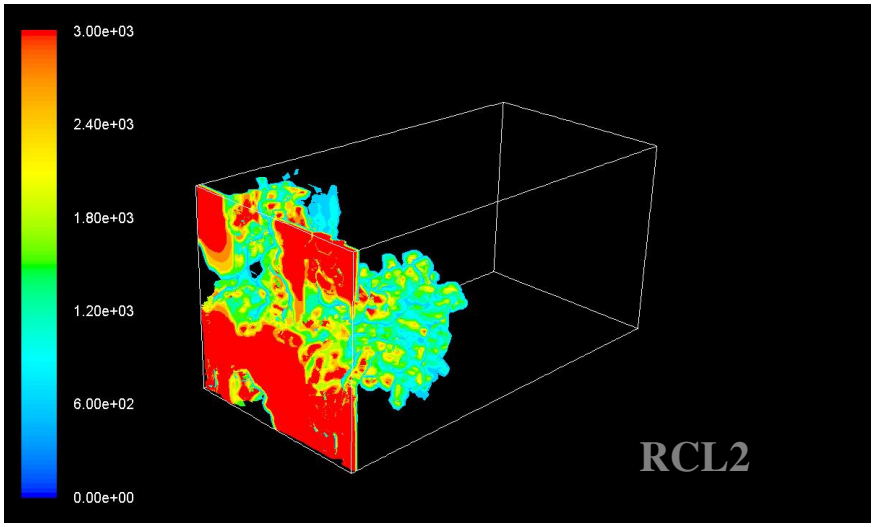

Figure 50. 3-D reaction current distribution for RCL2 at 70% RH, 0.4 A/cm^2, and 90 °C.

As seen from Figure 49 and Figure 50, there is a significant reaction current distribution difference between the two microstructures. RCL1 has a more gradual reduction in the reaction current the further into the catalyst layer. This is due to the fairly uniform porosity throughout the microstructure. RCL2 has a high reaction current near the membrane that decreases very steeply further towards the GDL. Figure 51 uses the reaction current density to illustrate this effect.

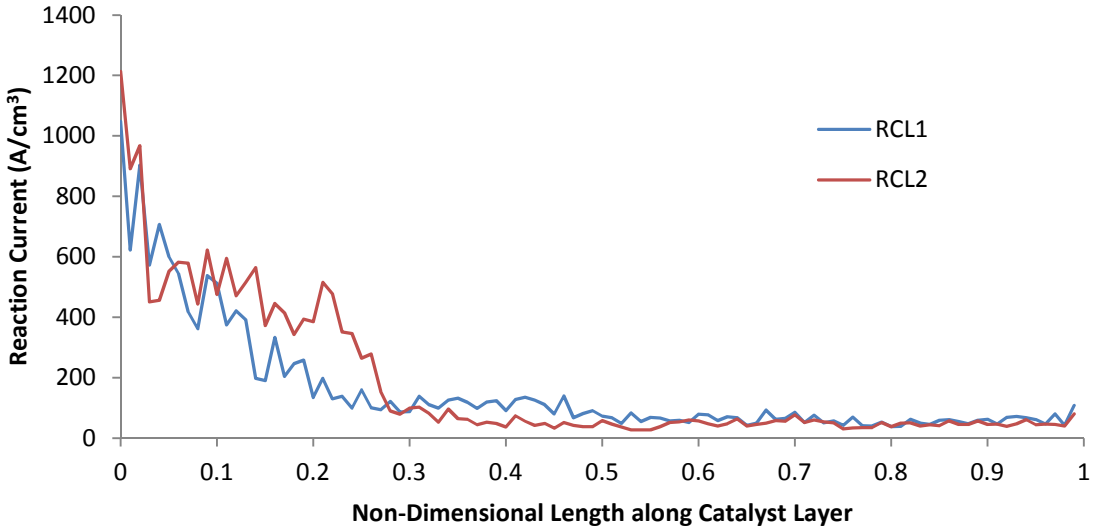

Figure 51. Reaction current through the catalyst layer at 70% relative humidity, 0.4 A/cm^2, and 90 °C.

The high reaction rate near the membrane in RCL2 can be attributed to the large reduction in porosity approximately 15 µm from the membrane as seen in Figure 23. The lack of void phase in this region decreases the number of reaction sites. Therefore, more current must be produced near the membrane to compensate for the ineffectiveness of the low porosity region.

The region of low porosity in RCL2 is especially detrimental at higher current densities. As seen from Figure 52 the catalyst utilization for each microstructure is very similar at lower and intermediate values of current density. At higher current densities when oxygen must diffuse more quickly, the catalyst utilization in RCL2 drops off significantly compared to RCL1. This is because the oxygen has increased difficulty diffusing through the low porosity region toward the membrane where most of the reaction is taking place; the region chokes off oxygen flow to the reaction site.

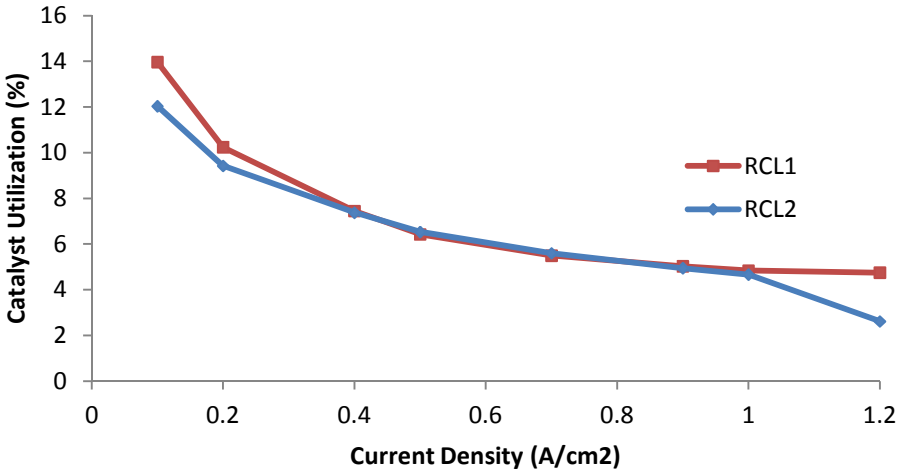

Figure 52. Catalyst utilization for each microstructure at 100% relative humidity and 90 °C.

5. Recommendations and Conclusions

Catalyst layer modeling can be a very useful tool for fuel cell design. If a model can accurately predict the processes occurring within a catalyst layer, different catalyst layer designs, material loadings, physical properties, and even microstructures can be tested before a large amount of money is spent for construction and experimental testing. However, models must be validated through experimental results to confirm that they are capturing the correct physical phenomena. The work presented here has focused on reconciling results from a direct numerical simulation (DNS) of a PEM fuel cell catalyst layer with results obtained from an MES that allows through-thickness measurements of ionic potential. This work has provided insight into useful methods of construction for MES assemblies and into procedures for improving MES and DNS comparative studies.

Ionic potential measurement through the thickness of the catalyst layer proved to be very challenging but was accomplished with one of the MES structures with results similar to expected values from the DNS simulation. Data was successfully collected from one of six MES assemblies constructed and compared to DNS predictions. It was found that the average error between the DNS predicted through-plane measurement and experimental measurements (excluding one outlier) was 26.5% compared to results from RCL1 and 23.7% compared to results from RCL2. The successful DNS used FIB drilling to fabricate the hole for the catalyst layer and used the liquid reference electrode fixture to measure potential. Even for the successful MES, results were noisy and one of the measurement points failed to make connection to the catalyst layer structure. A few design changes are suggested in following sections.

A new technique was used to construct an MES assembly for measurement of ionic potential gradients within the catalyst layer. An MES comprised of two-part sublayers was designed to be much closer to the actual thickness of a catalyst layer (20-25 μm) than in previous work. A reference electrode fixture was also designed that uses sulfuric acid to take the potential measurements at different locations within the catalyst layer.

The Nafion/PVDF sublayers were sequentially cast to achieve an overall thickness of 3-4 μm thus enabling five distinct measurement points within the 20-25 μm thick catalyst layer. The casting method used in this research worked well to create thin ionically conducting/insulating sublayers. However, many of the layers developed discontinuities or did not connect to the catalyst layer. Experimentation with different casting parameters (concentrations, solvents, casting temperature, etc.) may yield more robust sensing layers. Likewise, different materials for the insulating portion of the sublayer could be investigated. In this research, PVDF was chosen due to its insulating properties and to the fact that it can be cast from solution. However, other materials (Kapton, PTFE, etc.) could be explored to see if they could be fabricated in sufficiently thin films and provide a suitable casting surface for the Nafion. The thermal properties of the insulating layer must also be considered, as heat can cause melting, smearing, and shorting when the catalyst layer hole is drilled with FIB or a laser.

Once cast, the sublayers were assembled to overlap only in the region of the catalyst layer to reduce the possibility of shorting with each other and the membrane. The sublayers extended to external

potential sensing ports. The resulting long, thin layers had the disadvantage of being difficult to hydrate and of being susceptible to interruptions that were believed to be caused by discontinuities in the Nafion film or poor attachment at the catalyst layer. Future MES design improvements should focus on reducing the length of the sublayer to improve hydration of the Nafion film and to reduce the possibility of macroscopic defects/discontinuities. This change in geometry will likely require custom machined fuel cell assemblies (which this work attempted to avoid) but should improve the reliability of the ionic potential measurements.

Two methods to taking ionic potential measurements were investigated – a gold wire and a liquid reference electrode fixture – with the latter yielding the most reliable results. The reference electrode fixture eliminates the possibility of unpredictable reactions at the gold/Nafion interface from interfering with the measurements and provides hydration for the sublayer. The reference electrode was designed to rest on top of the fuel cell flow plates with acid and sensing electrodes inserted from overhead. Future designs should consider location of the sensing wells underneath the flow plates so that the wells cannot leak into the fuel cell assembly. In addition, a dedicated sensing well should be provided for the membrane.

The experimental MES technique and the direct numerical simulation model were found to be complementary tools each providing insight to help refine and validate the other, but care must be taken to ensure that the results from the two approaches are mutually relevant. Particular areas of concern include (i) establishment of appropriate operating parameters; (ii) casting procedures; (iii) acquisition of characteristic catalyst layer images.

Operating conditions should be selected to limit the formation of liquid water and to achieve appropriate ionic potential gradients within the catalyst layer. Operating conditions for the MES must be selected such that water generated in the catalyst layer is certain to exit in the vapor phase to make DNS results (which do not account for liquid water in the current model) comparable to experimental results. This means operating at low relative humidity (which may lead to MES dehydration) or operating at high temperatures where additional vapor can be accommodated even at high values of humidity. Operating conditions should also be selected to achieve a large but gradual ionic potential gradient through the catalyst layer to facilitate comparisons between the DNS and experimental results. If the ionic potential is relatively uniform, potential differences between layers are difficult to measure. On the other hand, if the potential gradient is too steep, the entire potential difference may be realized in the first layer of the MES making meaningful comparisons difficult. A useful potential gradient which is significant and which spans much of the catalyst layer can be achieved by operating at intermediate to high values of current density (but not so high as to encounter diffusive losses) and intermediate values of relative humidity to partially hydrate the ionomer (e.g. 75%-90% RH).

Casting procedures for catalyst layers are assumed to yield random structures with generally uniform volumetric properties, including ionomer content, platinum loading, and porosity. It is important that the layer exhibit a uniform porosity through-plane like RCL1 used in this research and avoid large “pockets” of a single phase, as seen in RCL2. However, real catalyst layers exhibit a

through-plane deviation of porosity about an average value. With this being said, it is important that the catalyst layer used in the cathode of the MES be as uniform and statistically homogeneous so the numerical reconstruction is as accurate as possible. This can be difficult due to the size of the cathode catalyst layer (100 µm diameter) but application procedures can help. In this research, the catalyst layer was applied with an airbrush. While this method produces a more uniform coating than painting, there can still be agglomeration, thickness gradients, etc. due to the "human factor". One method to avoid this is with ultrasonic spraying systems. These systems, while expensive, can atomize the catalyst ink and apply a precisely uniform thin film coating. Not only will this help with catalyst layer homogeneity, but because these systems can atomize the catalyst ink, small droplet sizes are guaranteed and agglomerations are eliminated, nearly ensuring that the 100 µm diameter catalyst layer hole is completely and uniformly filled.

Acquisition of characteristic catalyst layer images may entail more complex imaging than that employed in this study if the catalyst layer is not relatively uniform. For example, the MES catalyst layer can be characterized similarly to the FIB/SEM technique explained in Section 2.1.3. While this method is very useful and has been shown to be accurate ([18, 19]), it is a destructive technique; that is that the porous media being reconstructed is coincidently being destroyed. Since fuel cell catalyst layers are typically sprayed, there is the possibility to use this method constructively. Once the hole in the MES is drilled, a portion of the catalyst layer can be sprayed. The MES can then be viewed with an SEM and a picture of the catalyst layer within the hole can be taken. The MES can then be removed from the SEM and the process can be repeated as many times as desired. The resulting images give cross-sectional views of the actual catalyst layer within the MES. These images can then be stochastically combined to interpolate the structure between pictures. While this reconstruction method is time consuming (pumping down SEM, spraying many times, etc.), it theoretically reconstructs the actual catalyst layer being used in the MES and may even be the most accurate.

The previously suggested reconstruction method uses several different SEM images to reconstruct the porous catalyst layer. Traditionally, only one SEM picture is taken of the XY plane of the catalyst layer (looking down from the top of the catalyst layer) and a two-point autocorrelation is then generated from this picture. An alternate method could use two or three pictures of the catalyst layer; an XY picture, a YZ picture, and/or an XZ picture. The YZ and XZ pictures are cross-sectional pictures of the catalyst layer. Additional autocorrelation functions can be generated from these alternate views and used in the reconstruction for each respective plane.

Assumptions utilized in the reconstruction of the catalyst layer were shown to yield different stochastic microstructures that had different current distributions even though overall polarization curve behavior was comparable. The DNS uses a reconstructed catalyst layer and solves conservation equations at each location within the domain. The catalyst layer is reconstructed stochastically using an SEM image. Two different catalyst layer microstructures were reconstructed for this research, each using a different stochastic realization based on the same initial images. The microstructures proved to be quite different; RCL1 exhibited uniform through-plane porosity about an average porosity but with a fairly large deviation. RCL2 exhibited less deviation about an average value but had a region of very

low porosity which choked a large part of the catalyst layer in some cases. Improved catalyst layer reconstruction methods such as multiple plane autocorrelation functions and constructive catalyst layer characterization could help to reduce the uncertainty in the reconstruction.

The effects of different microstructures could not be seen in polarization curves, however, the effects could be seen in 3-D reaction current plots. RCL1 showed a more uniform reaction current distribution while RCL2 showed higher reaction current occurring near the membrane and a large decrease closer to the GDL. This can be attributed to the large decrease in porosity in RCL2. It was found that the large drop-off in the porosity in RCL2 is particularly detrimental to catalyst utilization at higher current densities because the oxygen is choked off from a large part of the catalyst layer.

Results from reconciling the DNS and the experimental results suggest that the conductance of the ionic pathway within the catalyst layer is particularly important to cell performance. Polarization curves of the MES exhibited larger Ohmic type losses than initially predicted by the DNS. Several modifications to the DNS were explored to reconcile the model and experiment. Results suggest that the lower performance of the actual cell relative to the model was attributable to the low conductance of the thin, tortuous ionomeric pathway. By increasing the significance of the Bruggeman correction for transport within the mixed ionomer/carbon voxel, the model results were brought into agreement with the experimental results.

This work was among the first studies to compare experimental through-plane ionic potential measurements to DNS modeling of a cathode catalyst layer in a PEM fuel cell. It was found that the combination of the two techniques provides complementary insights. Particular challenges were found in the fabrication of robust microscale films for sensing, in the fabrication and numerical reconstruction of representative catalyst layers, and in the selection of operating conditions to yield results that were amenable to both numerical and experimental analysis. Improvements in experimental methods, microstructure generation, and DNS modeling can help to yield better numerical and experimental agreement and to improve the understanding of catalyst layer behavior.

References

1. White, F.M., *Viscous Fluid Flow*. McGraw-Hill Series in Mechanical Engineering. 1991, New York: McGraw-Hill.
2. Mukherjee, P. and C.Y. Wang, *Stochastic Microstructure Reconstruction and Direct Numerical Simulation of the PEFC Catalyst Layer.* Journal of the Electrochemical Society, 2006. 153(5): p. A840.
3. Hess, K.C., S. Litster, and W.K. Epting, *In Situ Measurements of Through-Plane, Ionic Potential Distributions in Porous Electrodes*, in *ASME 2010 Eighth International Fuel Cell Science, Engineering, and Technology Conference*. 2010.
4. Kong, C.S., et al., *Influence of Pore-Size Distribution of Diffusion Layer on Mass Transport Problems of Proton Exchange Membrane Fuel Cells.* Journal of Power Sources, 2002. 108(1-2): p. 185-191.
5. Androutsopoulos, G.P. and R. Mann, *Evaluation of Mercury Porosimeter Experiments Using a Network Pore Structure Model.* Chemical Engineering Science, 1979. 34(10): p. 1203-1212.
6. Landis, E.N., E.N. Nagy, and D.T. Keane, *Microstructure and Fracture in Three Dimensions.* Engineering Fracture Mechanics, 2003. 70(7-8): p. 911-925.
7. Trtik, P., et al., *3D Imaging of Microstructure of Spruce Wood.* Journal of Structural Biology, 2007. 159(1): p. 46-55.
8. Griesser, S., et al., *Characterization of Fuel Cells and Fuel Cell Systems Using Three-Dimensional X-Ray Tomography.* Journal of Fuel Cell Science and Technology, 2007. 4(1): p. 84.
9. Izzo, J.R., et al., *Nondestructive Reconstruction and Analysis of SOFC Anodes Using X-ray Computed Tomography at Sub-50nm Resolution.* Journal of the Electrochemical Society, 2008. 155(5): p. B504.
10. Pfrang, A., et al., *Imaging of Membrane Electrode Assemblies of Proton Exchange Membrane Fuel Cells by X-ray Computed Tomography.* Journal of Power Sources, 2011. 196: p. 5272-5276.
11. Quiblier, J.A., *A New Three-Dimensional Modeling Technique for Studying Porous Media.* Journal of Colloid and Interface Science, 1984. 98(1): p. 84-102.
12. Bentz, D.P. and N.S. Martys, *Hydraulic Radius and Transport in Reconstructed Model Three-Dimensional Porous Media.* Transport in Porous Media, 1994. 17: p. 221-238.
13. Liang, Z.R., et al., *A Reconstruction Technique for 3-D Porous Media Using Image Analysis and Fourier Transforms.* Journal of Petroleum Science and Engineering, 1998. 21: p. 273-283.
14. Okabe, H. and M. Blunt, *Pore Space Reconstruction Using Multiple-Point Statistics.* Journal of Petroleum Science and Engineering, 2005. 46(1-2): p. 121-137.
15. Yeong, C.L.Y. and S. Torquato, *Reconstructing Random Media.* Physical Review E, 1998. 57(1): p. 495-506.
16. Yeong, C.L.Y. and S. Torquato, *Reconstructing Random Media. II. Three-Dimensional Media from Two-Dimensiomal Cuts.* Physical Review E, 1998. 58(1): p. 224-233.

17. Kim, S.H. and H. Pitsch, *Reconstruction and Effective Transport Properties of the Catalyst Layer in PEM Fuel Cells.* Journal of the Electrochemical Society, 2009. 156(6): p. B673.

18. Bansal, R.K., et al., *High-Resolution Three-Dimensional Reconstruction: A Combined Scanning Electron Microscope and Focused Ion Beam Approach.* Journal of Vacuum Science Technology, 2006. 24(2): p. 554-561.

19. Wilson, J.R., et al., *Three-Dimensional Reconstruction of a Solid-Oxide Fuel-Cell Anode.* Nature Materials, 2006. 5(7): p. 541-544.

20. Patelli, E. and G. Schuëller, *On Optimization Techniques to Reconstruct Microstructures of Random Heterogeneous Media.* Computational Materials Science, 2009. 45(2): p. 536-549.

21. Kasula, B.V., et al., *3D Microstructure Reconstructions of Solid Oxide and Proton Exchange Membrane Fuel Cell Electrodes with Applications to Numerical Simulations of Reacting Mixture Flows Using LBM*, in *ASME International Mechanical Engineering Congress and Exposition*. 2007: Seattle, WA.

22. Wang, G., P. Mukherjee, and C.Y. Wang, *Direct Numerical Simulation (DNS) Modeling of PEFC Electrodes Part I. Regular Microstructure.* Electrochimica Acta, 2006. 51(15): p. 3139-3150.

23. Wang, G., P. Mukherjee, and C.Y. Wang, *Direct Numerical Simulation (DNS) Modeling of PEFC Electrodes Part II. Random Microstructure.* Electrochimica Acta, 2006. 51(15): p. 3151-3160.

24. Alder, P.M., *Porous Media: Geomoetry and Transports*. 1992, Stoneham, MA: Butterworth-Heinemann.

25. Berryman, J.G., *Measurement of Spatial Correlation Functions Using Image Processing Techniques.* Journal of Applied Physics, 1985. 57(7): p. 2374-2384.

26. Cressie, N., *Statistics for Spatial Data*. 1993, New York: J. Wiley.

27. O'Hayre, R., et al., *Fuel Cell Fundamentals*. 2nd ed. 2009, New York: John Wiley & Sons.

28. Springer, T.E., T.A. Zawodzinski, and S. Gottesfeld, *Polymer Electrolyte Fuel Cell Model.* Journal of the Electrochemical Society, 1991. 138(8): p. 2334-2342.

29. Bernardi, D.M. and M.W. Verbrugge, *A Mathematical Model of the Solid-Polymer-Electrolyte Fuel Cell.* Journal of the Electrochemical Society, 1992. 139(9): p. 2477-2491.

30. Khajeh-Hosseini-Dalasm, N., K. Fushinobu, and K. Okazaki, *Three-Dimensional Transient Two-Phase Study of the Cathode Side of a PEM Fuel Cell.* International Journal of Hydrogen Energy, 2010. 35(9): p. 4234-4246.

31. Hu, M., *Three Dimensional, Two Phase Flow Mathematical Model for PEM Fuel Cell: Part I. Model Development.* Energy Conversion and Management, 2004. 45(11-12): p. 1861-1882.

32. Broka, K. and P. Ekdunge, *Modeling the PEM Fuel Cell Cathode.* Journal of Applied Electrochemistry, 1997. 27: p. 281-289.

33. Berg, P., A. Novruzi, and K. Promislow, *Analysis of a Cathode Catalyst Layer Model for a Polymer Electrolyte Fuel Cell.* Chemical Engineering Science, 2006. 61(13): p. 4316-4331.

34. Genevey, D.B., *Transient Model of Heat, Mass, and Charge Transfer as well as Electrochemistry in the Cathode Catalyst Layer of a PEMFC*, in *Mechanical Engineering*. 2001, Virginia Tech: Blacksburg.

35. Eikerling, M. and A.A. Kornyshev, *Modeling the Performance of the Cathode Catalyst Layer of Polymer Electrolyte Fuel Cells.* Journal of Electroanalytical Chemistry, 1998. 453: p. 89-106.

36. Song, D., *Numerical Optimization Study of the Catalyst Layer of PEM Fuel Cell Cathode.* Journal of Power Sources, 2004. 126(1-2): p. 104-111.

37. Kamarajugadda, S. and S. Mazumder, *Numerical Investigation of the Effect of Cathode Catalyst Layer Structure and Composition on Polymer Electrolyte Membrane Fuel Cell Performance.* Journal of Power Sources, 2008. 183(2): p. 629-642.

38. Wang, Q., et al., *Structure and Performance of Different Types of Agglomerates in Cathode Catalyst Layers of PEM Fuel Cells.* Journal of Electroanalytical Chemistry, 2004. 573(1): p. 61-69.

39. Schwarz, D. and N. Djilali, *3D Modeling of Catalyst Layers in PEM Fuel Cells.* Journal of the Electrochemical Society, 2007. 154(11): p. B1167.

40. Liu, J. and M. Eikerling, *Model of Cathode Catalyst Layers for Polymer Electrolyte Fuel Cells: The Role of Porous Structure and Water Accumulation.* Electrochimica Acta, 2008. 53(13): p. 4435-4446.

41. Schwarz, D.H. and N. Djilali, *Three-Dimensional Modelling of Catalyst Layers in PEM Fuel Cells: Effects of Non-Uniform Catalyst Loading.* International Journal of Energy Research, 2009. 33(7): p. 631-644.

42. Srinivasarao, M., et al., *Performance Analysis of a PEM Fuel Cell Cathode with Multiple Catalyst Layers.* International Journal of Hydrogen Energy, 2010. 35(12): p. 6356-6365.

43. Siegel, N.P., et al., *Single Domain PEMFC Model Based on Agglomerate Catalyst Geometry.* Journal of Power Sources, 2003. 115(1): p. 81-89.

44. Coppo, M., N.P. Siegel, and M.R. Von Spakovsky, *On the Influence of Temperature on PEM Fuel Cell Operation.* Journal of Power Sources, 2006. 159: p. 560-569.

45. Mukherjee, P. and C.Y. Wang, *Direct Numerical Simulation Modeling of Bilayer Cathode Catalyst Layers in Polymer Electrolyte Fuel Cells.* Journal of the Electrochemical Society, 2007. 154(11): p. B1121.

46. Bird, R., W. Stewart, and E. Lightfoot, *Transport Phenomena*. 2002, New York: John Wiley and Sons.

Appendix A: Oxygen and Water Concentrations at $x = x_L$

For ease of implementation of the boundary conditions, at the interface between the catalyst layer and the membrane, one layer of electrolyte cells is added to the computational domain and the operating current is applied uniformly on this layer (see Eq. (26)). At the interface between the catalyst layer and the gas diffusion layer, one layer of pore cells is added to the computational domain and a constant oxygen and water vapor concentration are implemented (see Eq. (28)). The oxygen concentration at this interface ($x = x_L$, see Figure 5) is adjusted to take into account the diffusion resistance through the gas diffusion layer with constant oxygen concentration in the gas channel and is defined in Eq. (31) (linear oxygen concentration profile within the GDL)

$$c_{O_2,x_L} = c_{O_2,inlet} - \frac{I\Delta X_{GDL}}{4FD^{g,eff}_{O_2,GDL}} \tag{31}$$

where $c_{O_2,inlet}$ is the concentration of oxygen into the gas diffusion layer, ΔX_{GDL} is the gas diffusion layer thickness, and $D^{g,eff}_{O_2,GDL}$ is the effective diffusion coefficient of oxygen in air adjusted with respect to the GDL porosity, ε_{GDL}, and tortuosity, τ_{GDL}, and is given by Eq. (32)[2]

$$D^{g,eff}_{O_2,GDL} = D^{g}_{O_2}\frac{\varepsilon_{GDL}}{\tau_{GDL}} \tag{32}$$

Similar to the oxygen concentration, the water vapor concentration profile is assumed constant in the gas channel and linear within the GDL. The concentration of water vapor at the interface between the catalyst layer and the GDL ($x = x_L$) is defined with Eq. (33)

$$c_{H_2O,x_L} = c_{H_2O,inlet} + N_w\frac{\Delta X_{GDL}}{D^{g,eff}_{H_2O,GDL}} \tag{33}$$

where $c_{H_2O,inlet}$ is the water vapor concentration of the humidified air at the channel inlet, N_w is the water flux through the GDL, and $D^{g,eff}_{H_2O,GDL}$ is the effective diffusion coefficient of water vapor in air. $c_{H_2O,inlet}$ is calculated from the relative humidity and saturation concentration at the cell operating temperature. The effective diffusion coefficient of water is adjusted with respect to GDL porosity and tortuosity similar to the effective oxygen diffusion coefficient given by Eq. (32). The net water flux through the GDL is the sum of the net flux across the membrane and the water production rate in the catalyst layer and is given by Eq. (34)

$$N_w = (\alpha + 0.5)\frac{I}{F} \tag{34}$$

The oxygen and water concentrations defined above are inputs to the direct numerical simulation. These values must be calculated and manually entered into the program, hence the detailed description.

Appendix B: Species Diffusivity and Ionic Conductivity

For pore level DNS modeling in the catalyst layer microstructure, Knudsen diffusion due to molecule to wall collision becomes important. Therefore, $D_{O_2}^g$ is a combination of Knudsen and binary diffusivity of oxygen through a gas. This is also important for the diffusion of water vapor, and the combined diffusivity of species *i* through a gas, D_i^g, is given by Eq. (35)

$$D_i^g = \left(\frac{1}{D_{b,i}^g} + \frac{1}{D_{K,i}^g}\right)^{-1} \tag{35}$$

where $D_{b,i}^g$ is the binary diffusivity of species *i* in the gas and $D_{K,i}^g$ is the Knudsen diffusivity of species *i* in the gas. $D_{b,i}^g$ and $D_{K,i}^g$ are given in Eq. (36)[46] and Eq. (37)

$$D_{b,i}^g = \frac{a}{p}\left(\frac{T}{\sqrt{T_{ci}T_{cg}}}\right)^b \left(p_{ci}p_{cg}\right)^{1/3}\left(T_{ci}T_{cg}\right)^{5/12}\left(\frac{1}{M_i} + \frac{1}{M_g}\right)^{1/2} \tag{36}$$

$$D_{K,i}^g = \frac{2}{3}\left(\frac{8RT}{\pi M_i}\right)^{1/2} r_p \tag{37}$$

where a = 2.745e-4 and b = 1.823 for pairs of non-polar gases or a = 3.640e-4 and b = 2.334 for pairs involving water (polar) and a non-polar gas, p is the cell operating pressure, T is the cell operating temperature, T_{ci}, p_{ci}, and M_i are the critical temperature, critical pressure, and molecular weight of species *i* (oxygen or water), T_{cg}, p_{cg}, and M_g are the critical temperature, critical pressure, and molecular weight of the gas in which these species are diffusing (in this case air), and r_p is the representative mean pore radius (50 nm).

The ionic conductivity, κ_o, of the electrolyte phase of the reconstructed microstructure as a function of water content has been correlated by Springer et al. [28], and is shown in Eq. (38)

$$\kappa_o(\lambda) = 100 \exp\left[1268\left(\frac{1}{303} - \frac{1}{T}\right)\right](0.005139\lambda - 0.00326) \tag{38}$$

where λ is the water content, and depends on the water activity, a, in the gas phase according to the experimental fit shown in Eq. (39)

$$\lambda = \begin{cases} 0.043 + 17.81a - 39.85a^2 + 36.0a^3, & 0 < a \leq 1 \\ 14 + 1.4(a-1), & 1 < a \leq 3 \end{cases} \tag{39}$$

The water activity, *a,* is defined in Eq. (40)

$$a = \frac{c_{H_2O}}{c_{H_2O}^{sat}} \tag{40}$$

where $c_{H_2O}^{sat}$ is the saturated water concentration and c_{H_2O} is the local water concentration. Substituting Eq. (39) into Eq. (38) provides the ionic conductivity as a function of water activity. Since the

concentration of water varies at every point within the catalyst layer, the ionic conductivity will also vary and must be calculated at each location.

Appendix C: DNS Inputs

Table 3 shows typical operating parameters that must be input into the user-defined function (UDF) for the DNS to work properly. Note that the variable symbol indicated is the variable symbol used in this document, not necessarily the variable symbol used in the UDF. Grey boxes in the following tables indicate an input value into the UDF and the ones used throughout the case study (see Section 4).

Table 3. User-defined parameters that must be input into the UDF.

Variable	Description	Typical Value
Cell Temperature (K)	T	323
Gas Constant (J/K-mol)	R	8.314
Net Water Flux Coefficient	α	0.2
Relative Humidity	RH	1
Faraday's Constant (col/mol)	F	96487
Current Density (A/m^2)	j	3000
Exchange Current Density (A/m^2)	j_o	5.00E-04
Cathodic Transfer Coefficient	α_c	1

Table 4 shows typical geometrical parameters input into the UDF. These parameters are constrained by the dimensions of the reconstructed microstructure. A rectangular geometry and mesh must be generated in Fluent which matches the overall geometrical properties of the reconstructed microstructure.

Table 4. Geometrical inputs to the UDF. Inputs are constrained by the size of the reconstructed microstructure.

Variable	Description	Typical Value
Domain Length (m)	x_L, length of the domain without the single ionomer/gas phase layers at each boundary	2.00E-05
Cell Dimension (m)	Δx, dimension of one side of the cubic cells	2.00E-07
Number of Cells in x Direction		102
Number of Cells in y-z Plane		2500
Cell Center to Center Distance (m)	Distance from center to center of adjacent cells	2.00E-07

The preceding inputs to the UDF are all independent of one another, however, there are some parameters that must be calculated before they can be input into the UDF. In order to calculate these parameters, there is some other information that needs to be used or calculated. Table 5 shows the supplementary variables and calculations that are needed to calculate the UDF inputs shown in Table 6.

Table 5. Supplementary information that is required and/or needs to be calculated to find the UDF input parameters shown in Table 6.

Variable	Description	Typical Value
Cell Pressure (atm)	p	1
GDL Thickness (μm)	ΔX_{GDL}	290
GDL Porosity	ε_{GDL}	0.6
GDL Tortuosity	τ_{GDL}	1.5
Saturation Pressure (Pa)	$P_{sat}(T)$, can be found in thermodynamic water tables	12350
O_2 Binary Diffusion Coefficient	Binary o_2 diffusivity in air calculated based on kinetic theory of gases using critical temperatures and pressures (Eq. 36)	2.38E-05
O_2 Knudsen Diffusion Coefficient	Knudsen diffusion coefficient of O_2 (Eq. 37)	1.54E-05
H_2O Binary Diffusion Coefficient	Binary H_2O diffusivity in air calculated based on kinetic theory of gases using critical temperatures and pressures (Eq. 36)	3.13E-05
H_2O Knudsen Diffusion Coefficient	Knudsen diffusion coefficient of H_2O (Eqn. 37)	2.05E-05
Effective O_2 Diffusivity in GDL	Used to find oxygen boundary condition (Eq. 32)	3.74E-06
Effective H_2O Diffusivity in GDL	Used to find water boundary condition (Eq. 32)	4.96E-06
Inlet O_2 Concentration (mol/m^3)	Concentration of oxygen into the GDL based on operating conditions and relative humidity	6.96
Inlet H_2O Concentration (mol/m^3)	Concentration of water into the GDL based on operating conditions and relative humidity	4.60

Table 6. Variables that must be calculated before entered into the UDF.

Variable	Description	Typical Value
Reference Concentration (mol/m^3)	Molar concentration of the reactant at the channel inlet ($C_{ref} = P/RT$)	37.73
O_2 Reference Concentration (mol/m^3)	Reference O_2 molar concentration used in Butler-Volmer equation ($C_{ref,O2} = P°/RT°$)	40.90
Saturated H_2O Concentration (mol/m^3)	Saturation concentration of water based on cell temperature ($C_{sat} = P_{sat}(T)/RT$)	6.59
Total O_2 Diffusion Coefficient	Combined O_2 diffusivity (Eq. 35)	9.36E-06
Total H_2O Diffusion Coefficient	Combined H_2O diffusivity, (Eq. 35)	12.40E-06
O_2 Boundary Condition into CL	Concentration of O_2 into the catalyst layer (Eq. 31)	6.36
H_2O Boundary Condition into CL	Concentration of H_2O into the catalyst layer (Eq. 33)	5.87

Appendix D: Reference Electrode Fixture Design

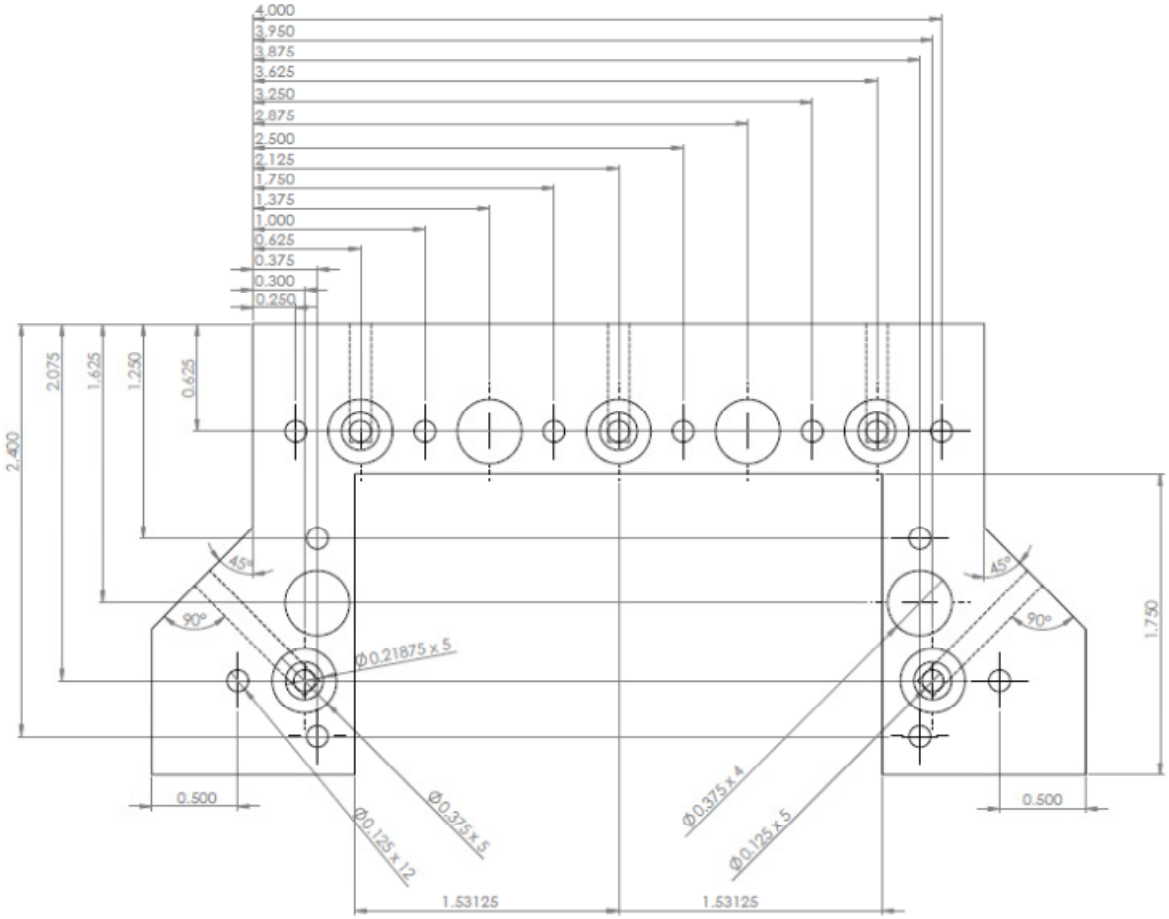

Figure 53. Front view of part 1 of the reference electrode fixture. Dimensions are in inches.

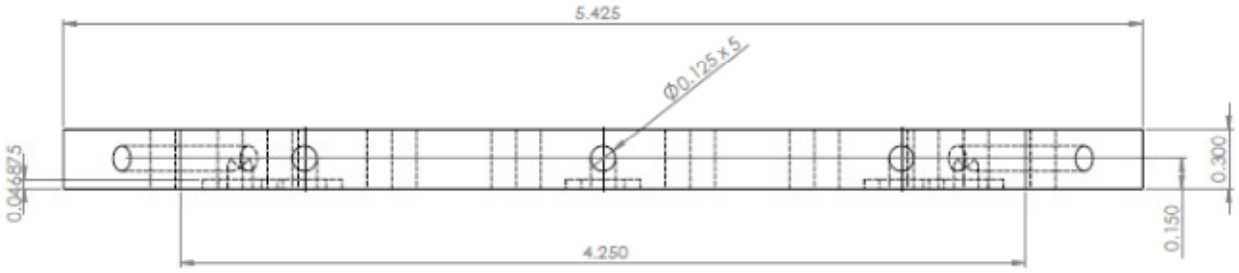

Figure 54. Top view of part 1 of the reference electrode fixture. Dimensions are in inches.

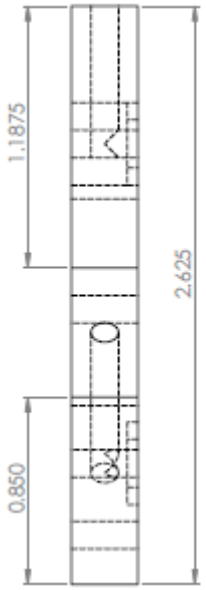

Figure 55. Side view of part 1 of the reference electrode fixture. Dimensions are in inches.

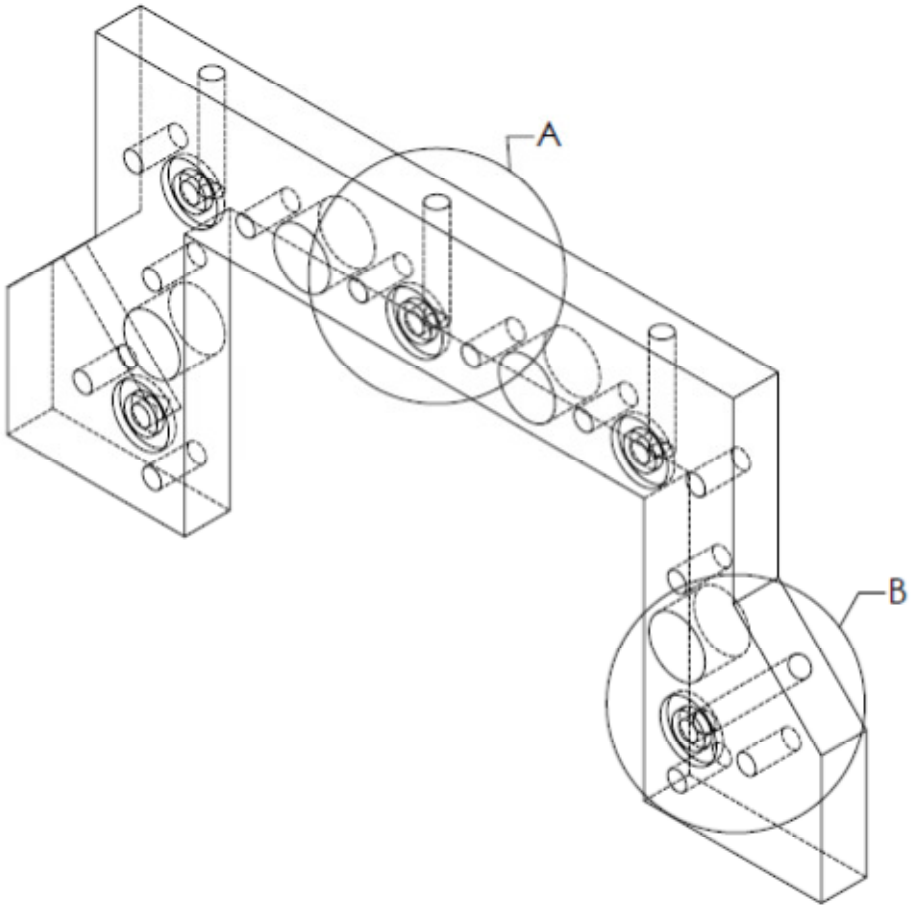

Figure 56. Isometric view of part 1 of the reference electrode fixture.

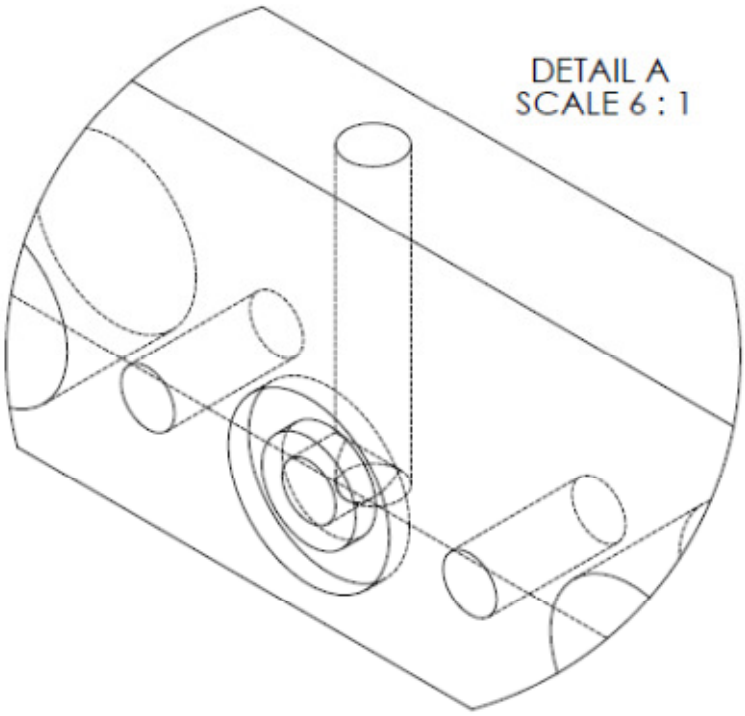

Figure 57. Detailed view of Section A from Figure 56.

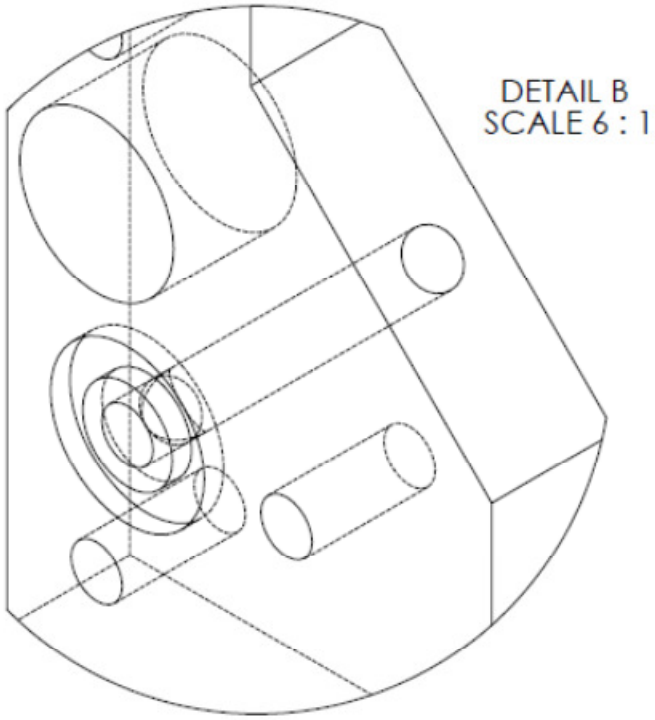

Figure 58. Detailed view of Section B from Figure 56.

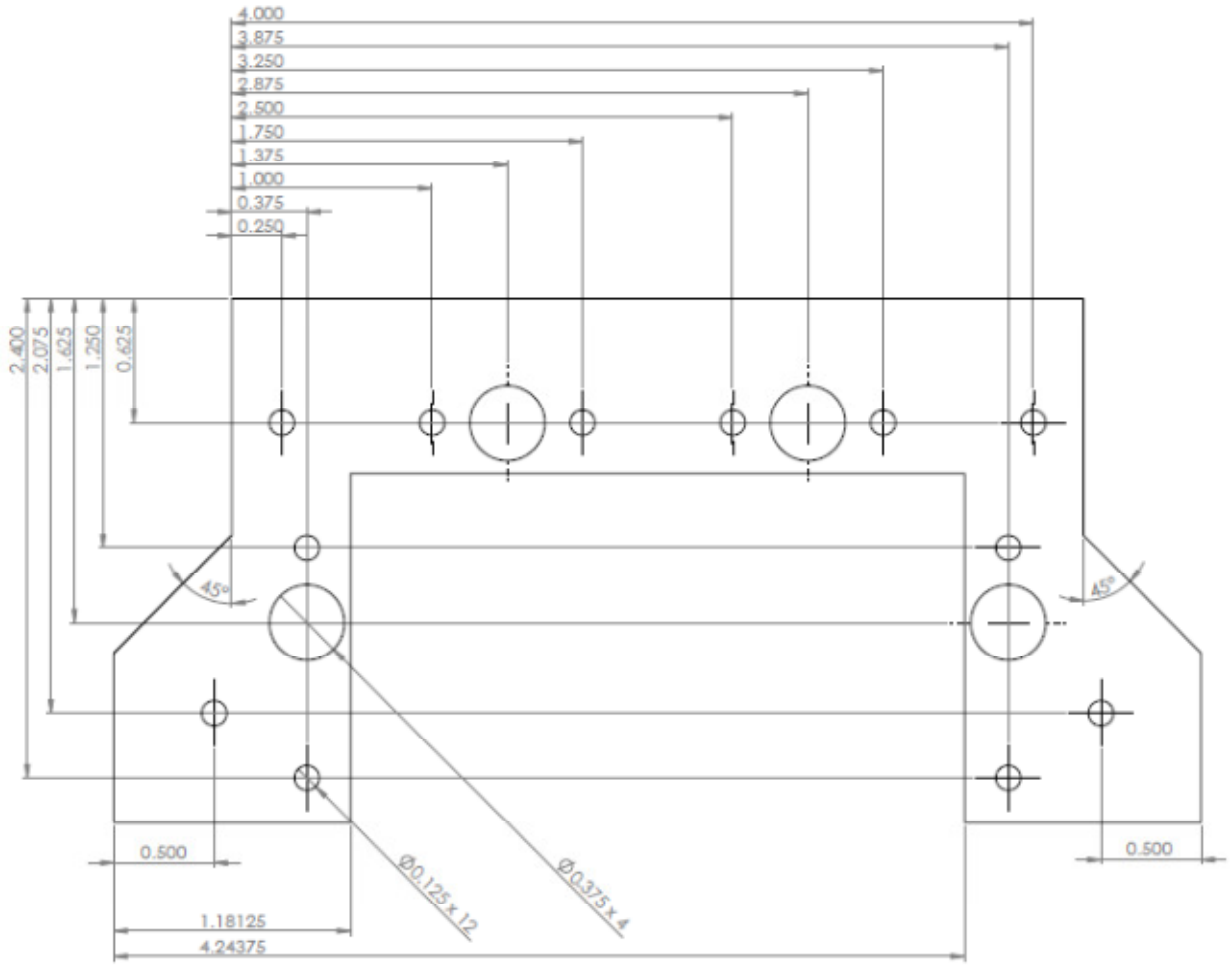

Figure 59. Front view of part 2 of the reference electrode fixture. Dimensions are in inches.

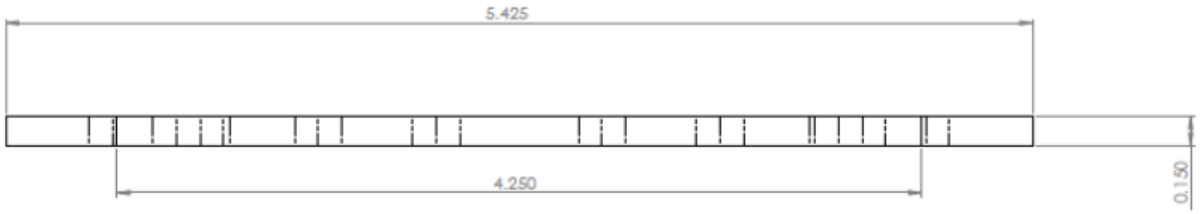

Figure 60. Top view of part 2 of the reference electrode fixture. Dimensions are in inches.

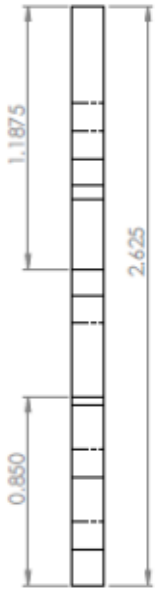

Figure 61. Side view of part 2 of the reference electrode fixture. Dimensions are in inches.

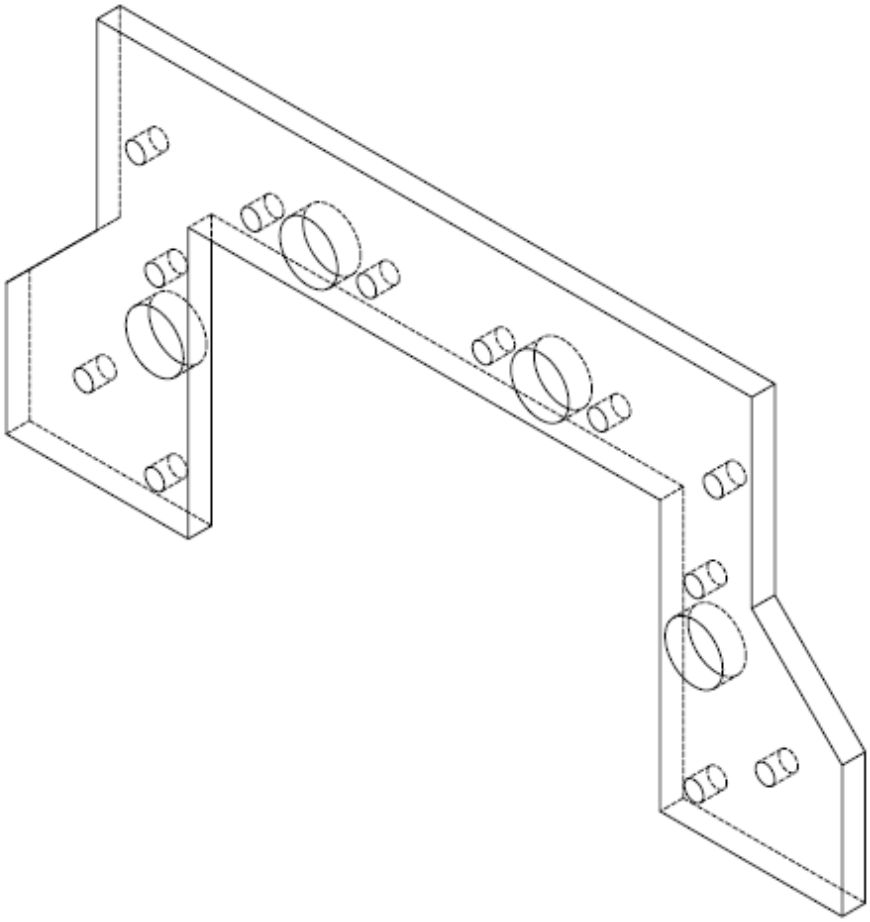

Figure 62. Isometric view of part 2 of the reference electrode fixture.